Title
Design And Management For Energy-Efficient Cyber-Physical Systems

Author
Wei, Tianshu

Publication Date
2018

Peer reviewed|Thesis/dissertation

UNIVERSITY OF CALIFORNIA
RIVERSIDE

Design and Management for Energy-Efficient Cyber-Physical Systems

A Dissertation submitted in partial satisfaction
of the requirements for the degree of

Doctor of Philosophy

in

Electrical Engineering

by

Tianshu Wei

June 2018

Dissertation Committee:

Dr. Qi Zhu, Chairperson
Dr. Hyoseung Kim
Dr. Nanpeng Yu

The Dissertation of Tianshu Wei is approved:

Committee Chairperson

University of California, Riverside

Acknowledgments

First and foremost, I would like to express my sincere gratitude to my advisor Prof. Qi Zhu, who gave continuous support of my Ph.D. study and related research and introduced me to this wonderful research area, provided me guidance with his patience, motivation, and immense knowledge. His guidance helped me in all the time of research and writing of this thesis. He is always insightful and inspiring and provided me with valuable advice and suggestions for my life and career. Many ideas in this dissertation come from discussion with him. This dissertation wouldn't have been possible without his guidance and supports. I could not have imagined having a better advisor and mentor for my Ph.D. study. I am fortunate to be one of the Ph.D. students of this lab and have learned a lot not only on the knowledge domain as well as the skills of innovation, problem solving and critical thinking, which will continue to benefit in my future career.

My thesis committee guided me through all these years. Thank you to Prof. Wei Ren and Prof. Sheldon Tan for serving as my preliminary exam committee members. I also want to thank Prof. Hyoseung Kim for letting my defense be an enjoyable moment, and for your brilliant comments and suggestions. I also would like to thank Prof. Nanpeng Yu and Prof. Shaolei Ren, who provided great insights and great helps in problem formulation in a few of my projects. I am also grateful to all the professors who taught me throughout the years. They helped me to established solid foundation for my research and career.

I am fortunate to have collaborated with many brilliant colleagues and researchers in my PhD career. They are but not limited to Taeyoung Kim, Mohammad Atiqul Islam, Bowen Zheng. Our collaborations are always fruitful and I have learned a lot from the

discussions with them. I also would like to thank my lab colleagues, Peng Deng, Bowen Zheng, Hengyi Liang, Shuyue Lan and Zhilu Wang, Di Chen. I enjoyed working with them and they brought a lot of fun to the lab. I also deepened my knowledge and broadened my horizon through the discussions and interactions with them.

Many thanks to my best friends at UCR, Peng Deng, Yue Cao, Junchao Wang, Bowen Zheng, Linchao Liao, Shukui Zhang, Xing Zheng, Hongsheng Yu, Bo Li, Peng Wang, Yan Zhu, Meng Zhao, Fei Ye, Xuewei Qi, Weimin Zhou, Ming Huang, Zhisheng Lin, Xuqing Liu. My time at UCR was made enjoyable in large part due to these friends that became a part of my life. I am grateful for time spent with these friends on playing badminton, traveling, hiking, having good food, watching sports games together. They made my life in UCR enriched. I am also very grateful to my girlfriend Elaine Lu, who is a beautiful and smart person, brought lots of enthusiasm to my life. She is always optimistic, supportive and understanding.

Finally, and most importantly, I would like to thank my family for all their love and encouragement. For my parents who raised me with a love of science and supported me in all my pursuits. They provided me with anything I need and encouraged me to pursue my dreams. Words can not express how grateful I am to my mother and father for all of the sacrifices that they have made on my behalf. They are my best friends and life mentors. This dissertation devotes to them.

To my parents for all the support.

ABSTRACT OF THE DISSERTATION

Design and Management for Energy-Efficient Cyber-Physical Systems

by

Tianshu Wei

Doctor of Philosophy, Graduate Program in Electrical Engineering
University of California, Riverside, June 2018
Dr. Qi Zhu, Chairperson

With the increasing complexity of building infrastructure, building management systems have been widely used for managing various types of energy loads and optimizing building energy efficiency. In large commercial buildings, 50% of energy consumption is from HVAC (heating, ventilation, and air conditioning) for maintaining a comfortable environment throughout the day. The rapidly growing EV (electric vehicle) charging demand has distinct operating patterns and may cause spikes in power demand. In addition, majority of datacenters are collocated within mixed-use buildings, where they often share some common infrastructures and energy supplies with other building operations. To maximize building energy efficiency, i.e., effectively lower peak power demand and reduce overall electricity cost, this dissertation develops novel model predictive control based algorithms to co-schedule HVAC, EV charging and datacenter workload with heterogeneous power supplies (e.g., power grid, solar energy and battery storage) in a holistic framework. Furthermore, to avoid the costly and time-consuming thermal dynamics model design for building control *and* to further explore more effective building management scheme, we also present deep

reinforcement learning based algorithms to intelligently learn the effective control strategies through direct interactions with real buildings, without relying on any inflexible models. The experiment results demonstrate the effectiveness of our data-driven approaches in improving building energy efficiency, while maintaining the desired temperature for building occupants, and meeting the deadlines for EV charging and datacenter workload.

To further exploit the significant energy scheduling flexibility provided by smart buildings, in addition to intelligently managing buildings' energy loads, it is also essential to coordinate the behavior of large number of buildings for enhancing the efficiency and stability of the entire power system. With the advent of advanced metering infrastructure, various energy demand from smart buildings can be coordinated together with power plants across the power grid. Most of the previous works focus on developing price-based demand response (DR) strategies, in which the buildings can only passively react to the market signals (e.g., real-time electricity price) from utilities. To improve power system efficiency and facilitate customers' engagement level in electricity market, we present a proactive building demand participation framework to integrate the operation of smart buildings into the electricity market economic dispatch. Our new DR scheme enables building customers to proactively express multi-level energy demand preferences to smart grid operators instead of passively following the load reduction instructions. The experiment results demonstrate that our proactive DR scheme can achieve significant cost reduction for both power generation and building operation, and is more robust to various malicious cyber attacks compared with passive DR strategies.

Contents

List of Figures

List of Tables

Chapter 1

Introduction

Cyber-physical systems (CPS) are the types of embedded systems that are typically monitored and controlled by computer algorithms, and tightly integrated with computation and communication. CPS systems are becoming increasingly ubiquitous with the fast developing internet and exploding IT technologies. The major applications of CPS include but not limited to power grid, building energy management systems, industrial control systems, autonomous automobiles, medical devices, etc. Among various types of CPS applications, such as smart grid and building energy management, the performance of energy efficiency and system security becomes the primary focus for designing such systems. However, due to the complicated physical dynamics and increasing complexity in buildings and power grid infrastructure, designing robust energy management systems and highly efficient control algorithms for those CPS applications is very critical and becoming more challenging. In this dissertation, we present intelligent approaches for improving the energy efficiency of smart buildings and enhancing the stability across the power grid.

This chapter will first discuss the challenges for designing energy-efficient CPS applications building management system in section 1.1. In section 1.2, we summarize related works in the recent literature and also analyze their drawbacks. In section 1.3, we introduce the overview of our solutions to address the major challenges and improve system energy efficiency. Then, our contributions in this dissertation is summarized in section 1.4.

1.1 Design Challenges

Energy Management for Smart Buildings: The scale and complexity of building infrastructure has drastically increased in recent decades. The building stock, including both commercial and residential buildings, is energy-intensive and accounts for nearly 40% of primary energy consumption, 40% of the greenhouse gas emissions and 70% of the electricity use in the U.S. [1]. Therefore, it is critical to improve building energy efficiency for enhancing the nation's power stability and environment security. There are various types of energy loads in buildings, including HVAC (heating, ventilation and air conditioning), lighting, appliances, and emerging loads such as EV (electric vehicle) charging. Among these energy loads, HVAC system is responsible for maintaining the room temperature within the desired range throughout the day and typically accounts for around 50% of the total building energy demand [1]. The energy demand of HVAC system may change drastically and cause very high peak power demand if not controlled carefully, due to the varying physical environment (e.g., outside air temperature and sun radiation) and disturbances from building occupant activities. In addition, with the rapidly increasing popularity of EV, the charging demand from building tenants has emerged as a significant energy load in many commercial buildings

with installed charging stations. In most commercial buildings, the EV charging demand typically peaks at daytime and may coincide with the HVAC demand to cause spikes during peak hours.

Nowadays, to support tremendous computational demand from the exploding digital economy (e.g., IoT applications, cloud computing, etc.), the datacenter has been growing massively. These power-intensive computational facilities range from the large-scale state-of-the-art datacenters (e.g., Google and Equinix [2]) to the small-/medium-size server rooms operated by small companies and research institutions. The total demand from datacenter loads is expected to grow quickly from 4% to over 6% in the next few years [3]. In fact, most of total datacenter energy consumption (i.e., around 96%) is from the small-/medium-size server rooms [3], which are usually colocated within the mixed-use buildings (MUBs) [4] and share the space and power infrastructure with other building operations (e.g., management of offices and labs). In addition to the traditional building energy loads (e.g., HVAC and EV charging), a report based on real-world measurement shows that the datacenter loads could dominate the overall building energy demand [5], due to its high power density (0.1-1kW per square foot [6]). Moreover, in order to remove the excessive heat generated by datacenter servers, the HVAC systems (e.g., chillers, water pumps and cooling tower) for maintaining the desired temperature in office rooms, are usually shared or partially-shared with the datacenter rooms in MUBs. If the datacenter loads are not carefully scheduled with other energy loads, the HVAC system may work inefficiently and the datacenter loads could create unnecessarily high power demand at the same time with other energy loads in the MUBs.

On the power supply side, many buildings are equipped with battery storage and various on-site renewable sources, such as solar power and wind power, which can be leveraged to further boost building energy efficiency (i.e., shave peak power demand and reduce total energy consumption cost). Given that the power grid electricity usage in buildings is often billed with time-of-use (TOU) price, which charges the electricity usage at multi-level rates for different periods in each day. Intelligently coordinating various types of energy loads with heterogeneous power supplies can further improve building energy efficiency. However, it still remains to be challenging to design an efficient energy management system to simultaneously maintain comfortable temperature for building tenants, satisfy deadlines for EV charging and datacenter workload as well as effectively reduce the peak power demand and total energy consumption cost, especially constrained by limited and intermittent renewable energy supplies and shared building infrastructures.

Demand Response in Smart Grid: To exploit the significant energy scheduling flexibility from smart buildings for enhancing the stability of power system, in addition to intelligently scheduling various energy demand within buildings, it is also essential to coordinate the behavior of large number of buildings across the entire power grid. It is estimated by [7] that with all customers participating in the demand response (DR) programs, the total peak power demand in the U.S. can be reduced by up to 150 GW. To release the huge potential in improving grid power efficiency, extensive approaches have been developed in the literature to leverage the building scheduling flexibility from various energy loads (e.g., HVAC control, EV charging, battery operation). However, most of these efforts only focus on the energy optimization within the buildings by carefully scheduling the demand of dif-

ferent energy loads based on power supply information. On the power grid side, a variety of price-based DR strategies have been proposed to provide customers with incentive for their commitment to following the load reduction instructions. However, under these passive DR schemes, the building customers can only manage their energy loads by passively reacting to the real-time price dispatched from market system operator [8]. There exists a gap between the building energy management and the electricity market optimization. The conventional single-direction communicating DR mode greatly limits the potential effectiveness of DR strategy in leveraging the tremendous flexibility from building energy loads, and can easily create peak power demand in the grid when large number of buildings are synchronized by the DR signal. Such structural rigidity results in the low customer engagement level (i.e., only 6% [9]) in demand response penetration. Little work has been done to consider combining the intelligent building energy scheduling with the electricity market economic dispatch process in an integrated framework. Therefore, it is critical to increase the engagement of customers in the DR participation and enable the electricity market operator to take fully advantage of the building scheduling flexibility across the power network.

Efficient Data-Driven Building Control: Buildings have demonstrated significant flexibility for improving the power system energy efficiency. Another challenge comes from development of accurate and efficient models for building energy management systems. In the literature, various model-based approaches have been proposed for optimizing the demand of various energy loads to improve energy efficiency [10, 11, 12, 13, 14]. These methods typically optimize the HVAC system efficiency by leveraging the building thermal flywheel effect, which plays a key part by allowing buildings to temporarily unload the HVAC systems

without significantly degrading the comfort level of occupants. However, the performance and reliability of these model-based approaches highly depend on the accurate modeling of the building thermal dynamics, and it also requires that these models can be efficiently solved with mathematical tools for optimization during runtime [15]. These conflicting limitations often result in the inefficiency when applying these approaches for building control in practice, because the building thermal dynamics can be affected by various factors (e.g., building structure and materials and heterogeneous disturbances from environment and occupants) and cannot be accurately modeled by simple formulation. Thus, the simplified building thermal dynamics models often lead to large error when estimating building state evolution due to the hidden factors that cannot be accurately measured. In fact, it is often difficult to develop an accurate building dynamics model that is also efficient enough to be integrated into optimization formulations for control purpose. Furthermore, it is also time-consuming to develop distinct models for different buildings and it could also be costly to update the models to accommodate changes in complex commercial buildings. Therefore, it is critical to develop data-driven approaches to enable efficient control algorithm design effectively co-scheduling HVAC and heterogeneous energy loads without relying on those inflexible models.

In the next section, we will briefly discuss the models and methods proposed in the literature for addressing the aforementioned issues and challenges, and the major drawbacks of these existing approaches.

1.2 Related Work

Energy Management for Smart Buildings: The peak demand and total energy consumption can be reduced through 1) intelligent scheduling of HVAC by turning on/off air conditioning and changing air flow rate and 2) management of EV charging by charging each EV with varying power levels at different times. In the literature, extensive models and algorithms have been proposed for efficient HVAC control in [12, 10, 16, 11, 17, 18, 19]. The work in [12] develops nonlinear models for the cooling system, including chillers, cooling towers and thermal storage banks, and proposes an MPC scheme for minimizing energy consumption. In [11], a building thermal behavior is modeled with RC networks and validated against historical data, and a tracking linear-quadratic regulator (LQR) is proposed for HVAC control. The work in [18] uses the similar building models as in [11], and proposes a set of HVAC control algorithms that address the sensing data inaccuracy using unscented or extended Kalman filters. In [10], the authors develop a system model with bilinear inputs, states and weather parameters, and formulate the control optimization problem as sequential linear programming (SLP). There are also approaches proposed for optimizing EV charging in [20, 21, 22] with the utilization of renewable power sources such as solar and wind. In addition to scheduling energy loads, there are also approaches proposed for scheduling heterogeneous energy sources such as battery storage at individual customer level [23, 24, 25, 26, 27]. Although these approaches can be applied for scheduling the operation of HVAC, EV charging and battery storage, little work has been done for coordinating various types of energy loads in a holistic framework and further consider managing heterogeneous loads among building clusters. We believe that coordinating the operation of

HVAC system, EV charging and heterogeneous power supplies in an integrated formulation can further improve energy efficiency.

While the energy demand from datacenters within MUBs is growing rapidly as discussed in section 1.1, there has not been sufficient work optimizing the energy management for MUBs. Majority of existing works [28, 4, 29] mainly focus on developing models and scheduling algorithms for optimizing the energy efficiency in dedicated datacenters (e.g., Google), in which all the space and cooling infrastructure are specifically designed for datacenter operations. There are other efforts [12, 10, 14, 13] in the literature that mostly focus on developing control algorithms for managing HVAC, EV charging and heterogeneous energy supplies in large commercial building, in which significant space is occupied by office rooms or labs. These approaches typically treat the datacenter computational loads as "miscellaneous" plug-in loads and ignore the significant scheduling flexibilities provided by many flexible datacenter workloads (e.g., MapReduce). Therefore, none of these isolated approaches can be effectively applied for MUBs with datacenter loads. In fact, the datacenter loads has distinct demand patterns and share the same HVAC infrastructure (e.g., water pump, chiller and cooling tower) with non-IT operations in the building. Moreover, the scheduling of datacenter workload requires a different set of control knobs (e.g., number of active servers, workload priorities) and constraints (e.g., queuing delay, request deadlines). If the energy demand for maintaining desired temperature in office rooms and the energy demand for processing datacenter workload is not carefully coordinated, they may coincide with each other to create high power demand and greatly degrade building energy efficiency.

Demand Response in Smart Grid: To further leverage the scheduling flexibility provided by smart buildings, various price-based DR schemes and control strategies have been proposed in the literature [30, 31], including time-of-use [32, 33, 34], critical peak pricing [35, 36], peak load pricing [37, 38], peak day rebates pricing [39] and real-time pricing (RTP) [40, 9, 41, 42]. Most of existing DR strategies still require building customers to passively react to the real-time price or follow the demand reduction signals. Due to rigid single-direction communication scheme, the passive DR strategies have a very low participation level and cannot fully take advantage of the significant building energy flexibility to effectively improve the power grid energy efficiency. Among the price-based DR frameworks, the work in [9] proposes an iterative real-time pricing (RTP) mechanism, which is shown to be one of the most effective approaches in coordinating distributed energy response. In the iterative RTP approach, system operators (i.e., utility companies) and customers iteratively compute electricity prices and optimal electricity demand until a stable set of electricity prices and energy consumption schedules is reached. However, when applied in practical electricity market environment, the iterative RTP mechanism suffers from two critical drawbacks: 1) due to the lossy and delayed communication process in practice, it usually takes a high number of iterations or even diverges [43] before optimal power allocation points can be achieved. Moreover, the complexity of unit commitment problem in a regional electricity market also makes this iterative negotiation process too slow and not applicable for real-time operations; 2) it is assumed that both generation company agents and customers have to comply with same bidding strategy and cannot learn and adjust their behaviors based on the historical bidding experience, which may not hold in prac-

tice. To optimize the electricity wholesale market operations, the work in [44] proposes a distributed approach to derive retail market spot pricing in a radial distribution network. In [45], a nodal pricing mechanism for distribution networks is developed for improving the efficiency of distributed generation. In [46], the authors propose a novel pricing mechanism for locational marginal pricing with consideration of significant distributed generation penetration. To integrate the residual demand modeling with the transmission and distribution power grid [47], an iterative approach is presented in [48]. Although extensive approaches have been proposed to balance the energy demand with intelligent pricing mechanisms *and* to optimize the power generation efficiency in the electricity market, none of the existing methods considers the joint optimization of flexible energy demands and generation of power plants in a holistic framework. Therefore, it is critical to bridge the gap between the customer-level energy optimization in the retail market and the network-level economic dispatch in the wholesale market, which is the focus of our work in this dissertation.

Efficient Data-Driven Building Control: To alleviate the reliance of building energy management on the rigid thermal dynamics models, some recent works start developing *data-driven* approaches for efficient HVAC control based on historical operations by leveraging the reinforcement learning (RL). The works in [49, 50, 51] propose classical Q-learning based control approaches, which use a table to store the Q value in different states. These approaches is only suitable for discrete control actions and cannot be efficiently applied for control problems with large state space. There are other works that extend the conventional Q-learning with function approximations. In [52], the authors present a neural fitted RL method to determine the optimal temperature setting points through the inter-

action with building tenants. This approach is only evaluated with a single-zone building, which is modeled by a simple differential equations formulation to simulate the heat transfer process. In [53], a model-assisted batch RL approach is developed, where the optimal Q value is approximated by randomized trees and the HVAC is only operated with a simple on-off control strategy. These RL-based methods with function approximation is suitable for control problems with continuous state space. However, they suffers from very high computational cost due to their batch update mechanism throughout the learning process. Therefore, it is critical to develop a data-driven control algorithm that can be efficiently trained for large-scale building control problems without relying on the inflexible thermal dynamics models.

In the next section, we will present the overview of our approaches for addressing the critical challenges and to fill in the gaps between existing approaches in the literature and the need of complex energy-efficient CPS applications.

1.3 Overview of Our Approaches

Energy Management for Smart Buildings: A key aspect in improving building energy efficiency is to leverage the scheduling flexibility provided by various energy demand loads in large commercial buildings, including HVAC (heating, ventilation and air conditioning), plug-in loads and emerging loads such as EV charging, etc. In particular, the HVAC system can provide significant energy scheduling flexibility, because the building thermal flywheel effect allows the HVAC systems to be turned off for a short period of time without immediately degrading the comfortability of building tenants [54]. The building

energy management system can perform pre-cooling or pre-heating to shift some energy demand from peak hours to off-peak hours, while still satisfying the desired temperature requirements. For the intermittent EV charging demand, varying charging rates can be leveraged for improving energy efficiency as long as each EV is charged with the specified energy before its departure time. Therefore, we can intelligently control the charging rate for each individual EV to effectively avoid peaking their energy demand at the same time with the HVAC system and other energy loads in the building. Furthermore, battery storage has been increasingly used at building level to effectively shave peak demand and reduce energy consumption cost, by storing grid electricity at off-peak hours (or from renewable power sources) and discharging during peak hours. As shown in Figure 1.1, the demand side energy management (e.g., HVAC air volume and EV charging rate) requires on the availability information of the various energy sources, while the supply side power resources allocation (i.e., deciding which source to use and for how much at different times) depends on the real-time knowledge of total power demand. Therefore, it is important to co-schedule the energy demands with supply sources in a holistic framework for maximizing building energy efficiency. In this dissertation, as presented in section 2.1 and section 2.2, we first construct the building thermal dynamics model with RC (i.e., resistor-capacitor) network to capture the heat transfer process and forecast the building temperature evolution. Then, we develop a novel co-scheduling algorithm based on the model predictive control (MPC) to optimally manage HVAC system, EV charging and battery usage for reducing the total building energy cost (includes electricity consumption charge and the peak power demand charge) with constraints on room temperature and EV charging deadlines. Our experiment

results demonstrate that our co-scheduling algorithm can reduce the peak power demand by up to 25% and achieve 7.5% reductio for total energy cost.

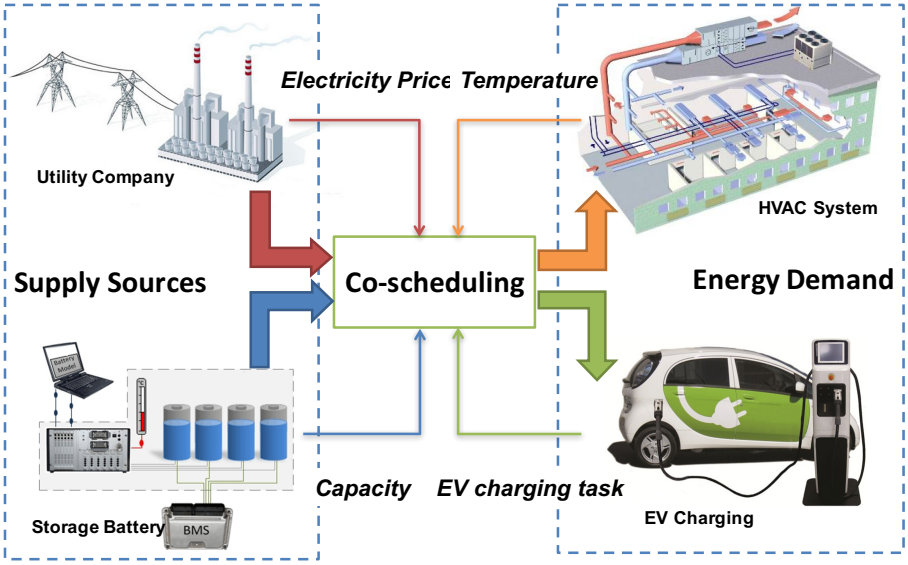

Figure 1.1: Overview of co-scheduling for HVAC and EV charging

In section 2.3, we further extend our MPC-based co-scheduling algorithm for energy management within building clusters. In this work, an integrated MPC-based formulation is first developed for co-scheduling energy demands (i.e., HVAC, EV charging) and power supplies (i.e., power grid and battery storage usage) for multiple buildings within a building cluster. This integrated formulation is able to manage the building energy loads with global optimal solutions, but also leads to very high computational complexity due to the large number of control variables in the integrated formulation. Thus, we further consider a heuristic method, which separately maximizes the energy efficiency within each building in a greedy manner. For the heuristic variant, the total battery storage capacity within the building cluster is heuristically allocated to each building based on their historical

energy consumption information. Our experiment results show that the separate-scheduling heuristic can achieve competitive energy efficiency (reduce peak power by 8.21% and total energy cost by 5.75%) within the entire building cluster while significantly reducing the computational complexity by 2.2 times.

To explore additional energy flexibility in the ubiquitous MUBs with colocated datacenter server rooms, in section 2.4, we extend the existing building energy management approaches in the literature by jointly optimizing the management of office rooms and datacenter operations, which are typically coupled together by shared HVAC devices[1]. More specifically, we further leverage the significant scheduling flexibility from various datacenter computational workload to enhance energy efficiency when operating the HVAC system to maintain the desired temperature for office rooms; on the other hand, we also consider the office room energy demand and occupant activities when scheduling the elastic computational workload and the consequent cooling demand from datacenter servers. As shown in Figure 1.2, we first develop models for key physical and cyber components in MUBs, including office thermal dynamics and comfort constraints, various types of datacenter workload and the energy/thermal demand of IT equipment, and HVAC system and its energy demand for both datacenter and office rooms. Then, we present an MPC-based formulation for co-scheduling datacenter workload and HVAC demand (for both datacenter and office rooms thermal loads), while satisfying constraints on office room temperature, computational workload delay/deadlines and the datacenter cooling requirements. In this work, we further incorporate the intermittent renewable power sources (i.e., solar power) and battery

[1]While there are various types of MUBs, in this dissertation we focus on those that are managed by a single building manager, e.g., enterprise MUBs that provides significant office space for occupants and operates private small-/medium-size datacenters.

storage in our co-scheduling framework to improve the energy efficiency. Based on real-world trace-based simulations, our experiment results show that our approach can achieve $5\% - 17\%$ energy cost reduction compared with the baseline method. Our co-scheduling formulation is also extended to optimize the trade-off between minimizing carbon footprint and reducing the total energy cost.

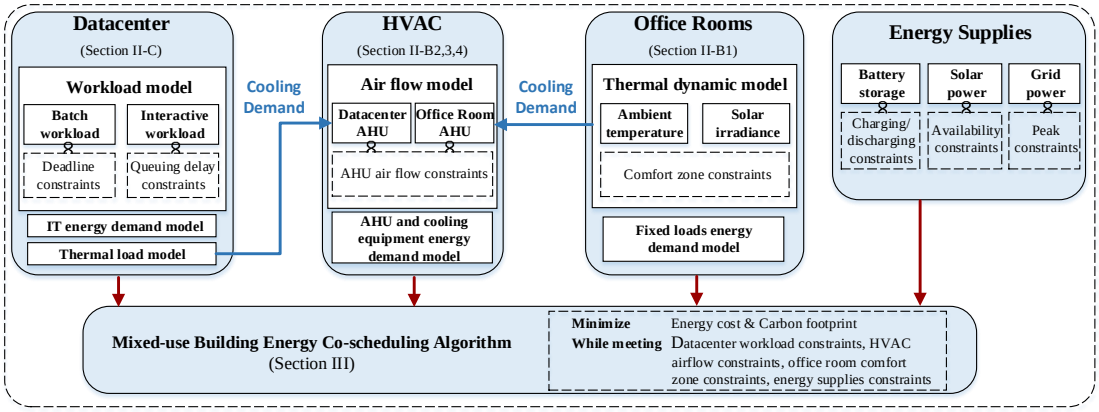

Figure 1.2: Overview of modeling of cyber and physical components and MPC-based co-scheduling algorithm for mixed-use buildings (MUBs)

Demand Response in Smart Grid: To further exploit the significant energy flexibility from buildings and encourage more customers to participate in the demand response (DR) program for improving entire power system efficiency, in section 3.1, we present an innovative DR scheme based on *proactive demand participation from smart buildings*. This work addresses the building energy scheduling and power network optimization in a holistic framework. As shown in Figure 1.3, at building level, we leverage the similar MPC-based control algorithms to co-schedule different energy loads (e.g., HVAC and EV charging) and power

supplies (e.g., grid and battery storage) to lower the energy cost within each building based on electricity price information. In this work, instead of just determining and submitting the total energy demand to power system operator, each building customer will generate a demand bid curve, which incorporates multi-level energy demand preferences under varying electricity price forecasts for current decision interval without violating building operating constraints. At power grid level, all individual demand bid curves from building customers and from the regular power plants will be aggregated at the substation (i.e., distribution network) level. Then, we solve the security constrained economic dispatch (SCED) problem at the wholesale market (i.e., transmission network) level after receiving all building demand bids and power plant supply offers. The SCED optimization is able to determine the optimal electricity market clearing price and dispatch the energy consumption quantity to each building customer, by maximizing the total social welfare for all building customers and power plants in the network. Finally, each building customer will operate various energy loads and supplies with the total energy consumption strictly following the dispatch quantity from the market operator. The clearing price will be used to charge each building's electricity usage for current decision interval. Compared with the existing passive DR strategies, our *proactive demand participation scheme* enables the electricity market operator to fully take advantage of buildings' demand flexibility by embedding buildings' scheduling flexibility into the demand bid curve, which represents building customers' willingness to pay for different amount of energy consumption. Our proactive DR scheme can further improve the DR engagement by allowing building customers to actively participate in the market clearing process, instead of just passively following demand reduction instruc-

tions. Our experiment results show that our proactive DR scheme can achieve up to 20% building operation cost reduction and 10% system generation cost reduction compared with passive DR strategies.

For different DR strategies, particularly in our *proactive demand participation* framework, various types of information, such as electricity price forecasts and buildings' demand bid curves, are required to be exchanged between decision-making entities (e.g., building energy management, electricity market operator). In practice, the advanced metering infrastructure (AMI) enables the bilateral communication between building customers and power system operators [55]. Due to the sensitive information exchanged via the wide-area network [56, 57], the *proactive demand participation* scheme may be exposed to threatenings from various malicious cyber attacks, such as private information leakage [58, 59], untruthful demand bidding [60], guideline price manipulation [55], etc. In this dissertation, we study the impact of electricity guideline price manipulation and untruthful demand bidding on our proactive demand participation scheme, and comparing it to the conventional DR scheme in section 3.2. We investigate attack strategies for the two DR schemes, and conduct experiments to evaluate the impact of guideline price manipulation and untruthful demand bidding on customers' electricity usage expense. Our experiment results demonstrate that 1) for both proactive and passive schemes, guideline price manipulations may significantly lower the attacker's own electricity cost while increasing other customers' cost; 2) our proactive DR scheme is more robust with respect to guideline price manipulation attacks than the conventional DR strategies; 3) our proactive DR scheme is less sensitive to the untruthful demand curve attacks.

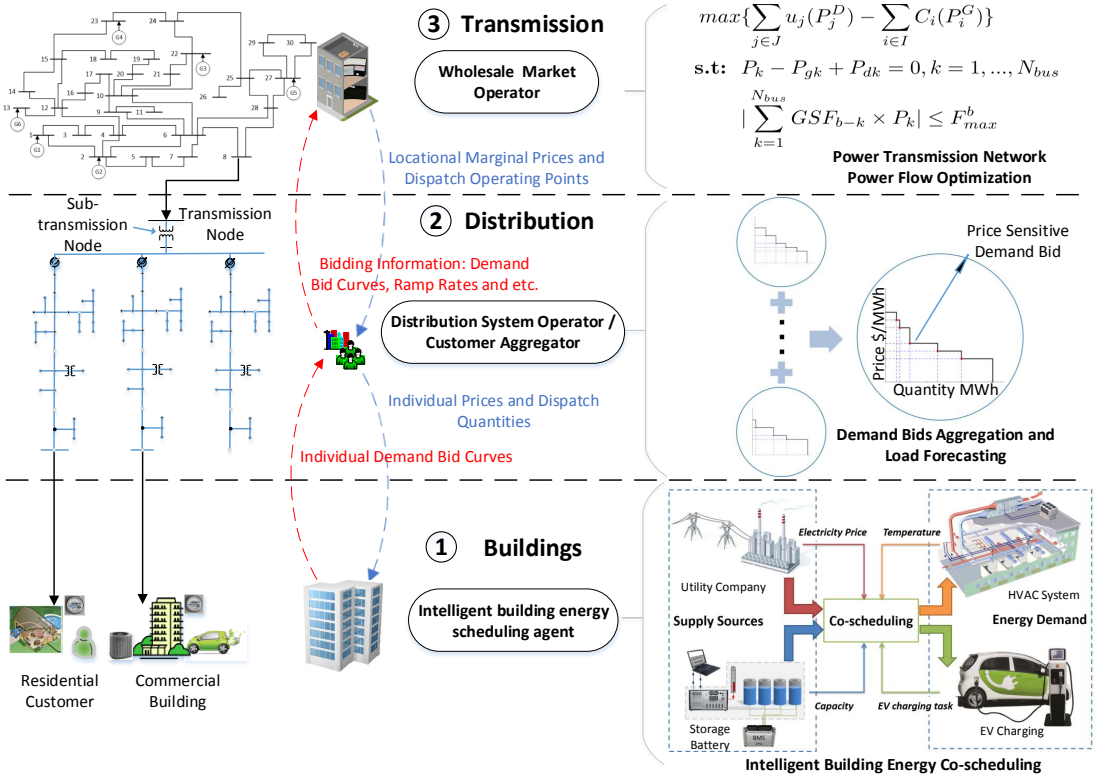

Figure 1.3: Integrated market operations framework with proactive demand participation

Efficient Data-Driven Building Control: As discussed in section 1.1, in practice, it is often time-consuming and inefficient to develop thermal dynamics models for building HVAC control. To further explore more effective control strategies while reducing the model design complexity, in section 4.1, we develop data-driven control algorithms for building energy management by leveraging the state-of-the-art *deep reinforcement learning* (DRL) techniques, which have demonstrated to be successful in playing Atari and Go games [61, 62]. One important feature of DRL is that it is able to learn the effective control strategy directly from the historical operating data without relying on any expensive models. Moreover, deep

neural networks are also used in DRL for estimating the optimal action value in order to overcome the shortcoming of conventional reinforcement learning (RL) methods *and* enables the DRL to handle control problems with large state space. These features make the DRL emerge as an efficient and powerful approach for addressing complex control problems. In this dissertation, we first model the building HVAC operation as a Markov decision process (MDP) [2] by defining the key components, such as system state, control actions and reward function. Then, a DRL-based algorithm is developed for effective HVAC control (i.e., maintain desired temperature for building tenants while reduce the total energy cost) without leveraging any thermal dynamics models. A heuristic variant of our DRL control algorithm is further presented to perform efficient control for large-scale buildings with multiple thermal zones. We develop a co-simulation framework based on *EnergyPlus* [3] and *BCVTB* to facilitate training of the DRL agent and to evaluate the effectiveness of our DRL-based control algorithms. Our experiment results show that our DRL-based control algorithm can intelligently control the HVAC for maintaining comfort temperature through direct interactions with building environment, while effectively reduce the total building energy consumption cost by $20\% - 70\%$.

1.4 Contributions

The main contributions of this dissertation include:

- We develop novel algorithms based on model predictive control (MPC) to co-schedule HVAC control, EV charging and battery usage in a holistic framework for reducing the

[2] Our MDP formulation is general and can be time-variant as well.

[3] For offline training and validation of our algorithm, we leverage detailed building dynamics model built in the widely-adopted *EnergyPlus* [63] simulation tool. It should be noted that while the detailed EnergyPlus models are highly accurate and suitable for offline training and validation, their high complexity makes them unsuitable for real-time control.

peak demand and total building energy cost [13, 14, 64]. The MPC-based formulations are further extended for energy management in building clusters with shared limited power resources. We also model the major physical and cyber components of MUBs (part of space is reserved for datacenter operations) to minimize the overall energy cost while satisfying requirements on office room temperature, datacenter computational workload deadlines [65].

- We present an innovative proactive demand response (DR) scheme with proactive participation of smart buildings. Our proactive DR scheme allows the building customers to proactively participate in the economic dispatching decision and enables the electricity market operator to effectively leverage the significant scheduling flexibility from smart buildings [66, 64, 67, 68]. We also evaluate the robustness of our proactive DR scheme against the various cyber attacks, such as guideline price manipulation and untruthful demand bidding.
- We present a data-driven approach for HVAC control by formulating the HVAC operation as a Markov Decision Process (MDP). We develop a model-free control algorithm for minimizing the building energy cost while maintaining the desired temperature for building occupants based on the deep reinforcement learning (DRL) technique. We further present a scalable heuristic variant for efficient control of large buildings with multiple thermal zones [69, 70]. A co-simulation framework based on EnergyPlus is also developed for evaluation and facilitating the training process.

The outline of the remaining dissertation is organized as follows. In Chapter 2, various MPC-based are presented for optimally scheduling energy demand in smart build-

ings. In Chapter 3, we present a proactive demand participation framework for improving the power efficiency in the entire power network by further integrating our intelligent building energy management with economics dispatch process in the smart grid. In Chapter 4, we present our DRL-based control algorithms for building HVAC control without relying on any thermal dynamics models. Finally, this dissertation is concluded in Chapter 5.

Chapter 2

Co-Scheduling for Energy-Efficient Buildings

In this chapter, we develop models for various energy loads in buildings and present our energy-efficient control algorithms for building energy management. In section 2.1, we first introduce our modeling and MPC-based control algorithm for co-scheduling the operations of HVAC and battery storage [13]. Then, in section 2.2 we construct models for EV charging tasks and extend our control algorithm for scheduling HVAC control, EV charging and battery usage in a holistic framework [14]. Next, we further extend our MPC-based approach in section 2.3 for improving energy efficiency in building clusters [64]. Finally, in section 2.4, we combine our models for building energy management with datacenter load scheduling and develop co-scheduling algorithm for mixed-use buildings (MUBs) [65].

2.1 Co-scheduling of HVAC Control and Battery Usage

To lower the electricity energy cost in buildings, there are two main portions of the electricity cost that we can optimize, i.e., the total amount of the electricity used (measured in kWh), and the monthly peak power demand (measured in kW). As an example, we monitored the electricity usage and cost of our building testbed at the Center for Environmental Research and Technology (CE-CERT) [1]. In June 2013, the peak power demand of the building testbed is 72.4 kW, which is billed at the rate of $10.48 per kW and leads to the peak demand charge of $758.75. The total electricity consumption cost is $2,390.82, in which over 30% is contributed by the peak demand charge. We also notice that the power demand of HVAC change drastically and accounts for around 65 kW during peak hours, as shown in Figure 2.1, while the remaining 7.4 kW comes from other energy loads (e.g., lighting and office equipment) [2]. Therefore, over 4% cost reduction can be achieved if we can reduce the HVAC peak power demand by 20%. It is important to intelligently control the HVAC to improve the building energy efficiency. We believe that the peak power charge can be greatly reduced if we can temporarily turn off some air conditioning units during peak hours, and shift the peak demand from peak hours to non-peak hours while still maintaining the desired temperature for building occupants.

In this section, we present a model predictive control (MPC) based algorithm to effectively minimize the total electricity cost, including the electricity consumption charge,

[1] We use the real building testbed at the Center for Environmental Research and Technology (CE-CERT) in University of California, Riverside (UCR) to identify energy saving opportunities, provide proper simulation parameters for our approaches. The building testbed is located off campus in an industrial zone. It pays standard industrial electrical time of use rates which includes peak and demand charges.

[2] We also reviewed the electricity usage for another two larger buildings at CE-CERT, and the peak HVAC demand charge has an even higher percentage in the total electricity cost (25% - 30%).

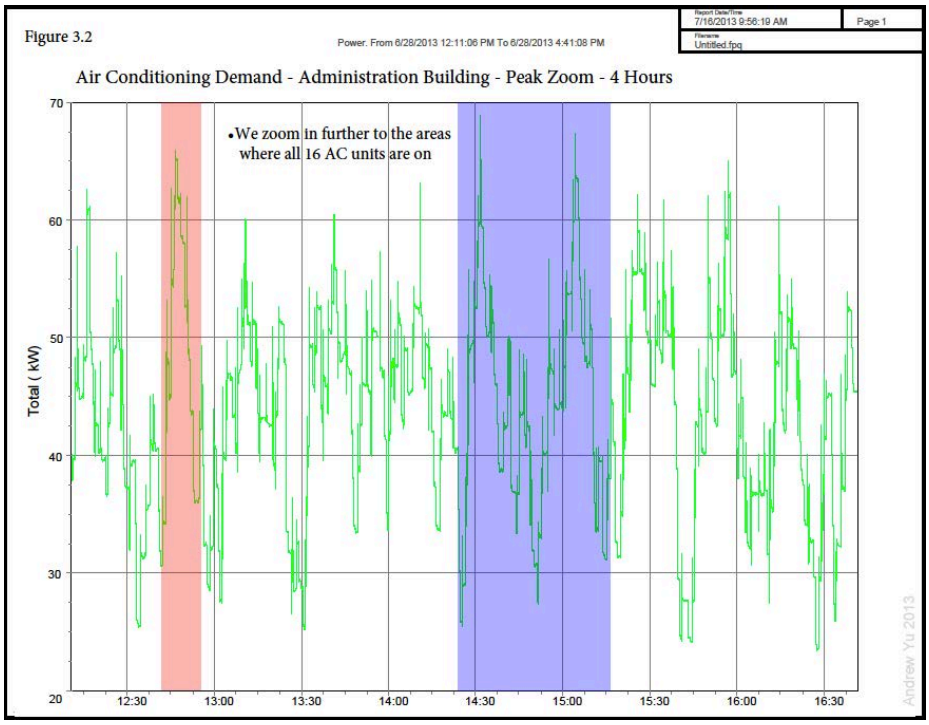

Figure 2.1: HVAC demand collected from the building testbed at CE-CERT during peak hours (12 : 00 pm to 5 : 00 pm) on June 28, 2013.

the peak demand charge, by coordinating the HVAC operation and battery usage. We first present our thermal dynamics model for estimating the temperature evolution in the building and our battery model for capturing the battery charging/discharging characteristics.

2.1.1 System Models

A. Building Thermal Dynamics Model

The heat transfer process among different entities in the building can be modeled with the RC (resistor-capacitor) network as shown in Figure 2.2, in which the heat can be stored by capacitor-like components and there exists certain resistance for heat transfer

between different components. We use a set of differential equations to capture the building

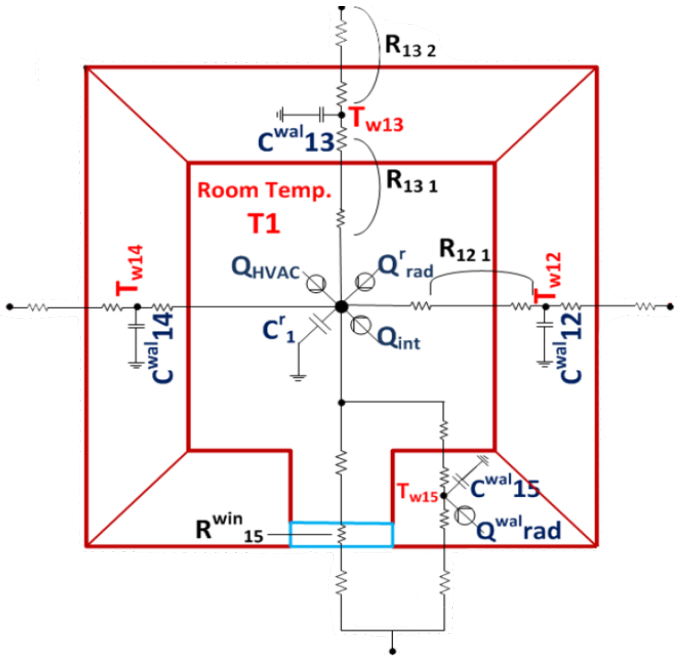

Figure 2.2: Diagram of the RC network of one room.

thermal dynamics similar as in [11, 18]. Different entities in the building can abstractly represented by a node and there are two major types of nodes in the RC network, i.e., wall nodes and room nodes. We assume there are total n nodes in the building, m of which represent room nodes and the remaining $n-m$ represent wall nodes. In our thermal dynamics model, the temperature of the i-th wall node is represented by the following equation (2.1):

$$C_{\omega_i}\frac{dT_{\omega_i}}{dt} = \sum_{j\in\mathcal{N}_{\omega_i}} \frac{T_j - T_{\omega_i}}{R'_{ij}} + r_i\alpha_i A_i q''_{rad_i} \tag{2.1}$$

where T_{ω_i}, C_{ω_i}, α_i and A_i are the temperature, heat capacity, absorption coefficient and area of wall i, respectively. R'_{ij} represents the total resistance between wall node i and

adjacent node j. q''_{rad_i} is the radiative heat flux density on wall i. $\mathcal{N}_{\omega_i}$ denotes the set of all of neighboring nodes to wall node i. r_i is an indicator that equals to 0 for internal walls, and is set to 1 for peripheral walls that are directly exposed to the sun radiation. In equation (2.1), the temperature change of the i-th wall is affected by the heat transfer between adjacent nodes and the heat injection from the solar irradiance. Next, the temperature of the i-th room node is governed by the following equation (2.2):

$$C_{r_i}\frac{dT_{r_i}}{dt} = \sum_{j\in\mathcal{N}_{r_i}} \frac{T_j - T_{r_i}}{R'_{ij}} + \dot{m}_{r_i}c_a(T_{s_i} - T_{r_i}) + \omega_i\tau_{\omega_i}A_{\omega_i}q''_{rad_i} + \dot{q}_{int_i} \tag{2.2}$$

where T_{r_i}, C_{r_i} and $\dot{m}_{r_i}$ are the temperature, heat capacity and conditioned air mass flow into the room i, respectively. c_a is the specific heat capacity of air. A_{ω_i} represents the total area of window on walls surrounding room i, τ_{ω_i} is the transmissivity of glass of window in room i. q''_{rad_i} is the radiative heat flux density radiated into room i, and $\dot{q}_{int_i}$ denotes the total internal heat generation inside room i. $\mathcal{N}_{r_i}$ represents the set of all of the neighboring nodes to room i. ω_i is equal to 0 if none of the walls surrounding room i has window, and is set to 1 otherwise. More details of building thermal modeling and estimation of the un-modeled dynamics are presented in [71, 17, 11].

The above heat transfer equations for walls and rooms yield to the following state space form of the system dynamics:

$$\begin{aligned} \dot{x}_t &= f(x_t, u_t, \hat{d}_t) \\ y_t &= Cx_t \end{aligned} \tag{2.3}$$

where $x_t \in \mathbb{R}^n$ is the state vector representing the temperature of the nodes in the thermal network. $u_t \in \mathbb{R}^{lm}$ is the input vector representing the conditioned air mass flow rate and

discharge air temperature of conditioned air into each thermal zone. $y_t \in \mathbb{R}^m$ is the output vector of the system representing the temperature of the thermal zones. C is a matrix used for calculating rooms' temperature out of the system state and $\hat{d}_t$ captures the disturbance in the building environment.

The above nonlinear thermal dynamics formulation is used for building state estimation and as the plant model to estimate the actual temperature evolution. While for control purpose, we need to use a simplified format that can efficiently solved by mathematical tools during run-time control. The original nonlinear thermal dynamics model is linearized around the system operating point by using Jacobian linearization (details can be found in[71]). The system equilibrium point is obtained by starting from an initial point and using a sequential quadratic programming(SQP) search algorithm [72] until it finds the nearest equilibrium point to the specified system operating point (through solving a series of quadratic programming(QP) subproblems). Then, we use zero-order hold to discretize the linear state space formulation and derive the following discrete time LTI thermal dynamics model (2.4):

$$x_{k+1} = Ax_k + Bu_k + E\hat{d}_k \tag{2.4}$$

$$y_k = Cx_k$$

where A is the state transition matrix and B denotes the input matrix. Matrix E combines the impact of heterogeneous environment disturbances. C represents a matrix of proper dimension to select room temperature from building state estimation x_k.

B. Battery Model

Battery discharging current will decrease as the remaining energy in the battery gets lower. The battery open circuit voltage and the discharging characteristic is studied in [73], the battery open circuit voltage VOC is a nonlinear function of battery state-of-charge (SOC), as shown in equation (2.5).

$$VOC(t) = b_1 e^{b_2 \cdot SOC(t)} + b_3 \cdot SOC(t)^3 + b_4 \cdot SOC(t)^2 + b_5 \cdot SOC(t) + b_6 \tag{2.5}$$

where $b_1, b_2, b_3, b_4, b_5, b_6$ are constant coefficients and SOC is a percentage that represents the remaining energy level in the battery.

2.1.2 MPC-based Co-scheduling Algorithm

Model predictive control (MPC) is a heuristic algorithm, which optimizes the system performance by predicting the system behavior within a short period of time (called predicting window). At each control step, only the decision for the first time step within the predicting window is applied to control the HVAC (i.e., the conditioned air flow rate for each thermal zone in this work). Then, MPC formulation will be solved repeatedly at every control step to optimally [3] operate the HVAC system. We define a predicting window of length w and optimize the objective function (2.6) by determining the air flow rate and battery discharging rate for every decision step within the predicting window. The objective function will minimize the power grid electricity cost, battery depreciation cost, battery overuse cost and the peak power charge within the predicting window, with respect

[3] While the solution provided by MPC-based algorithm is not globally optimal, we can still derive a near-optimum solution if the environment disturbances don't change rapidly and we have an relatively accurate thermal dynamics model to predict temperature evolution.

to constraints from (2.7) to (2.16). Note that this second term is not the actual peak power demand charge but rather a penalty to lower the peak demand during optimization. In practice, peak power demand charge is calculated based on the highest demand within a billing cycle (often a month), while the predicting window of our MPC formulation is at the granularity of hours. Our MPC formulation is shown as follows from (2.6) to (2.16). The notations of various parameters and variables in our formulation are summarized in Table 2.1, 2.2 and 2.3.

$$\min \sum_{t=j}^{j+w-1} \left[p_g(t) \cdot [e_g(t) + charge(t)] + p_b \cdot e_b(t) + p_{bo} \cdot [E_b + e_b(t) - B(t)]^+\right] + p_p \cdot \max_{t=j}^{j+w-1} \{e_g(t) + charge(t)\} \tag{2.6}$$

$$T(t+1) = A \cdot T(t) + B \cdot u(t) + E \cdot dist(t) \tag{2.7}$$

$$T_{lowBound}(t+1) \leq C \cdot T(t+1) \leq T_{upBound}(t+1) \tag{2.8}$$

$$e(t) = [c_1 \cdot u(t)^3 + c_2 \cdot u(t)^2 + c_3 \cdot u(t) + c_4] \cdot AC_p \tag{2.9}$$

$$e_g(t) \geq e(t) - e_b(t),\ e_g(t) \geq 0,\ e_b(t) \geq 0 \tag{2.10}$$

$$U_{lowBound} \leq u(t) \leq U_{upBound} \tag{2.11}$$

$$VOC(t) = b_1 e^{b_2 SOC(t)} + b_3 SOC(t)^3 + b_4 SOC(t)^2 + b_5 SOC(t) + b_6 \tag{2.12}$$

$$B(t) = SOC(t) \cdot C_b \cdot U_N \tag{2.13}$$

$$e_b(t) \leq B(t),\ e_b(t) \leq U_N \cdot VOC(t)/R_b \tag{2.14}$$

$$0 \leq charge(t) \leq U_N \cdot C_i,\ charge(t) \leq E - B(t) \tag{2.15}$$

$$SOC(t+1) = SOC(t) - e_b(t)/U_N/C_b \tag{2.16}$$

where equation (2.7) estimates the temperature in each thermal zone based on the current system state, conditioned air flow input and the environment disturbances by leveraging our building thermal dynamics model presented in section 2.1.1. At each time step, the zone temperature needs to be controlled within the desired temperature range $[T_{lowBound}, T_{upBound}]$ by applying constraint (2.8). Equation (2.9) calculates the energy consumption of HVAC based on airflow demand, the coefficients are estimated based on the HVAC energy consumption from real buildings in [74]. Constraint (2.10) specifies the relationship between total building demand and power supplies (i.e., the power from grid and battery discharging should be greater than the total HVAC energy demand). Equation (2.11) is a constraint on HVAC air flow rate. Equation (2.12) calculates the open circuit voltage of battery as discussed in section 2.1.1, and equation (2.13) determines the remaining energy stored in battery. Constraints (2.14) sets the battery discharging boundary, in which R_b denotes the battery internal resistance and $VOC(t)/R_b$ represents the maximum discharging current as battery open circuit voltage $VOC(t)$ decreases over time. We assume that with the help of battery management system, the battery storage can power the electrical system at a constant voltage level denoted by nominated voltage U_N, and therefore $U_N \cdot VOC(t)/R_b$ represents the maximum discharging rate at decision step t. Constraint (2.15) denotes the battery charging boundary. Finally, the status of battery SOC status is updated by equation (2.16).

Variables	Definition
$b1, b2, b3, b4, b5$	battery model coefficients
p_b	battery depreciation cost
$SOC(t)$	state of charge
C_b	capacity of battery
R_b	internal resistance
E_b	battery lower threshold
E	total battery capacity
p_{bo}	battery overuse cost
$B(t)$	battery residual electricity
C_i	battery charging current

Table 2.1: Notations of battery parameters

Variables	Definition
$c1, c2, c3, c4$	energy coefficients
AC_p	AC power
$U_{upBound}$	air flow upper bound
$U_{lowBound}$	air flow lower bound
U_N	nominal voltage of AC

Table 2.2: Notations of HVAC parameters

Variables	Definition
$p_g(t)$	electricity price
p_p	peak power charge
$T_{upBound}(t)$	comfort zone upper bound
$T_{lowBound}(t)$	comfort zone lower bound
$Tctrl$	room states
$u(t)$	air flow rate
$e_g(t)$	electricity from power grid
$e_b(t)$	electricity from battery
$charge(t)$	power grid charges battery

Table 2.3: Notations of variables and constrains

2.1.3 Experiments

A. Experiment Setup

In this section, we conduct experiments to evaluate the effectiveness of our algorithm for co-scheduling HVAC control with battery usage. The simulation parameters are chosen based on the building testbed. Our experiment is conducted for 24 hours of operation and the predicting window of our MPC-based algorithm is set to 8 hours.

B. Experiment Results

(1) HVAC operation without battery usage: Figure 2.3 shows the electricity consumption during each hour provided by the power grid when the power grid is the only available energy resource. To keep temperature within the desired temperature range, the electricity consumption from 9 : 00 am to 3 : 00 pm is very high. According to the time-of-use (TOU) electricity price offered by utility companies, this period of time is also during peak hours. Such energy consumption profile results in high electricity consumption charge and also high peak demand charge.

(2) Co-scheduling HVAC control with battery usage: when battery storage is available, we can charge the battery during off-peak hours, and use our MPC-based co-scheduling algorithm to determine the optimal discharging rate to power the HVAC system during on-peak hours to reduce the energy cost. Figure 2.4 shows the result with a 500 Ah battery storage. In the figure, the black curve represents the electricity provided by the power grid to operate the HVAC system. The area between black and red curves represents the electricity stored in battery during off-peak hours. The area between black and blue curves

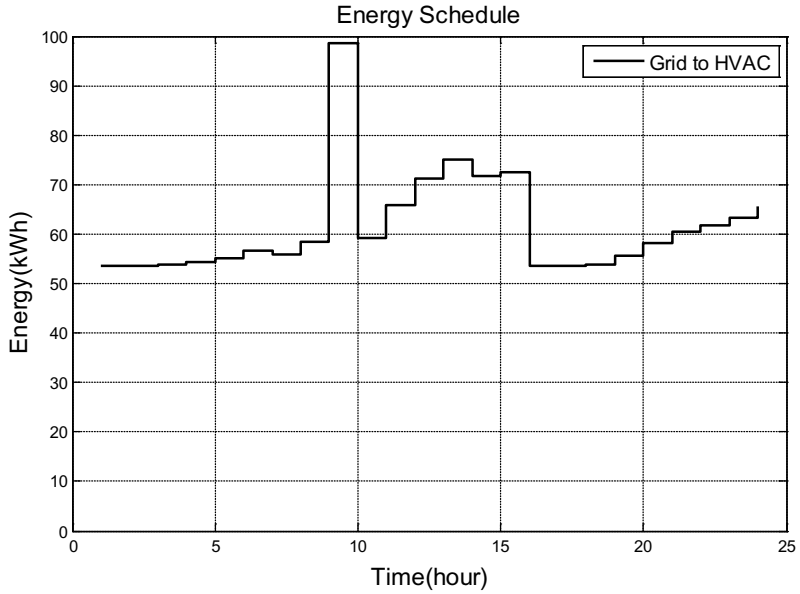

Figure 2.3: Energy scheduling by only using power grid

is the electricity provided by battery for reducing the on-peak electricity consumption from the grid. The higher values along red and black curves denotes the electricity consumption from the power grid. Compared with Figure 2.3, the power grid electricity usage is much more smooth over time when the battery storage is used, thus reducing both electricity consumption charge and peak demand change.

(3) Impact of battery capacity: we also studied the impact of battery storage capacity on the potential energy cost saving. Figure 2.5 shows the total energy cost reduction in a month with different battery capacities (varying from 50 Ah to 500 Ah). It is calculated by comparing the total cost by using battery and grid electricity versus the total cost by using only the grid electricity. Note that after the battery capacity exceed 500 Ah, the total cost reduction stops increasing. That is because the battery capacity is already large enough for the current HVAC system and the addition capacity is not being utilized.

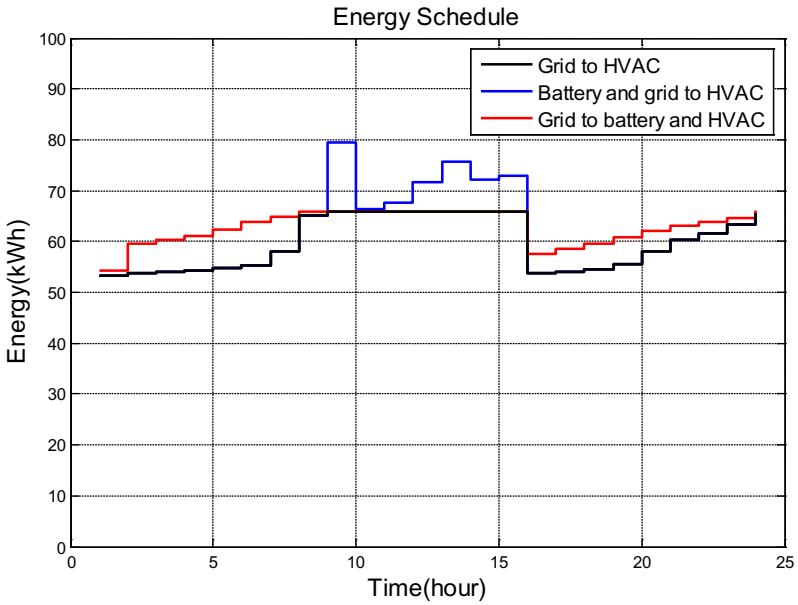

Figure 2.4: Energy scheduling by using power grid and battery storage

2.2 Co-scheduling of EV Charging, HVAC Control and Battery Usage

In this section, we consider the buildings with two major energy loads, i.e., the HVAC control and the emerging EV charging demand. We develop models for EV charging demand and present a novel algorithm based on model predictive control (MPC) to coordinate HVAC control, EV charging and battery usage for reducing the total building energy cost, including both the electricity consumption charge and the peak demand charge. The energy demand side optimization of HVAC control and EV charging depends on the information of battery storage availability and the price of power grid electricity. While the power supply side scheduling (i.e., determine when to use battery power and the optimal charging/discharging rate) is based on the real-time knowledge of HVAC and EV charging

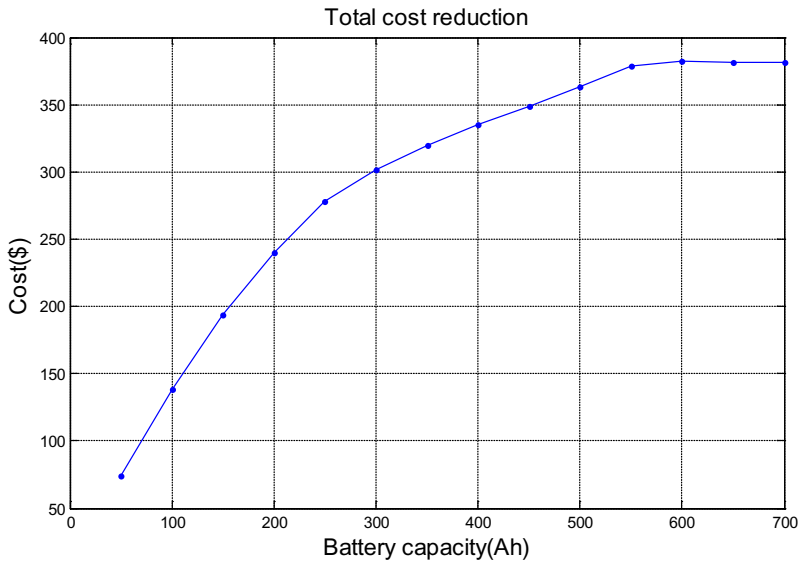

Figure 2.5: Total cost reduction with different battery capacities

demand. We address all these factors in an integrated MPC formulation, with constraints on room temperature, EV charging deadlines and battery safety.

In this work, the energy demand of HVAC system is estimated based on the room thermal dynamics model, which explicitly depicts the impact of the conditioned air input from HVAC system and environment disturbances on the room temperature. The power demand of EV charging is constrained by the total energy demand of each EV, the maximum charging rate and the deadlines for the requested energy. Next, in section 2.2.1, we will introduce our building thermal dynamics model, EV charging model and the battery model, which are the key components of our co-scheduling algorithm presented in section 2.2.2.

2.2.1 System Models

A. Room Thermal Dynamics Model

In this work, we use a similar linear thermal dynamics model as in section 2.1.1, the original model based on nonlinear differential equations is linearized around the nearest equilibrium point [71] for control design. The original nonlinear model is used as the building simulation platform for computing the actual building temperature evolution in our experiment. Then, we can derive the discrete time LTI thermal dynamics model (2.17), (2.18) by discretizing the state space realization using zero-order hold (details of the thermal dynamics model is discussed in section 2.1.1).

$$x_{k+1} = Ax_k + Bu_k + E\hat{d}_k \tag{2.17}$$

$$y_k = Cx_k \tag{2.18}$$

where A, B and E represent the state transition matrix, input matrix and environment disturbance matrix, respectively. Matrix C is used for selecting the specific room temperature from the entire building system states.

B. Electric Vehicle Charging Model

We use a 4-tuple $(s_k^J, d_k^J, e_k^J, r_k^J)$ to represent each EV charging task J_k, similarly as in [20]. s_k^J and d_k^J denote the arrival time and departure time of the vehicle, respectively. e_k^J denotes the total energy demand of the charging task J_k, which needs to be fully delivered to that EV before its charging deadline d_k^J. In addition, r_k^J denotes the reservation time, which represents the moment this EV charging task is known to the building system (r_k^J equals to s_k^J if the EV arrives without reservation) before its actual arrival time s_k^J. In our

experiment, we can evaluate the impact of knowing EV charging demand beforehand on building energy efficiency by adjusting the reservation time r_k^J for each EV. To guarantee that each EV charging task is feasible, the following constraints should be satisfied, in which p_r represents the maximum charging rate. Constraint (2.19) requires that the total energy demand for each EV should be less than the maximum energy that could be delivered to that EV between its arrival and departure time. Constraint (2.20) guarantees that the EV charging deadline must be smaller than the EV arrival time.

$$(d_k^J - s_k^J) \cdot p_r \geq e_k^J \tag{2.19}$$

$$r_k^J \leq s_k^J \tag{2.20}$$

As shown in Figure 2.6, we divide the timeline into a set of intervals I_i based on the EV arrivals and departures [75]. Each interval I_i may contain several decision steps, which correspond to the decision steps in our MPC-based co-scheduling algorithm (details are introduced later in section 2.2.2. The predicting window in the figure is also used in the MPC-based co-scheduling). Instead of simply using one decision variable for every EV charging task at each decision step, we first determine how much energy should be delivered to each EV within each interval I_i, and then use one decision variable for each decision step to determine the total energy consumption from all EVs that overlap with that decision step. The motivation of this design is that within each interval I_i, there is no EV arrival or departure, and thus the overall EV charging demand doesn't change within that interval. Each interval often contains multiple decision steps and each decision step within that interval usually corresponds to multiple EV charging tasks as shown in Figure 2.6. Therefore, it is inefficient to separately determine the energy consumption

of each EV at each decision step within an interval. The definition of intervals can help reduce the complexity (i.e., the number of decision variables in our formulation) of our EV charging model. As an example, interval I_2 contains 4 decision steps, and each decision step corresponds to two EV charging tasks, i.e, J_1 and J_2. In our modeling, we only need $6 = 2+4$ (2 variables for determining energy consumption for each EV charging task within interval I_2 and 4 variables for determining the total energy consumption of all EVs at each decision step) decision variables, instead of $8 = 2 \times 4$ decision variables when inefficiently determining the energy consumption for each EV charging task at each decision step within interval I_2.

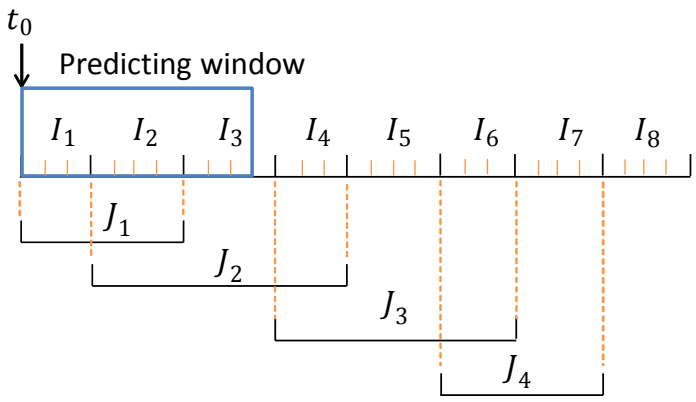

Figure 2.6: EV charging task sequence and intervals

As stated before, we formulate the EV charging constraints as shown in (2.21), (2.22) and (2.23), which determine the total energy consumption of all EVs at each decision step and ensure that the energy demand of each EV charging task can be satisfied. p_r denotes the maximum charging rate. $I_i \times p_r$ is the maximum amount of energy that can be delivered from energy sources to the EV within interval I_i.

$$\forall_j \quad \sum_{i=I_j^s}^{I_j^e} D_{ij}^J \geq e_j^J \tag{2.21}$$

$$\{\forall_j, \forall_i | I_j^s \leq i \leq I_j^e\} \quad D_{ij}^J \leq I_i \times p_r \tag{2.22}$$

$$\forall_i \quad \sum_{t=t_i^s}^{t_i^e} e^J(t) \geq \sum_{j \in \mathcal{J}_i} D_{ij}^J \tag{2.23}$$

Constraint (2.21) guarantees that each EV receives enough energy during the charging period, where I_j^s and I_j^e denote the index of the first and the last interval corresponding to EV charging task J_j, respectively, and D_{ij}^J denotes the energy that is delivered to EV charging task J_j within the interval I_i. Constraint (2.22) ensures D_{ij}^J to be no more than the maximum amount of energy that could be charged within interval I_i for an EV. Constraint (2.23) further determines the EV energy consumption at decision step level and ensures that the total energy delivered to EV during interval I_i is sufficient for all EV charging tasks that overlap with interval I_i. $e^J(t)$ denotes the amount of energy that is consumed for total EV charging at decision step t. t_i^s and t_i^e denote the starting step and the ending step of interval I_i, respectively. $\mathcal{J}_i$ represents the set of EV charging tasks, whose charging period overlap with interval I_i. Within each decision step, we assume all EVs, which correspond to that decision step, are charged proportionally to their interval demand D_{ij}^J, as shown below in equation (2.24).

$$\{\forall_i | j \in \mathcal{J}_i, t_i^s \leq t \leq t_i^e\} \quad e_j^J(t) = e^J(t) \times \frac{D_{ij}^J}{\sum_{j \in \mathcal{J}_i} D_{ij}^J} \tag{2.24}$$

For the case studies in this work, we consider commercial buildings and use Gaussian distribution to model the pattern of EV arrival and departure within one workday [76]. The arrival time is generated following distribution $\mathcal{N}(9, 4/1.96)$ and the departure time

is generated following $\mathcal{N}(18, 4/1.96)$ (i.e., assuming most people arrive around 9 : 00 am and leave around 6 : 00 pm). We then generate the charging demand for each EV based on the work in [77, 78]. First, as shown in equation (2.25), the traveled distance at the beginning of recharging follows the log-normal distribution with parameters extracted from real transportation data [77, 78]. d represents the traveled distance since last charging. We let d_R denote the average maximum total travel distance of EV once it is fully charged. Then the battery state-of-charge (SOC) can be simply calculated as $SOC = 1 - d/d_R$. The SOC of EV battery at the beginning of recharging follows distribution in equation (2.26).

$$g(d; \mu, \sigma) = \frac{1}{d\sigma\sqrt{2\pi}} e^{-\frac{(\ln d - \mu)^2}{2\sigma^2}} \tag{2.25}$$

$$h(SOC; \mu, \sigma) = \frac{1}{(1 - SOC)\sigma\sqrt{2\pi}} \times e^{-\frac{\left(\ln [d_R(1-SOC)] - \mu\right)^2}{2\sigma^2}} \tag{2.26}$$

C. Battery Model

In this work, we use a similar battery model as in section 2.1.1. The battery open circuit voltage VOC with respect to battery state-of-charge (SOC) can be calculated by equation (2.27) [73].

$$VOC(t) = b_1 e^{b_2 \cdot SOC(t)} + b_3 \cdot SOC(t)^3 + b_4 \cdot SOC(t)^2 + b_5 \cdot SOC(t) + b_6 \tag{2.27}$$

2.2.2 HVAC, EV and Battery Co-scheduling Algorithm

Based on the models introduced above, we present our co-scheduling algorithm in this section. The main goal of the co-scheduling algorithm is to optimize the scheduling of HVAC control, EV charging and battery usage together in an integrated formulation for shaving the peak power demand and reducing the total energy cost in the building.

Our co-scheduling algorithm is based on model predictive control (MPC) that iteratively performs optimization within an finite horizon (i.e., called predicting window). At each decision step, our algorithm determines the optimal building operations for every time step within the current prediction window, based on the known EV charging tasks, remaining battery energy and the current room temperature information. Typically for building MPC applications, the decision (time) step is between 15 minutes to 1 hour and the prediction window ranges from 3 to 72 hours.

At each decision step t, the optimization objective is to minimize the total energy cost within the prediction window, which includes both the total energy consumption cost and the peak power demand charge, as shown below in equation (2.28). In this objective function, the second term is not the actual peak power charge by utility company, but rather an approximation within the predicting window to heuristically lower the building peak power demand.

$$\begin{aligned} &\sum_{t=t_0}^{t_0+w-1} \left[p_g(t)e_g(t) + (p_b + p_g^{off}) \cdot discharge(t)\right] \\ &+p_p \cdot max\{e_g(t) + charge(t) | t \in [t_0, .., t_0 + w - 1]\} \end{aligned} \tag{2.28}$$

where $discharge(t)$ and $charge(t)$ denote the energy for battery discharging and charging, respectively. $p_g(t)$ and p_p represent the power grid time-of-use price and the peak demand charge price. p_g^{off} is the power grid off-peak price. $e_g(t)$ denotes the power grid energy consumption by operating HVAC system and charging EVs at decision step t. In the objective function, the first part consists of the power grid total electricity consumption cost and the battery usage cost. The second part represents the power gird peak demand charge cost. In this work, we assume that *the battery is charged to full capacity during*

power grid off-peak hours, and therefore the battery usage cost includes the battery charge cost based on the off-peak price p_g^{off} and the battery depreciation cost p_b.

Based on the above objective function, we will repeatedly solve the following MPC formulation at each decision step (note that a complete formulation will also include the constraints from (2.21) to (2.23) in section 2.2.1).

$$min \sum_{t=t_0}^{t_0+w-1} \left[p_g(t) \cdot e_g(t) + (p_b + p_g^{off}) \cdot discharge(t)\right] \tag{2.29}$$

$$+ p_p \cdot max\{e_g(t) + charge(t) | t \in [t_0, .., t_0 + w - 1]\}$$

$$T(t+1) = A \cdot T(t) + B \cdot u(t) + E \cdot dist(t) \tag{2.30}$$

$$U_{lower} \leq u(t) \leq U_{upper} \tag{2.31}$$

$$T_{lower}(t+1) \leq C \cdot T(t+1) \leq T_{upper}(t+1) \tag{2.32}$$

$$e^H(t) = (c_1|u(t)|^3 + c_2 u(t)^2 + c_3|u(t)| + c_4) \cdot P_{AC} \tag{2.33}$$

$$e_g(t) \geq e^H(t) + e^J(t) - discharge(t), e_g(t) \geq 0 \tag{2.34}$$

$$0 \leq discharge(t) \leq min\{U_N \cdot VOC(t)/R_b, B(t) - E_b\} \tag{2.35}$$

where $u(t)$ is the HVAC air flow output at step t. Positive $u(t)$ corresponds to heating and negative $u(t)$ models cooling [4]. Constraint (2.30) derives from the linear system description in equation (2.17). U_{lower} and U_{upper} bound the lower and upper air flow limit of the HVAC system, respectively. In constraint (2.31), T_{lower} and T_{upper} bound the room temperature comfort zone. Constraint (2.33) represents the HVAC energy consumption, which is a function of the HVAC air flow output [74]. Constraint (2.34) describes the relation among

[4] In this work, we only consider that case where the HVAC system works in the cooling mode.

grid energy consumption, battery usage, and energy consumption for EV charging and HVAC control. $e^H(t)$ denotes the energy consumption for HVAC control at step t. $e^J(t)$ denotes the EV charging energy consumption, which is calculated based on constraints (2.21), (2.22) and (2.23). Constraint (2.35) bounds the battery discharge rate, in which the upper bound of discharging rate at decision step t is determined by choosing the smaller one between the battery maximum discharging rate at step t and the battery residual energy $B(t) - E_b$. The battery maximum discharging rate is a function of the varying battery open circuit voltage and is defined similarly as constraint (2.14) in section 2.1.2. In this work, we assume that the battery is not allowed to discharge below the lower threshold E_b in order to protect the battery.

2.2.3 Experiments

A. Experiment Setup

We consider two different scenarios in our experiments in order to evaluate our algorithm under different energy demand profiles. In the first scenario, we assume there are 60 EV charging tasks in one day and the outside temperature ranges from $68°F$ to $90°F$. In the second scenario, we assume there are only 30 EV charging tasks in one day and the outside environment is cooler, ranging from $58°F$ to $75°F$. We set the decision (time) step to 1 hour and the prediction window to 8 hours. In each scenario, we repeat the experiment based on 100 sets of random EV charging tasks to measure the average performance. We also alter the capacity of battery storage to test the impact of battery capacity on cost reduction and determine the most efficient capacity. In this work, we consider the case

where the battery in the building is fully charged at an even rate during off-peak hours (i.e., 21 : 00 pm to 7 : 00 am), during which time the electricity price is low. Our MPC-based algorithm will optimally operate the HVAC, EV charging stations and the battery during day time to effectively reduce the peak power demand and electricity usage from power grid.

A. Experiment Results

(1) Scenario 1: We evaluate the co-scheduling algorithm performance based on an energy demand profile that has 60 EV charging tasks and temperature from $68°F$ to $90°F$. First, we consider the case in which there is no information for future EV arrivals (i.e., no reservation information). Figure 2.7 shows the experiment results under four different system configurations. In Figure 2.7a, we co-schedule HVAC control, EV charging and battery usage. In Figure 2.7b, we remove the battery storage from the system configuration to study the impact of battery on energy efficiency. In Figure 2.7c, we co-schedule HVAC control with battery usage, but set the charging rate of each EV to be fixed, i.e., each EV is charged at a constant rate from its arrival time to its departure time to fulfill its energy demand. We use such configuration to study the benefits of co-scheduling EV with HVAC and battery. Finally, in Figure 2.7d, we do not use battery storage and we fix the EV charging rate.

As shown in Figure 2.7, the red line represents the total energy demand requested by HVAC control and EV charging over time, and the blue line represents the total energy drawn from the power grid. In Figure 2.7a and Figure 2.7c, two vertical black lines divide the entire time period into three parts. The middle part represents for on-peak hours,

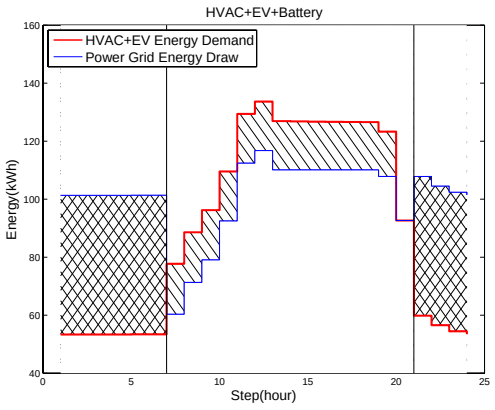

(a) HVAC, EV and battery co-scheduling

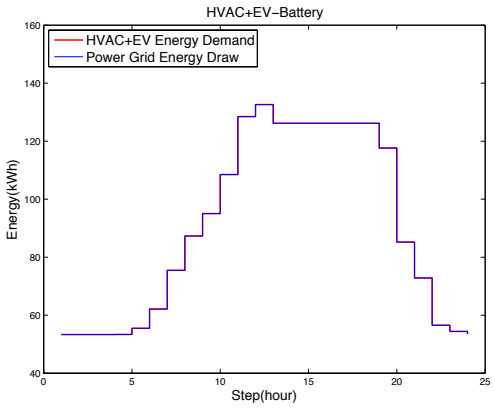

(b) HVAC and EV co-scheduling, no battery

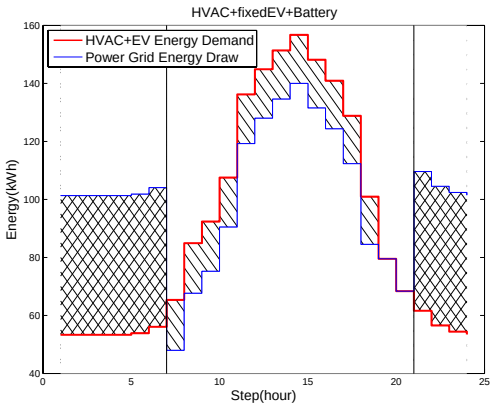

(c) HVAC and battery co-scheduling, fixed EV scheduling

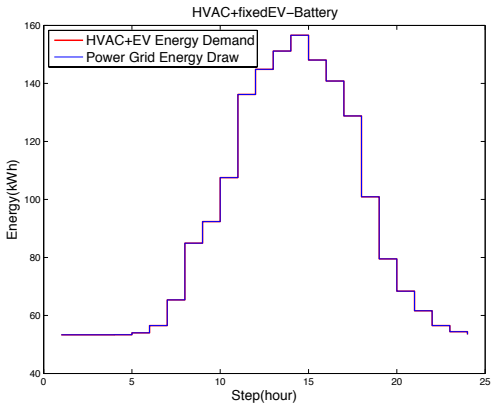

(d) HVAC scheduling, fixed EV scheduling, without battery

Figure 2.7: Energy scheduling in four system configurations under scenario 1 without future EV information

during which the battery will be optimally discharged to provide energy. The other two parts on the side correspond to off-peak hours, during which the battery will be evenly charged. The area marked by cross lines represents the energy released by battery storage, and the area marked by grid lines represents the energy used to charge battery storage. In Figure 2.7b and Figure 2.7d, we do not use battery, and therefore the energy demand curve (red curve) overlaps with the power grid energy curve (blue curve).

From Figure 2.7, we can clearly see the effectiveness of co-scheduling HVAC and EV in reducing peak demand from the grid (e.g., by comparing Figure 2.7a and Figure 2.7c), and the effectiveness of co-scheduling battery usage with the demand side scheduling (e.g., by comparing Figure 2.7a and Figure 2.7b), and the overall effectiveness of our approach (by comparing Figure 2.7a and Figure 2.7d). Table 2.4 shows the total energy cost and the peak demand charge for different configurations. Our co-scheduling approach (i.e., configuration (a)) provides 7.4% reduction in total energy cost, when compared with the baseline of no co-scheduling and no battery usage (i.e., configuration (d)). Furthermore, Table 2.4 also includes results for the case where the future EV arrivals within the prediction window are known. We can see that having the future EV arrival information provides significant reduction in peak demand but not much in total energy cost under this scenario. In practice, we may have some information of future EV arrivals but not the complete information, in which case the results are likely in between the two cases we have evaluated.

(2) Scenario 2: In the second scenario, we evaluate the co-scheduling algorithm performance under an energy demand profile in which there are 30 EV charging tasks in one day and the environment temperature ranges from $58°F$ to $75°F$. We also consider four

	No future EV information		Accurate future EV information	
	Total	Peak	Total	Peak
(a)	\$7290.3	\$803.3	\$7180.0	\$756.0
(b)	\$7564.7	\$912.4	\$7460.5	\$855.3
(c)	\$7577.3	\$963.3	\$7574.1	\$962.2
(d)	\$7877.4	\$1077.4	\$7877.4	\$1077.4

Table 2.4: Energy cost and peak demand charge for different system configurations under scenario 1: (a) HVAC, EV and battery co-scheduling, (b) HVAC and EV co-scheduling, no battery, (c) HVAC and battery co-scheduling, fixed EV scheduling, and (d) HVAC scheduling, fixed EV scheduling, no battery.

different system configurations similarly as in Scenario 1. Table 2.5 show the results for these four configurations under Scenario 2, either with no future EV arrival information or with accurate future EV arrival information within the prediction window. We can see that in this scenario, co-scheduling HVAC, EV and battery usage also reduces energy cost, although not as much as in Scenario 1, probably due to the lower energy demand from the HVAC under mild ambient environment and the less-intensive EV charging profile.

	No future EV information		Accurate future EV information	
	Total	Peak	Total	Peak
(a)	\$5752.2	\$707.6	\$5739.2	\$707.6
(b)	\$5842.7	\$596.1	\$5910.9	\$700.6
(c)	\$5866.3	\$750.4	\$5865.9	\$749.6
(d)	\$5958.5	\$658.3	\$5958.5	\$658.3

Table 2.5: Energy cost and peak demand charge for different system configurations under scenario 2: (a) HVAC, EV and battery co-scheduling, (b) HVAC and EV co-scheduling, no battery, (c) HVAC and battery co-scheduling, fixed EV scheduling, and (d) HVAC scheduling, fixed EV scheduling, no battery.

(3) Battery SOC: Figure 2.8 shows the battery SOC over time for the system configuration (a) (i.e., HVAC, EV and battery co-scheduling) under Scenario 1. The battery is being charged before 7 : 00 am and after 9 : 00 pm, which correspond to the off-peak hours. From 7 : 00 am to 8 : 00 pm, the battery is being discharged at its maximum rate because the cost of using battery is lower than the cost of drawing energy from the power grid. At the step from 8 : 00 pm, the battery is not being discharged, because the cost of using battery is higher than the cost of using power grid electricity.

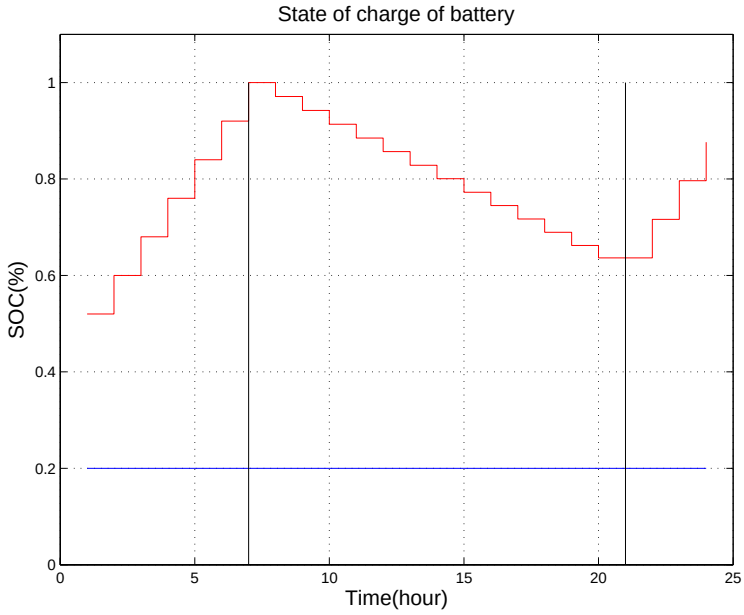

Figure 2.8: Battery SOC over time under scenario 1

(4) Energy cost reduction versus battery capacity: To study the impact of battery capacity on reducing energy cost, we change battery capacity from $50kWh$ to $900kWh$ and conduct experiments for the first system configuration (i.e., HVAC + EV + battery) under Scenario 1. We assume that the battery is charged to its full capacity during off-peak hours. The results are shown in Figure 2.9.

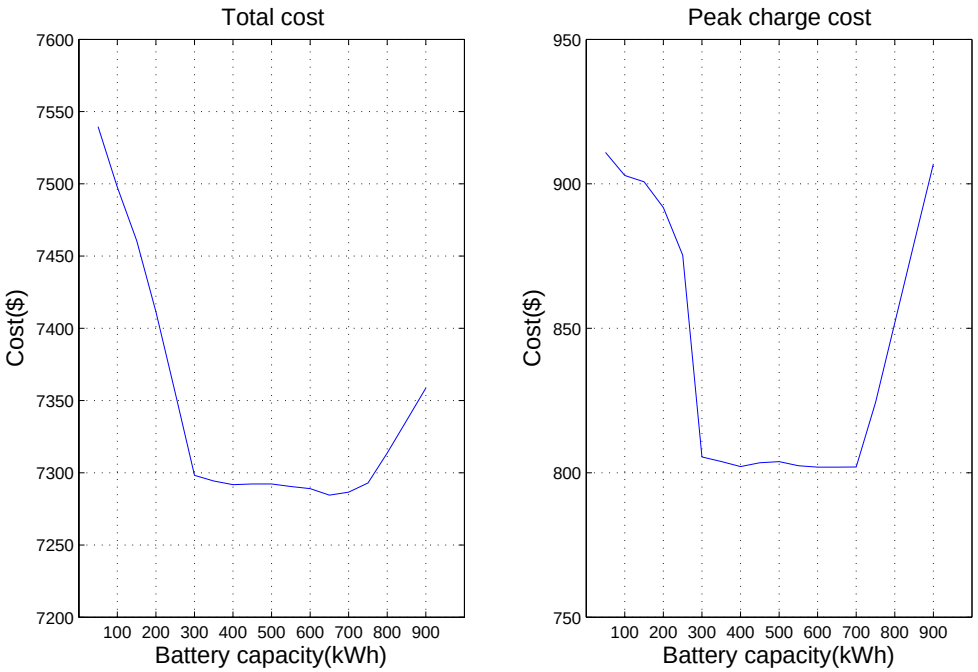

Figure 2.9: Total energy cost and peak demand charge cost versus battery capacity

We can see that with the increase of battery capacity, both the total energy cost and the peak demand charge cost are being reduced at the beginning. However, when the battery capacity is higher than a certain threshold (around 700 kWh), both costs start increasing. This is because the battery capacity is already sufficient for the energy demand in the building and additional battery capacity will become redundant. If we continue to increase the battery capacity and fully charge it during off-peak hours, it will lead to higher peak demand for the power grid and eventually results in higher total energy cost. Therefore, we need to carefully choose the appropriate battery capacity to achieve the optimal energy efficiency in the building.

2.3 Co-scheduling of Energy Loads in Building Clusters

In this section, we evaluate the efficiency of our MPC-based co-scheduling algorithm for energy management in building clusters. We first present an integrated model predictive control (MPC) formulation for co-scheduling energy demands (i.e., HVAC, EV charging) and battery storage usage for multiple buildings in a building cluster. Such integrated formulation may provide global optimal solutions to operate all flexible energy loads across the building cluster, however it has high computational complexity due to the large number of decision variables in the integrated formulation. Thus, we further consider a separate-scheduling heuristic, in which the energy management system of each building maximizes its own energy efficiency, while the shared battery storage resource is conceptually allocated to each building based on their historical energy consumption information.

2.3.1 System Models

A. Building Thermal Dynamics Model

One of the key requirements for buildings is to maintain the room temperature within a comfort range through operating the HVAC system. In this work, we adopt a RC-network based thermal dynamics model (similar as in section 2.1.1) to capture the heat transfer process in the building under the HVAC input and heat exchange with various environmental disturbances (e.g. ambient temperature, sun radiation and internal heat generation by human occupancy), similarly as in [18]. In our MPC-based optimization formulation, we use the model that is linearized around the system operating point by using Jacobian linearization method (details in [71]), and further transform it into the following

discrete time LTI system realization. Where A is the state transition matrix, B denotes the system input matrix, and E integrates the impact of various environmental disturbances.

$$x_{k+1} = Ax_k + Bu_k + Ed_k$$

$$y_k = Cx_k$$

B. Electric Vehicle Charging Model

In this work, we adopt a similar EV charging model as in section 2.2.1. We simplify our original EV charging model by directly determining the amount of electricity allocated to each EV at each decision step (in contrast, our original EV charging model in section 2.2.1 first maps the EV energy demand to intervals and then determines the energy consumption for EV charging at the decision step level), because even though in this work the total number of charging stations within the building cluster is similar as the experiment in section 2.2.1, each building only operates a portion of all EV charging stations (as shown in Table 2.7). Each EV charging task J_j is characterized by its departure time d_j and energy demand E_j similarly as in section 2.2.1. The following constraints (2.36) to (2.38) determines the energy demand for every EV at each decision step by ensuring that each EV charging task can be finished by its departure time d_j. Specifically, for every EV charging task J_j in the current charging task set $\mathcal{J}_k$, equation (2.36) guarantees that the remaining demanded energy E_j is provided before the departure time d_j. Constraint (2.37) bounds the maximum charging power for each EV. Equation (2.38) calculates the total energy consumption for EV charging at decision step t by adding up the energy demand of each EV charging task $e_j(t)$.

$$\sum_{t=k}^{d_j} e_j(t) = E_j \ \forall j \in \mathcal{J}_k \tag{2.36}$$

$$0 \leq e_j(t) \leq P_r \tag{2.37}$$

$$e_J(t) = \sum_{j \in \mathcal{J}_k} e_j(t) \tag{2.38}$$

C. Battery Storage Model

The following constraints (2.39) to (2.42) capture the battery storage characteristics. In this work, we take into account the battery round-trip efficiency and safety charging/discharging range. We can assume that the open circuit voltage of the battery is constant over time, because we prevent the overuse of battery by applying constraint 2.40.

$$SOC(t+1) = SOC(t) + \rho \cdot e_{g2b}(t) - e_b(t) \tag{2.39}$$

$$E^- \leq SOC(t+1) \leq E^+ \tag{2.40}$$

$$0 \leq e_b(t) \leq d_r \tag{2.41}$$

$$0 \leq e_{g2b}(t) \leq c_r \tag{2.42}$$

specifically, based on battery discharge energy $e_b(t)$ and charged energy by power grid $e_{g2b}(t)$, equation (2.39) updates state-of-charge of battery by considering the round-trip efficiency ρ. Constraint (2.40) sets the upper and lower threshold of available energy without causing demand to the battery. Constraints (2.41) and (2.42) bound the maximum power rate of discharging and charging process, respectively.

2.3.2 Building Cluster Energy Co-scheduling Algorithm

A. Co-scheduling Formulation

Based on the models introduced in section 2.3.1, we first develop an integrated MPC-based formulation for co-scheduling the flexible energy demand (i.e., HVAC system and EV charging) and the usage of battery storage within the entire building cluster, while satisfying requirements on building temperature, EV charging and battery usage.

$$min \sum_{t=k}^{k+w-1} \left[p_g(t) \cdot e_g(t) + p_b \cdot e_b(t)\right] + p_p \cdot \max_{t=k}^{k+w-1} e_g(t)/I \tag{2.43}$$

$$\forall t \in [k, k+w+1],\ \forall n \in [1, N]$$

$$\textbf{s.t:}\ T_n(t+1) = A \cdot T_n(t) + B \cdot u_n(t) + E \cdot d_n(t) \tag{2.44}$$

$$U_n^- \leq u_n(t) \leq U_n^+ \tag{2.45}$$

$$T_n^-(t+1) \leq C \cdot T_n(t+1) \leq T_n^+(t+1) \tag{2.46}$$

$$e_H(t) = \sum_{n=1}^{N} c_1 u_n(t)^3 + c_2 u_n(t)^2 + c_3 u_n(t) + c_4 \tag{2.47}$$

$$e_g(t) = e_H(t) + e_J(t) + e_{g2b}(t) - e_b(t) \geq 0 \tag{2.48}$$

The variable definitions of the MPC formulation are listed in Table 2.6. There are N buildings in the cluster. Objective function (2.43) minimizes the total energy cost of the cluster while reducing the peak electricity demand within a predicting window w. More specifically, the first term calculates the total energy consumption cost, including grid electricity cost and battery depreciation cost. The second term penalizes the peak energy demand with a factor p_p (in our experiments, p_p is determined based on the peak power charge from utility company [79]). Equation (2.44) calculates the temperature of each thermal zone in each

building n, where $u_n(t)$ is the conditioned air flow volume into the room. Constraint (2.45) sets bounds for $u_n(t)$. Constraint (2.46) depicts the temperature requirement for each room. Equation (2.47) calculates the HVAC energy consumption $\boldsymbol{e_H}(t)$ as a function of the air flow volume $u_n(t)$, based on the model from [74]. Constraint (2.48) captures the relation between grid electricity supply $e_g(t)$ and various energy demand, including the HVAC energy demand $e_H(t)$, the EV charging demand $e_J(t)$ (derived from equation (2.38)) and battery charging/discharging energy denoted by $e_{g2b}(t)$ and $e_b(t)$ respectively.

Table 2.6: MPC algorithm variables definition

k	current decision step	w	predicting window length
I	length of decision step	p_p	peak power demand penalty
d(t)	environment disturbances	p_b	battery depreciation cost
$u_n(t)$	conditioned air flow volume	$p_g(t)$	power grid electricity price
$T_n(t)$	system node temperature	$e_H(t)$	HVAC energy demand
$e_g(t)$	building grid electricity usage		
A_n, B_n, C_n, E_n	building thermal dynamics coefficient matrices		
U_n^-, U_n^+	air flow volume lower/upper bounds		
T_n^-, T_n^+	comfort zone temperature lower/upper bounds		
c_1, c_2, c_3, c_4	HVAC energy demand function coefficients		

The MPC formulation is solved at every decision step for the building cluster. Once the optimal operations are determined for the current predicting window, the decisions at the first decision step (i.e., $u(k)$, $e_J(k)$ and $e_B(k)$) are applied to operate the HVAC systems, charge EVs and manage the battery storage system. Next, each building will move the predicting window forward by one decision step and the co-scheduling formulation will be solved again.

B. Separate-scheduling Heuristic

The above co-scheduling formulation may achieve global optimality within the predicting window, however it results in high computation complexity. Thus, we also develop a separate-scheduling heuristic where each building conducts its own MPC-based optimization based on the following formulation:

$$min \sum_{t=k}^{k+w-1} \left[p_g(t) \cdot e_{g,n}(t) + p_b \cdot e_{b,n}(t)\right] + p_p \cdot \max_{t=k}^{k+w-1} e_{g,n}(t)/I \tag{2.49}$$

$$\forall t \in [k, k+w+1]$$

$$\textbf{s.t:} \quad T_n(t+1) = A \cdot T_n(t) + B \cdot u_n(t) + E \cdot d_n(t) \tag{2.50}$$

$$U_n^- \leq u_n(t) \leq U_n^+ \tag{2.51}$$

$$T_n^-(t+1) \leq C \cdot T_n(t+1) \leq T_n^+(t+1) \tag{2.52}$$

$$e_H(t) = c_1 u_n(t)^3 + c_2 u_n(t)^2 + c_3 u_n(t) + c_4 \tag{2.53}$$

$$e_{g,n}(t) = e_H(t) + e_{J,n}(t) + e_{g2b,n}(t) - e_{b,n}(t) \geq 0 \tag{2.54}$$

The main difference between the co-scheduling and the separate-scheduling heuristic lies in the management of battery storage. The co-scheduling formulation uses the entire battery storage capacity. While in the separate-scheduling case, the total battery storage capacity is heuristically allocated to each building based on their historical energy consumption characteristics (e.g., proportional to their average energy demand in the previous electricity bills). Then, each building conducts its own MPC-based optimization by only considering part of the battery capacity pre-allocated to that building.

2.3.3 Experiments

A. Experiment Setup

In our experiments, we consider a cluster of five buildings that are managed by the same institute. Each building operates its HVAC system to maintain the desired temperature for office zones, and also provides certain EV charging space for its tenants. In addition, there is certain amount of fixed load (e.g., lighting and operation of office equipment) consumption in each building. The configuration of different types of loads for each building is shown in Table 2.7. Moreover, it is assumed that the building cluster has installed a battery storage system.

Table 2.7: Load distribution in the building cluster

Building	1	2	3	4	5
HVAC Peak Demand (KW)	30	40	50	200	250
Fixed Load Peak Demand (KW)	5	10	15	30	40
Number of EV Charging Stations	5	5	10	15	15

B. Experiment Results

(1) Effectiveness of MPC-based building cluster co-scheduling: we first conduct experiments to evaluate the effectiveness of the MPC-based integrated formulation for energy co-scheduling. We compare the performance of our co-scheduling approach with a baseline strategy, in which the HVAC system is operated by an on-off controller (i.e., conditioned air flow cannot be changed continuously), each EV is charged at a constant rate during the entire charging period, and the battery is fully charged at night and evenly discharged

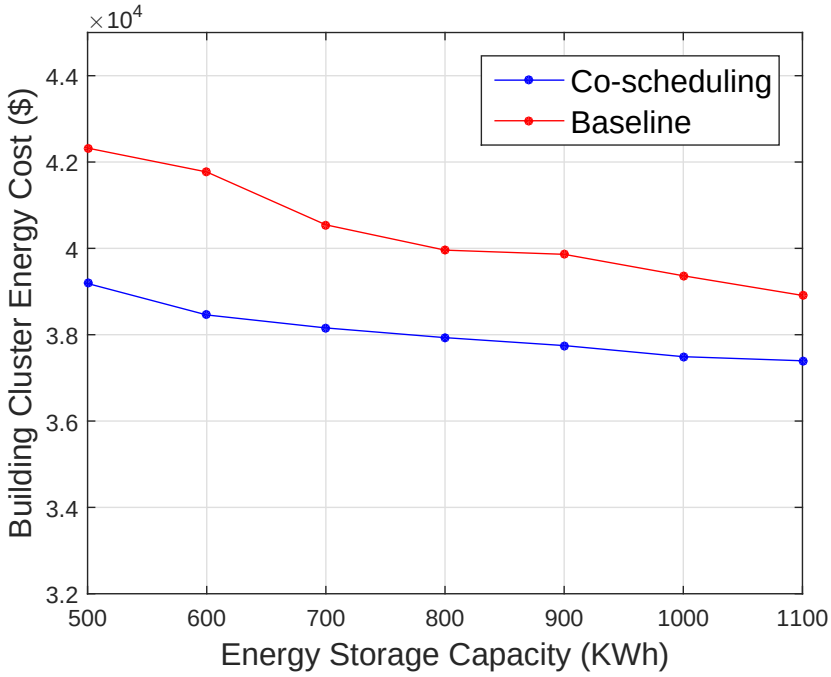

Figure 2.10: Comparison between co-scheduling and baseline

during on-peak hours. As shown in Figure 2.10, compared to the baseline approach, the co-scheduling formulation is able to significantly reduce the total energy cost of the building cluster, under different battery capacities. On average, 5.75% reduction can be achieved for total cost, and the peak power can be reduced by 8.21% in average. In this case, the total energy cost of the building cluster is minimized (although it is not guaranteed to achieve an optimal scheduling for each individual building).

(2) Evaluation of separate-scheduling heuristic: then, we evaluate the performance of the separate-scheduling heuristic by comparing it with the co-scheduling algorithm. In this study, we assume we have an accurate estimation of each building's energy consumption level based on historical information, and we distribute the battery storage capacity to

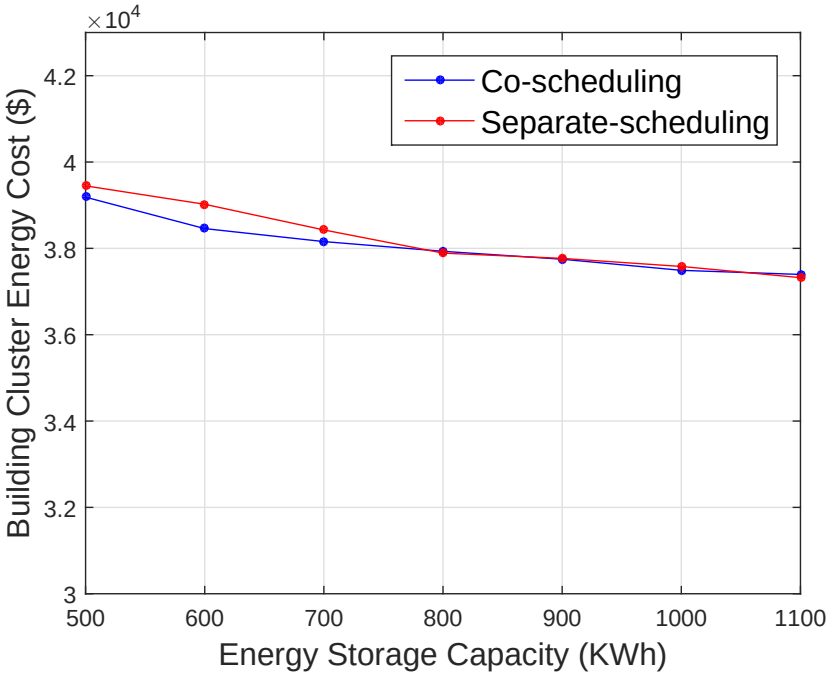

Figure 2.11: Comparison between co-scheduling and separate-scheduling approaches

each building in proportion to its historical consumption level. In Figure 2.11, we can see that the separate-scheduling heuristic can achieve similar performance as the co-scheduling formulation under different battery storage capacities (only 0.46% worse in average), when we have an accurate estimation of the building consumption level. However, the runtime of co-scheduling is 2.2× higher compared with the heuristic, and the difference in runtime will be more significant with increasing size of the building cluster.

(3) Impact of storage capacity allocation: finally, we conduct experiments to study the impact of battery storage capacity allocation. We consider another two cases where we do not have accurate estimation of building energy consumption level, and we allocate the battery storage capacity in two ways 1) evenly to each building, or 2) inversely proportional to each building's consumption level (an extreme case). We compare these two cases with

the above case where we allocate the battery capacity proportionally to each building's energy consumption level. As shown in Figure 2.12, the proportional allocation strategy

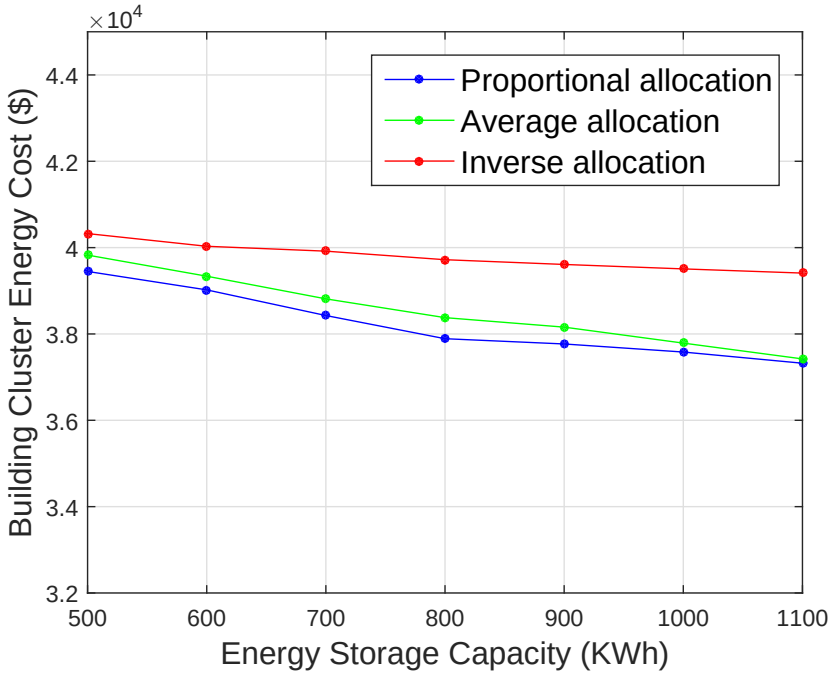

Figure 2.12: Total energy cost of building cluster by using separate-scheduling heuristic in different storage allocation scenarios

always achieves the lowest energy cost with different battery capacity. There is a only slight increase in the cost for the even allocation scenario (in average 0.77% higher), and a larger increase for the inversely proportional allocation case (in average 4.40% higher). Our experiment results demonstrate that proportionally allocating the battery resource among the building cluster and separately scheduling the flexible energy loads for each building could be a good heuristic approach, which can derive the near-optimum operating solution and significantly reduce the computational complexity.

2.4 Co-Scheduling of Datacenter and HVAC Loads in Mixed-Use Buildings

In this section, we address the problem of energy management for mixed-use buildings (MUBs), in which datacenter loads share the same set of HVAC devices (e.g., cooling tower, water pump, etc.) with office rooms. We also consider the case where limited renewable energy resources (i.e., solar power and battery storage) are shared between office loads and datacenter loads. In this work, we develop models for datacenter energy loads and present an MPC-based co-scheduling algorithm for improving the energy efficiency and reducing carbon footprint in MUBs by fully leveraging the intermittent renewable power sources. Figure 2.13 illustrates an overview of our modeling of the three major energy loads in an MUB with colocated datacenter server rooms.

- e_{IT}: energy demand from datacenter operations, including energy consumed by servers for data processing (e_{server}), by uninterruptible power supplies (e_{ups}), and by power distribution units (e_{pdu});
- e_h: energy demand from HVAC system, including energy consumed by air handling units (AHUs) in office rooms (which further includes $e_{fan,o}$ for delivering supply air and $e_{vent,o}$ for ventilation), by AHUs in datacenter rooms (which includes $e_{fan,dc}$ and $e_{vent,dc}$), and by shared cooling equipment such as water pump (e_{pump}), chiller ($e_{chiller}$) and cooling tower (e_{tower});
- e_m: energy demand from other miscellaneous loads that are assumed to be fixed in our model, including lighting system, office appliances, etc.

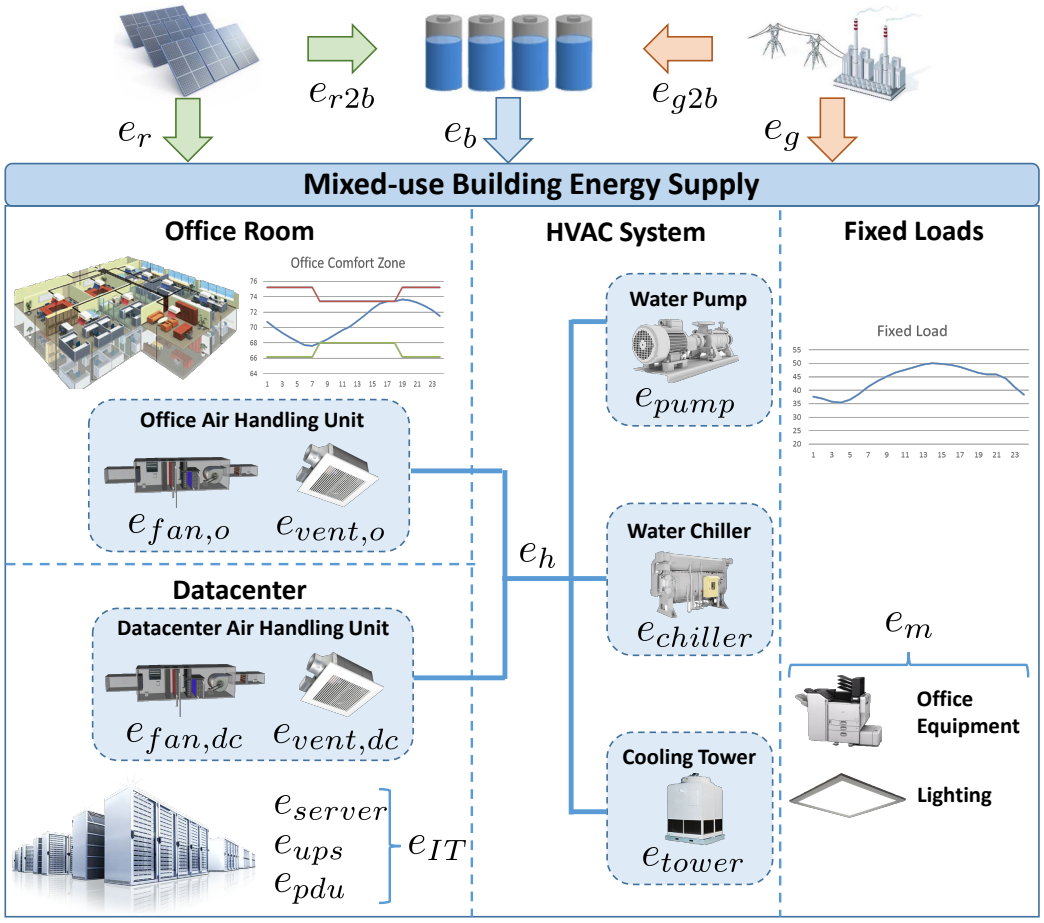

Figure 2.13: Energy modeling overview for MUBs

On the energy supply side, we consider energy provided by the power grid (e_g), by renewable sources (in particular solar energy e_r), and by battery storage (e_b). The battery storage system stores energy either from power grid during off-peak hours (e_{g2b}) or from excessive renewable sources (e_{r2b}), to help shave building's peak demand. In the next section, we will present the model of each type of energy load in details.

2.4.1 System Models

A. Building Thermal Dynamics and HVAC System Modeling

HVAC system is a major energy consumer in MUBs, and responsible for meeting the temperature and ventilation requirements for both office rooms and datacenter rooms. In this work, we consider HVAC cooling systems with separate AHUs for office rooms and for datacenter rooms, and while with shared water pump, chiller and cooling tower[5].

Figure 2.14 shows our model of air flow demand and supply in AHUs. The AHUs may take a mixed of outside fresh air and returned air [80], and cool it through cooling coil with chilled water, and serve it as supply air to building rooms for maintaining office room temperature and removing the server room heat generation. In addition, the AHUs need to input certain amount of outside air for ventilation purpose to ensure acceptable indoor air quality in office rooms, as required by the ASHRAE standard [81].

Next, we will first introduce our office room thermal dynamics model based on cooling supply air from the AHUs, and then present how we calculate the HVAC system energy demand based on the amount of needed supply air.

(1) Office room thermal dynamics model: we estimate the office room temperature changes based on a RC (resistor-capacitor) network model, similarly as in section 2.1.1. The network consists of wall nodes and room nodes, as shown in equation (2.56) and equation (2.55) respectively. Then, differential equations of room and wall nodes can be transformed into the following state space equation (2.57).

[5]There are also systems that use separate chillers, which can be treated as a special case of our formulation.

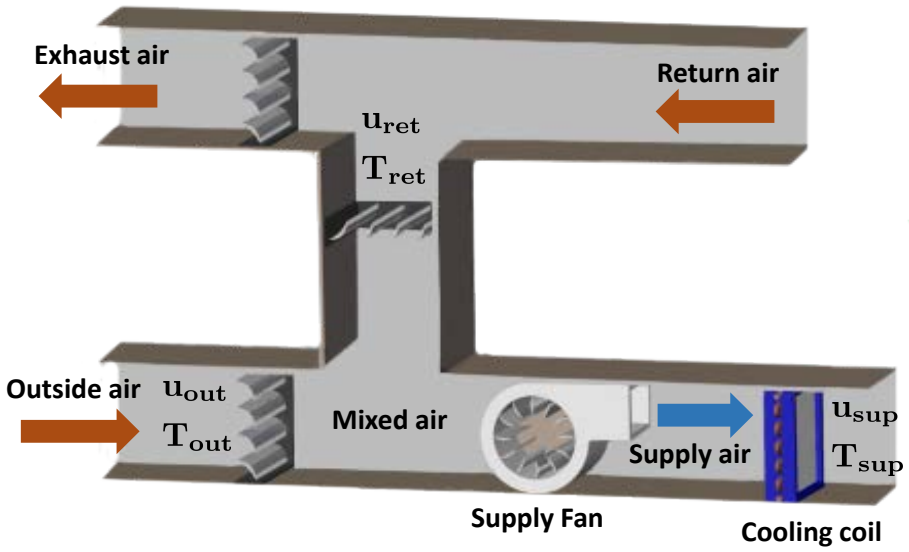

Figure 2.14: Overview of air flow demand and supply in air handling units

$$C_{r_i}\frac{dT_{r_i}}{dt} = \sum_{j\in\mathcal{N}_{r_i}}\frac{T_j - T_{r_i}}{R'_{ij}} + \dot{m}_{r_i}c_a(T_{s_i} - T_{r_i}) + \omega_i\tau_{\omega_i}A_{\omega_i}q''_{rad_i} + \dot{q}_{int_i} \tag{2.55}$$

$$C_{\omega_i}\frac{dT_{\omega_i}}{dt} = \sum_{j\in\mathcal{N}_{\omega_i}}\frac{T_j - T_{\omega_i}}{R'_{ij}} + r_i\alpha_i A_i q''_{rad_i} \tag{2.56}$$

$$\dot{\boldsymbol{x}}_{\boldsymbol{t}} = f(\boldsymbol{x}_{\boldsymbol{t}}, \boldsymbol{u}_{\boldsymbol{t}}, \boldsymbol{d}_{\boldsymbol{t}}); \quad \boldsymbol{y}_{\boldsymbol{t}} = \boldsymbol{C}\boldsymbol{x}_{\boldsymbol{t}} \tag{2.57}$$

where $\boldsymbol{x_t}$ is the state vector representing the temperature of each node (in this work, we use bold notation to denote a vector or matrix). $\boldsymbol{u_t}$ denotes the air mass flow into each room (corresponding to $\dot{m}_{r_i}$ in equation (2.55)). $\boldsymbol{d_t}$ captures the environment disturbance. Finally, $\boldsymbol{y_t}$ represents the temperature of each room node and is calculated out of system state $\boldsymbol{x_t}$. We use the nonlinear model in equation (2.57) as the plant model to estimate the actual temperature evolution in our simulation. While for efficient control in our MPC-

based formulation, we use the following linear representation, derived by linearizing the nonlinear dynamics model in (2.57) near its equilibrium operating points:

$$\boldsymbol{x_{t+1}} = \boldsymbol{A}\boldsymbol{x_t} + \boldsymbol{B}\boldsymbol{u_t} + \boldsymbol{E}\boldsymbol{d_t}; \quad \boldsymbol{y_t} = \boldsymbol{C}\boldsymbol{x_t} \tag{2.58}$$

where $\boldsymbol{A}$ is the system state coefficient matrix, $\boldsymbol{B}$ and $\boldsymbol{C}$ are control and output matrices respectively, and $\boldsymbol{E}$ integrates the impacts of various environmental factors.

For office rooms, we use equation (2.58) to determine the needed air mass flow $\boldsymbol{u_t}$ for maintaining the desired room temperature for building tenants. For datacenter rooms, we need a different model for calculating the air flow rate, which is presented later in section 2.4.1.

(2) Air flow constraints in air conditioning units: for both office rooms and datacenter rooms, following constraints set the requirements on ventilation and the bounds on supply air flow rate in AHUs. $\boldsymbol{u_{vent}}(t)$, $\boldsymbol{u_{out}}(t)$, $\boldsymbol{u_{ret}}(t)$ and $\boldsymbol{u_{sup}}(t)$ represent the ventilation air flow rate, outside air flow rate, return air flow rate, and supply air flow rate at decision step t (more strictly speaking, during the period of decision step t) in our discrete control model), respectively. Constraint (2.59) sets the minimum ventilation requirements $\boldsymbol{U_{vent}}$ for rooms that are served by each AHU. Constraint (2.60) represents the fact that the outside air and the return air are mixed and cooled through AHUs to generate the supply cooling air to rooms, as shown in Figure 2.14. $\boldsymbol{u_{sup}}(t)$ is determined by the total air mass flow input into rooms that are served by each AHU. Constraint (2.61) sets the lower and upper bounds for the supply air flow rate.

$$\boldsymbol{u_{vent}}(t) + \boldsymbol{u_{out}}(t) \geq \boldsymbol{U_{vent}} \tag{2.59}$$

$$\boldsymbol{u_{sup}}(t) = \boldsymbol{u_{out}}(t) + \boldsymbol{u_{ret}}(t) \tag{2.60}$$

$$\boldsymbol{U}^{-} \leq \boldsymbol{u_{sup}}(t) \leq \boldsymbol{U}^{+} \tag{2.61}$$

(3) Chilled water and condense water constraints: the thermal load in the building is first removed via heat exchange between supply air and chilled water that flows through AHUs. Then, condense water circulates in the loop between the chiller and the cooling tower to further release buildings' thermal load to the outside environment.

Equation (2.62) calculates the total thermal load $L_{heat}(t)$ that needs to be removed from the building by the HVAC system (through cooling the supply air for both office rooms and datacenter rooms). c_p^{air} denotes the heat capacity of air. $\boldsymbol{T_{out}}(t)$, $\boldsymbol{T_{ret}}(t)$ and $\boldsymbol{T_{sup}}$ denote the outside air temperature, return air temperature and supply air temperature, respectively. They are given as parameters in this work. Then, constraints (2.63) and (2.64) calculate the amount of chilled water and condense water needed for removing the building thermal load. T_{chws} and T_{chwr} denote the supply and the returned chilled water temperature, respectively. T_{cws} and T_{cwr} denote the supply and the returned condense water temperature, respectively. $m_{chw}(t)$ and $m_{cw}(t)$ denote the chilled water flow rate and the condense water flow rate, respectively.

$$L_{heat}(t) = (\boldsymbol{T_{out}}(t) - \boldsymbol{T_{sup}})^T \cdot \boldsymbol{u_{out}}(t) \cdot c_p^{air} + (\boldsymbol{T_{ret}}(t) - \boldsymbol{T_{sup}})^T \cdot \boldsymbol{u_{ret}}(t) \cdot c_p^{air} \tag{2.62}$$

$$(T_{chwr} - T_{chws}) \cdot m_{chw}(t) \cdot c_p^{water} = L_{heat}(t) \tag{2.63}$$

$$(T_{cwr} - T_{cws}) \cdot m_{cw}(t) \cdot c_p^{water} = L_{heat}(t) \tag{2.64}$$

(4) HVAC system energy demand: the energy demand of HVAC system includes the energy demand from chiller, water pump, cooling tower, and fans for cooling and ventilating purpose, as modeled in below.

$$e_{sup,o}(t) = \beta_1 \sum [u_{sup,o}^{(i)}(t)]^3, \ i \in \text{office fans} \tag{2.65}$$

$$e_{vent,o}(t) = \beta_1 \sum [u_{vent,o}^{(i)}(t)]^3, \ i \in \text{office fans} \tag{2.66}$$

$$e_{sup,dc}(t) = \beta_2 \sum [u_{sup,dc}^{(i)}(t)]^3, \ i \in \text{datacenter fans} \tag{2.67}$$

$$e_{vent,dc}(t) = \beta_2 \sum [u_{vent,dc}^{(i)}(t)]^3, \ i \in \text{datacenter fans} \tag{2.68}$$

$$e_{chiller}(t) = a_0 + a_1 m_{chw}(t) + a_2 m_{chw}(t)^2 + a_3 m_{chw}(t)^3 \tag{2.69}$$

$$e_{pump}(t) = b_0 + b_1 m_{chw}(t) + b_2 m_{chw}(t) + b_3 m_{chw}(t) \tag{2.70}$$

$$e_{tower}(t) = c_3 m_{cw}^3(t) \tag{2.71}$$

$$\begin{aligned} e_h(t) = {} & e_{sup,o}(t) + e_{sup,dc}(t) + e_{vent,o}(t) + e_{vent,dc}(t) \\ & + e_{chiller}(t) + e_{pump}(t) + e_{tower}(t) \end{aligned} \tag{2.72}$$

Equations (2.65) through (2.68) calculate the energy demand by fans for cooling and ventilation in office rooms, and by fans for cooling and ventilation in datacenter rooms, respectively, using the model in [17]. $u_{sup,o}^{(i)}(t)$ represents the total cooling air flow rate to office rooms that are served by AHU i, and $u_{vent,o}^{(i)}(t)$ denotes the total fresh air rate that is not

conditioned by the cooling coil within current decision step. $u^{(i)}_{sup,dc}(t)$ and $u^{(i)}_{vent,dc}(t)$ are similarly defined. Equations (2.69) through (2.71) calculate the energy demand by chiller, water pump and cooling tower, respectively, following the model in [82]. Note that $m_{chw}(t)$ and $m_{cw}(t)$ are calculated above in equation (2.63) and (2.64). Finally, equation (2.72) calculates the total HVAC energy demand.

B. Datacenter Modeling

We now model the datacenter IT energy demand (i.e., energy directly spent on IT equipment for computation), the delay performance constraint for its workloads, and the thermal load in datacenter for removing the generated heat. Our model is consistent with the existing literature [83, 84, 85] and captures the first-order effects of workload scheduling decisions on the datacenter energy.

$$e_s(t) = [x_a(t) + x_b(t)] \cdot e_0 \tag{2.73}$$

$$e_{IT}(t) = e_s(t) + \alpha \cdot e_s(t) \tag{2.74}$$

$$\frac{1}{\mu_a - \lambda(t)/x_a(t)} \leq D \tag{2.75}$$

$$x_b(t) \geq \frac{\sum_{i=1}^{j} b_i(t)}{\mu_b} \tag{2.76}$$

$$\sum_{t=A_i}^{A_i+N_i-1} b_i(t) = B_i \ , \ \forall i = 1...j \tag{2.77}$$

$$x_a(t) + x_b(t) \leq X \tag{2.78}$$

$$u_{dc}(t) = e_{IT}(t)/[(T_{ret,dc} - T_{sup}) \cdot c_p^{air}] \tag{2.79}$$

(1) IT energy demand: the energy demand of the servers $e_s(t)$ is calculated in equation (2.73) based on the average energy demand of a single server (denoted as e_0) [83] and

number of active servers processing interactive and batch workloads (denoted as $x_a(t)$ and $x_b(t)$, respectively). Note that the number of servers is approximated as continuous in this work, since a datacenter often houses hundreds to thousands of servers. Equation (2.74) calculates the total energy demand of IT equipments. It includes server energy demand $e_s(t)$, as well as energy demand of the supporting power equipments (power distribution units and uninterrupted power supplies) which is proportional to the server energy demand $e_s(t)$ and captured using a coefficient α. $e_{IT}(t)$, however, does not include the energy demand for running the AHUs in datacenter rooms, which is addressed later in equation (2.79).

(2) Workload constraints: datacenter processes both delay-sensitive interactive workloads and delay-tolerant batch workloads. Interactive workloads (e.g., web requests) require fast responses, whereas batch workloads (e.g., MapReduce) usually only have a deadline constraint. Constraint (2.75) determines the number of active servers for processing the interactive workloads based on the queueing model M/M/k to meet the performance constraint D [84]. μ_a and $\lambda(t)$ denote the maximum service rate and the arrival rate of interactive workloads, respectively. Constraint (2.76) determines the number of active servers for processing the batch workloads, where $b_i(t)$ denotes the amount of workload processed for the i-th batch job and μ_b denotes the maximum service rate for batch workloads. Equation (2.77) guarantees that each batch job B_i is finished within N_i decision steps since its arrival time A_i [83]. Constraint (2.78) bounds the maximum number of available servers. Aligned with existing literature [83, 84], we adopt a datacenter level control for our problem where the algorithm decides the number of servers to keep "ON" with performance constraint of (2.75) and (2.76). The server level job scheduling that captures other constraints

like data locality, can be considered as secondary control that takes the number of available sever as an input.

(3) Datacenter thermal model: we consider most of the energy consumed in server zone is converted into heat load [85], and calculate the amount of discharge air needed to remove the heat generated in the datacenter rooms in equation (2.79) which is then taken into account in equation (2.62) for calculating the total building thermal load.

2.4.2 Mixed-Use Buildings Co-Scheduling Algorithm

Based on the models developed in section 2.4.1, we present an online model predictive control (MPC) formulation to co-schedule the datacenter and the HVAC energy loads, with consideration of renewables and battery storage, for minimizing energy cost and satisfying operation requirements.

A. Co-scheduling Formulation

The MPC-based scheduling is optimized periodically. At each decision step t, a solution of control sequence is determined by minimizing the total energy cost within the current predicting window w, while meeting the office room comfort and datacenter service requirements. Then, only the first entry in the control sequence (the decision corresponding to decision step k) is implemented to operate building's flexible loads, i.e., control the HVAC system and the datacenter workloads. Next, the predicting window is advanced by one decision step, and the MPC-based scheduling is optimized again to determine the operation for the next decision step. Part of the MPC-based co-scheduling formulation is as below, while the rest of the formulation include equations (2.59) to (2.79) in section 2.4.1.

$$\min \sum_{t=k}^{k+w-1} [p_g(t)e_g(t) + p_b e_b(t)] + \hat{p}_g[\max_{t=k}^{k+w-1}[e_g(t)] - \hat{e}_g(t)]^+/I \tag{2.80}$$

$\forall t \in [k, k+w-1]$ subject to:

$$e_g(t) = e_{IT}(t) + e_h(t) + e_m(t) + e_{g2b}(t) - e_r(t) - e_b(t) \tag{2.81}$$

$$e_g(t) \geq 0 \tag{2.82}$$

$$\boldsymbol{T_c}(t+1) = \boldsymbol{A} \cdot \boldsymbol{T_c}(t) + \boldsymbol{B} \cdot \boldsymbol{u_{office}}(t) + \boldsymbol{E} \cdot \boldsymbol{d}(t) \tag{2.83}$$

$$\boldsymbol{T}^-(t+1) \leq \boldsymbol{C} \cdot \boldsymbol{T_c}(t+1) \leq \boldsymbol{T}^+(t+1) \tag{2.84}$$

$$e_r(t) + e_{r2b}(t) \leq E_r(t); e_{r2b}(t) \geq 0; e_r(t) \geq 0 \tag{2.85}$$

$$0 \leq e_b(t) \leq d_r \tag{2.86}$$

$$0 \leq e_{r2b}(t) + e_{g2b}(t) \leq c_r \tag{2.87}$$

$$S(t+1) = S(t) + \rho \cdot [e_{r2b}(t) + e_{g2b}(t)] - e_b(t) \tag{2.88}$$

$$E^- \leq S(t+1) \leq E^+ \tag{2.89}$$

Objective function: equation (2.80) defines the objective function for minimizing the total energy cost within the predicting window $(k, ..., k+w-1)$. The first term of the equation calculates the total energy consumption cost, including power grid electricity cost and battery depreciation cost. $p_g(t)$ denotes the grid electricity price at decision step t and $e_g(t)$ denotes the grid electricity consumed at t. p_b denotes the battery depreciation cost and $e_b(t)$ denotes the amount of energy discharged from battery at t.

The second term addresses the peak power demand charge. $\hat{e}_g(t)$ denotes the peak energy consumption of a decision step before the current step t. If the maximum energy consumption of any decision step within current predicting window exceeds $\hat{e}_g(t)$,

the amount of difference will be divided by the step length I to get average power demand and charged with a rate $\hat{p}_g$ (we use the peak power demand charge rate from utility company as $\hat{p}_g$). Then, $\hat{e}_g(t)$ will be updated to the new peak energy consumption. We should note that this second term is a heuristic to lower the peak power demand within the prediction window with an intent to eventually reduce the actual peak power charge over a month.

Energy demand/supply constraints: equation (2.81) balances the energy demand and supply. That is, the total energy demand from the datacenter energy demand $e_{IT}(t)$, the HVAC system demand $e_h(t)$, the fixed load demand $e_m(t)$ and the battery charging demand $e_{g2b}(t)$, minus the renewable energy supply (solar energy in this work) $e_r(t)$ and the battery energy supply $e_b(t)$, should be equal to the grid electricity demand $e_g(t)$. Constraint (2.82) requires the grid electricity consumption to be non-negative, since in our model we assume the building does not inject energy back to the grid. The datacenter energy demand $e_{IT}(t)$ and the HVAC system energy consumption $e_h(t)$ are calculated in equations (2.74) and (2.72), respectively, as defined in section 2.4.1.

Office room temperature constraints: equation (2.83) shows the linearized room temperature model (a simple rewriting of equation (2.58)). The room temperatures in the next decision step are estimated based on the current temperatures, air mass flow input $\boldsymbol{u_{office}}(t)$, and the environmental disturbances $\boldsymbol{d}(t)$ (e.g., sun radiation intensity, human occupancy and ambient temperature). Constraint (2.84) ensures that the office room temperature will not violate the comfort zone requirement.

Solar energy constraints: when solar energy is available during daytime, it can be applied to meet the building's energy demand. Moreover, the excessive energy may be stored in

the battery storage system. Constraint (2.85) ensures that the solar energy usage does not exceed the available solar energy $E_r(t)$ and is non-negative.

Battery storage constraints: constraint (2.86) sets the maximum discharging rate d_r for the battery. Constraint (2.87) sets the maximum charging rate c_r for the battery. As shown in Figure 2.13, charging energy may come from the grid (denoted by $e_{g2b}(t)$) or from the renewables (denoted by $e_{r2b}(t)$). Equation (2.88) updates the state of charge of the battery, denoted by $S(t)$, where ρ is the round trip efficiency. Constraint (2.89) ensures that the state-of-charge should be within a specified range for the purpose of safety and efficient battery usage.

B. Adaption for Carbon Footprint Optimization

In addition to reducing the total energy cost, carbon footprint is another important metric as many MUBs, especially those pro-sustainability MUBs, are actively seeking green certifications. Due to the heterogeneous and time-varying composition of energy sources in producing grid power (e.g., solar, nuclear and thermal power), the carbon footprint per kilowatt (i.e., carbon efficiency) may vary significantly throughout the day [86]. More importantly, carbon efficiency differs from electricity cost efficiency (e.g., coal-produced electricity is inexpensive but very carbon-intensive), and hence we need to factor carbon footprint into our co-scheduling decisions as a new metric [86]. Towards this end, we extend the objective function in (2.80) to the following equation (2.90) to make a trade-off between the carbon footprint and the total energy cost. We use a weight w_c to convert carbon footprint into an equivalent monetary value to indicate the relative importance of carbon emissions, and also to trade off between carbon footprint and energy cost.

$$\textbf{min} \sum_{t=k}^{k+w-1} [p_g(t)e_g(t) + p_b e_b(t) + w_c \cdot p_c(t)e_g(t)] + \hat{p}_g[\max_{t=k}^{k+w-1}[e_g(t)] - \hat{e}_g(t)]^+/I, \quad (2.90)$$

$p_c(t)$ is the average carbon efficiency calculated based on the energy fuel mix at time t [86].

2.4.3 Experiments

A. Experiment Setup

Our grid electricity price profile is a practical time-of-use tariff with three tiers of price [79] to bill business customers whose power demand is between $200KW$ and $500KW$, a typical range for small to medium MUBs. Moreover, customers' peak power demand within a month is charged at a rate of $\$16.37/KW$ (this rate is used as $\hat{p}_g$ in the objective function). In the MPC-based formulation, the decision step length I is set to one hour and the predicting window spans 24 steps (i.e., $w = 24$).

For datacenter, we use I/O traces from 6 RAID volumes in Microsoft Research (MSR) at Cambridge as the batch workload [87]. For interactive workloads we use traces from server usage log of Florida International University (a large public university in the U.S.) [6]. In practice, the interactive workload may be estimated based on historical workload trace. In our experiment, we vary the ratio between interactive and batch workloads, the percentage of batch workload takes up from 20% to 80%. The delay tolerance D of interactive workload is set to $50ms$. For batch workload, each job is required to be finished

[6]We also tried another workload trace from Google's publicly available real-time traffic data [88] and the results demonstrate similar trends. We only report the results from the university traces here due to space limitation (and also because they are better representatives of datacenter workloads in MUBs).

before its deadline (set to 24 hours in our experiments). The maximum service rate of each server is set to 100 requests per second, and the maximum power demand of each server is $0.4KW$. The office comfort temperature range is set to $20°C - 23°C$ during day time, and relaxed to $19°C - 24°C$ at night due to low occupancy activities [89].

Based on Tesla's PowerWall battery storage system [90], the battery depreciation cost p_b is set to $0.09\$/KW$, and its round-trip efficiency is set to 92%. The battery capacity is set to $300KWh$, and its state of charge thresholds are 20% and 80% of its capacity, respectively. The maximum amount of charging/discharging energy in one hour is set to 25% of its capacity. The peak solar power supply during the day time is set to $150KW$, which is around 50% of the building's average power demand. The solar power is proportional to the solar radiation. We take the solar radiation data from [91] for June, 2010 (the latest available data year).

In the following, we compare our co-scheduling approach with a baseline approach where datacenter loads and office room HVAC are scheduled separately using MPC to reduce energy cost. More specifically, for the separate scheduling approach, we divide the co-scheduling formulation introduced in section 2.4.2 into two MPC-based formulations, one for scheduling datacenter operations (and the corresponding HVAC activities) and the other for scheduling office room HVAC. All experiments are simulated for one month to take into account of the monthly peak demand charge. We first study the case where 80% of requests in datacenter are batch workload, and then we explore other scenarios with higher interactive workload percentage.

B. Experiment Results

(1) Effectiveness of co-scheduling without renewables and battery: first, we conduct experiments to evaluate the effectiveness of our co-scheduling formulation, without considering renewables and battery storage. The initial estimated value of the peak energy consumption within a decision step [7], i.e., $\hat{e}_g$ in the objective function (2.80), is set to $350KWh$ based on the analysis of simulation data (in practice, it could be estimated based on historical data). In the separate scheduling approach, this value is proportionally reduced based on the demands of datacenter operation and of office room HVAC control.

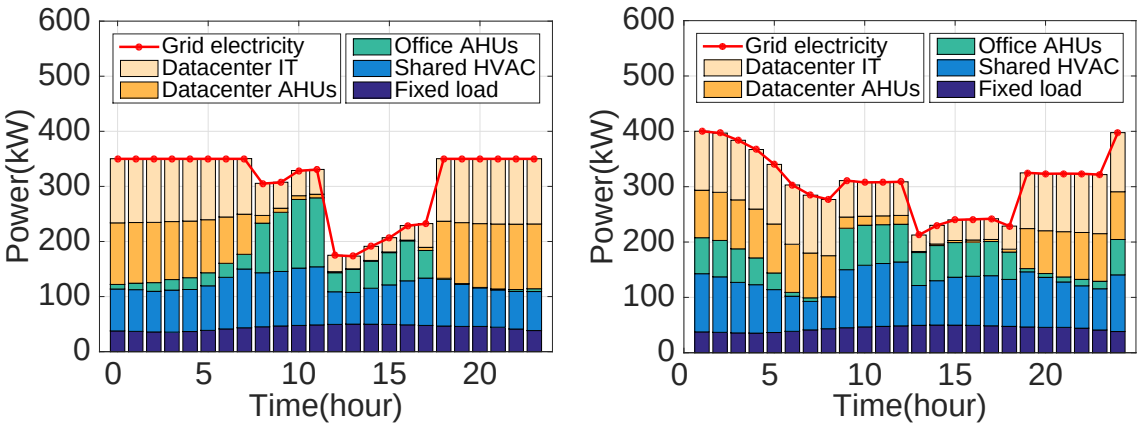

(a) Co-scheduling

(b) Separate scheduling

Figure 2.15: Power consumption of co-scheduling and separate scheduling without renewables and battery

Figure 2.15 shows the power consumption comparison between co-scheduling and separate scheduling approaches in a weekday. Various energy demand types are represented with different colors, including datacenter IT operations, datacenter AHUs, office room

[7]Because the length of decision step I is set to one hour in our experiment, we will use *initial estimated peak power* interchangeably in the following sections.

AHUs, shared HAVC (chiller, water pump, cooling tower), and fixed load. The red curve shows the total grid electricity usage. From the figure, we can see that our co-scheduling approach is more effective in reducing the energy consumption during peak hours from $12:00$ pm to $5:00$ pm and in reducing peak demand. In contrast, the baseline separate scheduling approach has a higher energy consumption during peak hours and al so higher peak demand, due to the lack of coordination between datacenter load scheduling and office room HVAC control.

Next, we vary the initial estimated peak power from $250KW$ to $450KW$ and evaluate the performance of our co-scheduling approach in different cases.

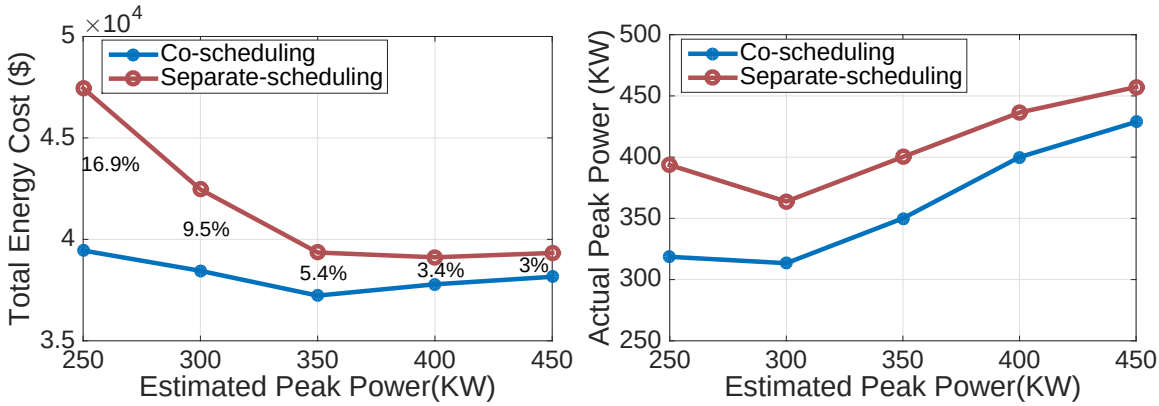

(a) Total monthly cost

(b) Actual peak power demand

Figure 2.16: Comparison between co-scheduling and separate scheduling in energy cost and peak power demand under various initial estimated peak power (energy cost reduction percentage is shown in the figure)

Figure 2.16 shows the comparison of total monthly energy cost (including energy consumption cost and peak demand charge) and actual peak power demand between co-

scheduling and separate scheduling approaches. We can see that the initial estimated peak power has significant impact on the total energy cost and on the eventual peak demand. Furthermore, in all cases, the co-scheduling approach can significantly reduce the total energy cost and peak power demand, compared with separate scheduling.

(2) Effectiveness of co-scheduling in leveraging renewables: next, we conduct experiments to evaluate the effectiveness of our co-scheduling approach in leveraging renewables (solar energy in this case). As stated before, we assume a solar energy profile with $150KW$ peak supply. For the separate scheduling approach, we assume the solar energy is proportionally allocated to datacenter and office rooms, based on the estimation of their demands.

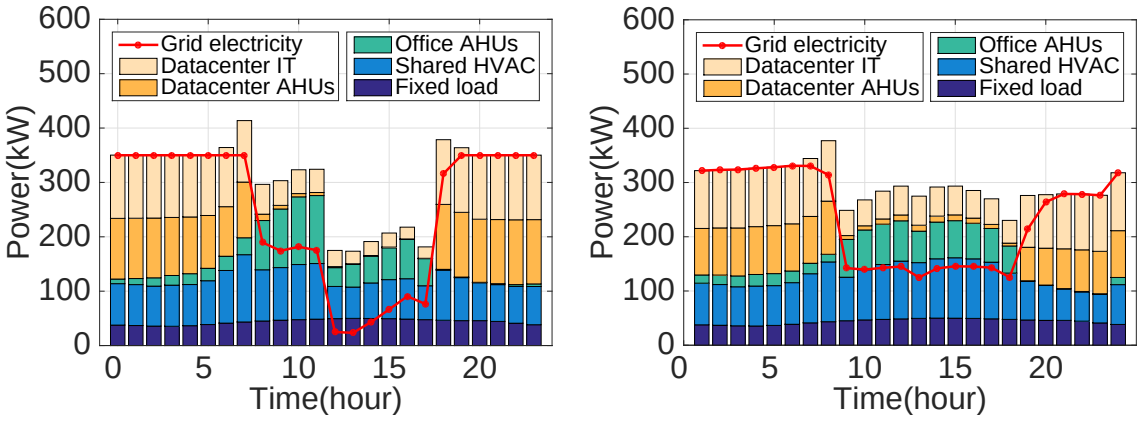

(a) Co-scheduling

(b) Separate scheduling

Figure 2.17: Power consumption of co-scheduling and separate scheduling with solar energy supply

Figure 2.17 shows the power consumption comparison between co-scheduling and separate scheduling approaches in a weekday with solar energy supply, with initial estimated peak power demand set to $350KW$. We can see that our co-scheduling approach is much

more effective in leveraging the solar energy for reducing energy demand to the grid during peak hours.

Figure 2.18 shows the comparison under various initial estimated peak power demand. As shown in the figure, *our co-scheduling approach can achieve a* 14.2% *cost reduction at the lowest total energy cost point, compared with the separate scheduling approach.* In addition, compared with the co-scheduling case without renewables, a 31.5% cost reduction is achieved in average.

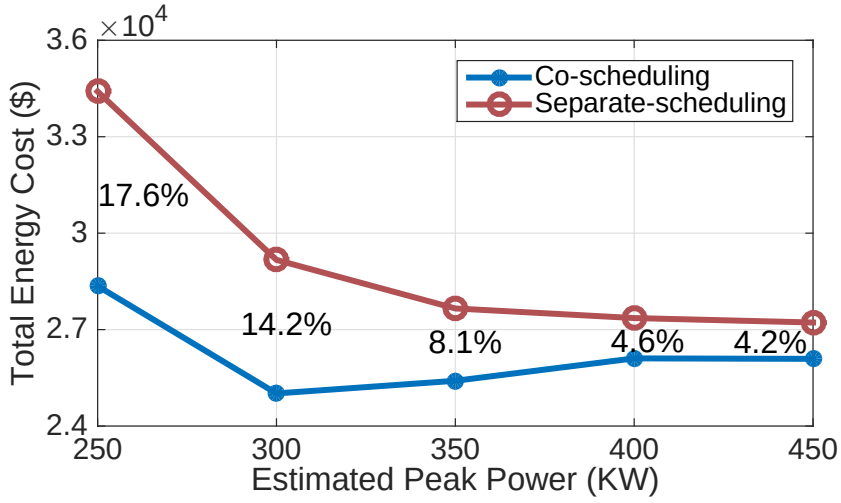

Figure 2.18: Comparison between co-scheduling and separate scheduling (with solar energy supply) in energy cost (energy cost reduction percentage is shown in the figure)

(3) Joint consideration of renewable energy supply and battery storage system: we also conduct experiments to compare co-scheduling and separate scheduling approaches with solar power (peak supply at $150KW$) and battery storage system ($300KWh$ capacity), and with initial peak power demand set to $350KW$. For separate scheduling, the battery capacity is proportionally allocated to datacenter and office rooms based on their demands.

Experimental results show that our co-scheduling approach is more effective than the separate scheduling approach, with a 11.8% monthly energy cost reduction. Compared with the co-scheduling case with solar but without battery, an additional 4.1% cost reduction can be achieved. Figure 2.19 shows the charging/discharging energy of battery in each decision step in both co-scheduling and separate scheduling approaches. We can see that our co-scheduling algorithm can better leverage the battery by charging the battery from grid and solar power during off-peak hours, and discharging the battery during peak hours.

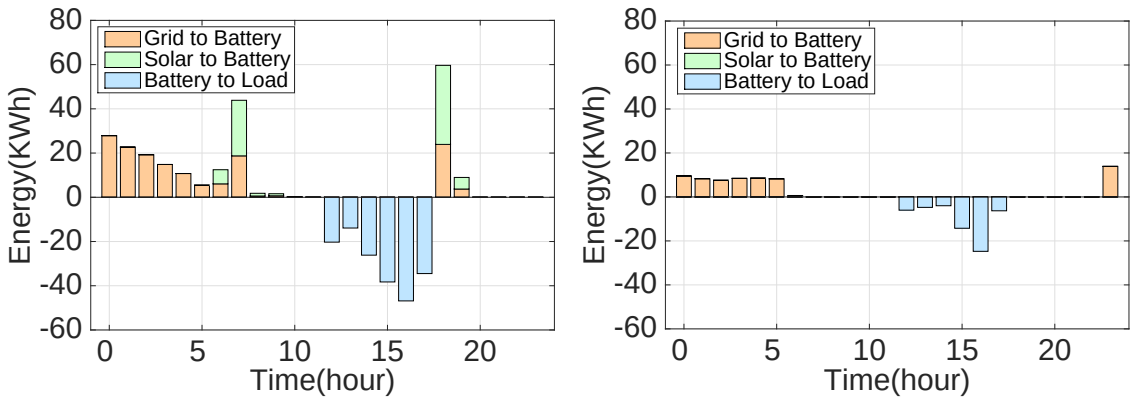

(a) Co-scheduling

(b) Separate scheduling

Figure 2.19: Comparison of battery charging/discharging between co-scheduling and separate scheduling approaches

(4) Effectiveness of co-scheduling with different percentage of batch workload: we also evaluate the effectiveness of our co-scheduling approach with different ratios between interactive and batch workload. We reduce the total amount of batch workload from 80% to 20% among all workload, and evaluate the cost reduction co-scheduling can achieve (with respect to separate scheduling) under various initial estimated peak power.

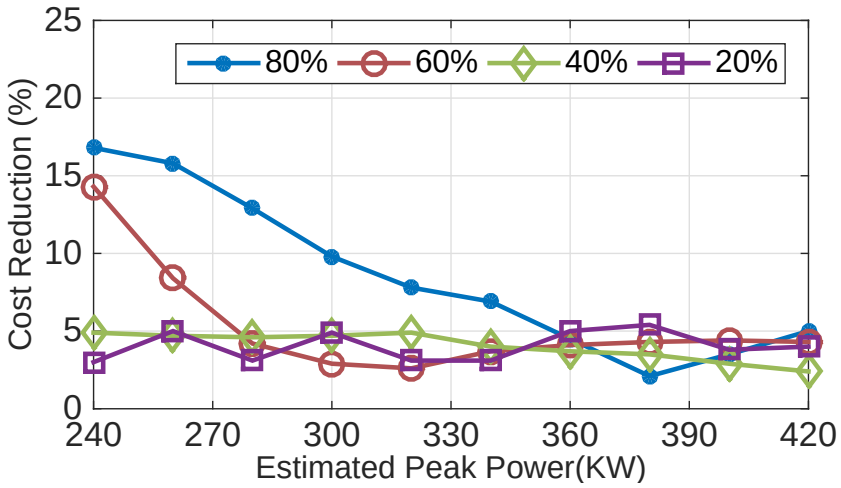

Figure 2.20: Cost reduction under different batch workload ratios

As shown in Figure 2.20, our co-scheduling approach can achieve more cost reduction compared to separate scheduling when there is higher level of batch workload. The performance of co-scheduling becomes insensitive to the initial estimated peak power when the percentage of batch workload decreases. That is because less scheduling flexibility can be provided by datacenter with a small fraction of batch workload.

(5) Consideration of carbon footprint: as introduced in section 2.4.2, our co-scheduling formulation may also be used for reducing carbon footprint, using an extended objective function as shown in equation (2.90). Figure 2.21 shows the carbon footprint and energy cost of co-scheduling and separate scheduling approaches under different values of weight w_c. Initial estimated peak power is set to $350KW$ to study the trade-off between carbon footprint and energy cost without renewables or battery storage. From Figure 2.21, we can see that the co-scheduling approach is more effective in reducing carbon footprint, at the expense of higher energy cost.

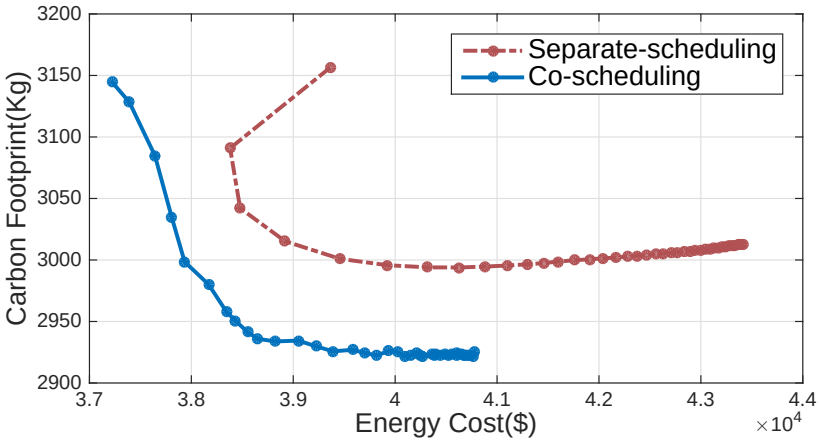

Figure 2.21: Carbon footprint and energy cost of co-scheduling and separate scheduling

Chapter 3

Proactive Demand Participation of Smart Buildings in Smart Grid

In this chapter, we fully take advantage of the energy flexibility provided by smart buildings and integrate it with the electricity market optimization to further improve the overall power grid power efficiency. In section 3.1, we present a novel proactive demand participation demand response (DR) scheme to enable building customers actively participate in the wholesale electricity market operation [67, 92, 66]. In section 3.2, we analyze the security issues and evaluate the effectiveness and robustness of our proactive DR scheme against several possible security attacks, and demonstrate its robustness compared with conventional passive DR strategies [68].

3.1 Proactive Demand Participation of Smart Buildings

In this section, we present our proactive demand response (DR) strategy which enables the customers actively participate in the decision process in the whole-sale electricity market, and thus further improves the overall energy efficiency across the entire power grid. Our integrated market operations framework with proactive demand participation from smart buildings is illustrated in Figure 3.1. The framework integrates demand response and network optimization across three levels of the smart grid – individual (building) customers, distribution system, and transmission system – through the interactions of three key decision making entities, including intelligent building energy scheduling agent, distribution system operator/customer aggregator and wholesale market operator. We will first briefly introduce these three key components as follows and present the details of each phase later in section 3.1.1.

(1) Intelligent building energy scheduling agent: at the building customer level, intelligent energy scheduling agent is designed to reduce energy cost and enable proactive demand participation. First, as part of the building automation and control system, the agent minimizes the building operating energy cost by scheduling the energy consumptions of various subsystems and controlling the usage of heterogeneous energy supply sources, while satisfying the requirements from building occupants. In this work, we address the scheduling of HVAC systems and battery storage systems with an MPC control algorithm.

Then, the agent constructs demand bid curves that capture the potential building energy demand under various possible grid electricity price. Those demand bid curves will then be sent to the distribution system operator/customer aggregator via wide-area network.

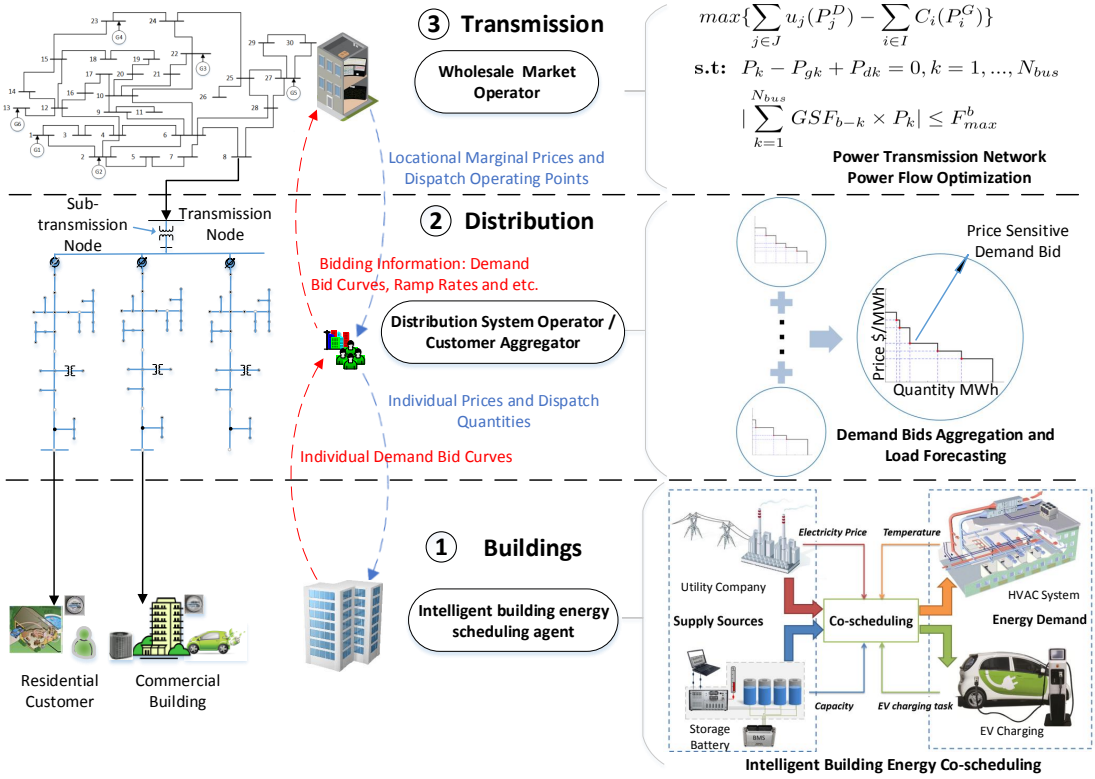

Figure 3.1: Overview of proactive demand response scheme

After the day-ahead and real-time markets are cleared by the electricity wholesale market operator, the building intelligent agent will receive the dispatch operating points in the same way as a regular power plant. By following the total electricity dispatch instruction, the intelligent agent will then coordinate various flexible loads to determine the amount of electricity that should be allocated to each of them.

(2) Distribution system operator/customer aggregator: the number of building customers in a regional electricity market could easily add up to millions. It is inefficient and impractical to deal with every individual customer's demand bid curve directly in the elec-

tricity market. To reduce the complexity of unit commitment and economic dispatch process when flexible load demand bids are considered, distribution system operator/customer aggregator needs to accurately aggregate individual demand bid curves at the substation level. Namely, the distribution system operator needs to find a set of equivalent overall demand bids which reflect integral demand bid characteristics of all individual customers at the transmission interconnection node while considering the physical models of distribution system. In the distribution system, there could exist participations from both proactive customers and passive customers who do not participate in the proactive demand bid program. To deal with the mixed customer structure, it is essential for distribution system operator/customer aggregator to predict the flexible load demand from passive customers based on smart meter data and current weather information.

The demand bid aggregation process follows an iterative process if the distribution network is radial. The load at downstream node could be related to upstream node by considering distribution network losses [44]. The locational marginal price (LMP) at the downstream nodes could depend on the transmission interconnection nodes when marginal distribution losses due to power injection at the downstream node is considered [45]. Finally, the aggregated demand bid information will be incorporated into the day-ahead and real-time market clearing process. After these markets are cleared, the distribution system operator is responsible for disaggregating the distribution system dispatch operating point into individual customers.

(3) Wholesale market operator: currently, in most independent system operators' five-minute real-time operations, demand is treated as fixed injection into the power network.

The wholesale market operator typically uses very short-term load forecasting algorithm to estimate total load in a region and then disaggregates the total load to individual nodes based on load distribution factors estimated from state estimation solutions. In our integrated market operations framework, the distribution system operators will submit demand bids at each transmission interconnection point as described above. The aggregated demand bid represents overall willingness to pay of all customers under the same pricing node. Therefore, apart from minimizing the total purchase cost of energy and ancillary services, the market operator will also try to maximize the sum of expected surplus of both generators and customers. The wholesale market operator is responsible for sending the dispatch operating points of the aggregated demand bids back to the distribution system operator.

3.1.1 Design of Proactive Demand Participation Framework

In this section, we introduce the design details of our framework. We first present the intelligent energy scheduling algorithm at the building customer level, the creation and aggregation of demand bid curves for individual buildings. Next, we illustrate the market operation optimization at the network level and disaggregation of dispatching points. Then, we present our proactive demand participation scheme.

A. Intelligent Building Energy Scheduling

At individual building customer level, it has been shown in chapter 2 that appropriately managing flexible energy loads such as HVAC systems and battery storage can effectively reduce both peak power demand and total energy cost of buildings. Furthermore,

it is also essential to coordinate the building energy consumption behavior collaboratively in a holistic formation to maximize power grid efficiency. Next, we will first introduce our building thermal dynamics model, the MPC-based building energy scheduling algorithm that addresses both HVAC control and battery storage usage based on the proof-of-concept formulation presented in section 2.1.

(1) Building thermal dynamics model: we use a building thermal dynamics model similarly as in section 2.1, where a building is considered as a network. The building can be modeled by using two types of nodes: walls and rooms. The temperature of each wall node and room node can be modeled by equations (3.1) and (3.2).

$$C_{\omega_i}\frac{dT_{\omega_i}}{dt} = \sum_{j\in\mathcal{N}_{\omega_i}}\frac{T_j - T_{\omega_i}}{R'_{ij}} + r_i\alpha_i A_i q''_{rad_i} \tag{3.1}$$

$$C_{r_i}\frac{dT_{r_i}}{dt} = \sum_{j\in\mathcal{N}_{r_i}}\frac{T_j - T_{r_i}}{R'_{ij}} + \dot{m}_{r_i}c_a(T_{s_i} - T_{r_i}) + \omega_i\tau_{\omega_i}A_{\omega_i}q''_{rad_i} + \dot{q}_{int_i} \tag{3.2}$$

As mentioned in section 2.1.1, the above heat transfer differential equations of walls and rooms can be transformed into the following linear state space equation (3.3), by linearizing and discretizing the state space realization by following the methods discussed in section 2.1.

$$x_{k+1} = Ax_k + Bu_k + E\hat{d}_k \tag{3.3}$$

$$y_k = Cx_k$$

In equation (3.3), A is the system state coefficient matrix, B and C are control and output matrices respectively, while matrix E combines the impacts of various environmental factors on room temperature. The original nonlinear model is used for state estimation and calculating the actual temperature evolution in our simulation. While for control purpose, we

use the linear thermal dynamics model to capture the building heat transfer characteristics and develop the MPC-based building energy scheduling algorithm as follows.

(2) MPC-based building energy scheduling algorithm: based on the building thermal dynamics model, we formulate an MPC-based control algorithm to co-schedule the HVAC control and the battery storage usage for reducing energy cost, while meeting HVAC system requirements on room temperature and airflow:

$$min \sum_{t=i}^{i+w-1} \left[p_g(t) \cdot e_g(t) + p_b \cdot e_b(t)\right],\ \forall t \in [i, i+w+1] \tag{3.4}$$

$$\textbf{s.t:}\ T_c(t+1) = A \cdot T_c(t) + B \cdot u(t) + E \cdot \hat{d}(t) \tag{3.5}$$

$$U^- \leq u(t) \leq U^+ \tag{3.6}$$

$$T^-(t+1) \leq C \cdot T_c(t+1) \leq T^+(t+1) \tag{3.7}$$

$$e_g(t) = e_H(t) + e_B(t), e_g(t) \geq 0 \tag{3.8}$$

$$e_H(t) = c_1 u(t)^3 + c_2 u(t)^2 + c_3 u(t) + c_4 \tag{3.9}$$

$$-d_r \cdot \tau \leq e_B(t) \leq c_r \cdot \tau \tag{3.10}$$

$$Soc(t+1) = (1-\gamma) \cdot Soc(t) + \rho \cdot e_B(t) \tag{3.11}$$

$$E^- \leq Soc(t+1) \leq E^+ \tag{3.12}$$

$$Soc(t+1) = E_0, \text{if } t \bmod N = 0 \tag{3.13}$$

$$e_b(t) = \begin{cases} |e_B(t)| & e_B(t) < 0 \\ 0 & e_B(t) \geq 0 \end{cases} \tag{3.14}$$

The MPC-based algorithm is applied periodically. At each decision step t, it determines the optimal air flow volume trajectory $[u(t), u(t+1), \cdots, u(t+w-1)]$ and battery charging/discharging trajectory $[e_B(t), e_B(t+1), \cdots, e_B(t+w-1)]$ for a predicting

window w. The optimization takes into account the electricity price forecasts and the building operation constraints such as room temperature constraints and battery storage charging/discharging restrictions. The room temperature within the predicting window is predicted based on the thermal dynamics model, the air flow volume trajectory, and the forecasted environmental disturbances. Once the optimal air flow volume and battery charging/discharging trajectories are determined, the MPC algorithm will implement the first entry $u(t)$ and $e_B(t)$ to control the HVAC system and operate the battery storage. Next, the decision step will advance to $t+1$ and the predicting window will be advanced by one decision step accordingly (in our experiments the decision step is set to one hour), and the MPC algorithm will be applied again.

Variables and parameters of the MPC formulation are listed in Table 3.1. Objective function (3.4) minimizes the total energy cost within the predicting window. The first term of (3.4) captures the energy consumption cost of the grid electricity, while the second term calculates the battery depreciation cost (based on battery manufacturing cost and battery maximum charging/discharging cycles). Battery discharging energy is denoted by $e_b(t)$ and calculated in equation (3.14), where $e_B(t) < 0$ represents battery discharging energy while $e_B(t) > 0$ denotes battery charging energy. As shown in objective function (3.4), the battery depreciation cost is calculated during the battery discharging process. Equation (3.5) follows equation (3.3) and calculates the temperature of building thermal zones, where $\hat{d}(t)$ is the environment disturbance vector that represents sun radiation intensity, ambient temperature, etc. Constraint (3.6) sets bounds for air flow input volume. Constraint (3.7) sets bounds for room temperature, which has to be satisfied for building occupants comfort.

Constraint (3.8) sets the relation among grid electricity consumption $e_g(t)$, HVAC energy consumption $e_H(t)$, and battery charging/discharging energy $e_B(t)$. The HVAC energy consumption $e_H(t)$ is calculated in equation (3.9) as a function of air flow volume, and is based on the result from [74]. Constraint (3.10) restricts battery maximum charging/discharging rate. Equation (3.11) updates battery state-of-charge in the next decision step by considering battery energy decay and round-trip efficiency. Constraint (3.12) sets the battery charging/discharging safety boundary. Constraint (3.13) is the battery end-of-day energy limit, which requires the battery to have the same initial state-of-charge condition when the next day begins.

Table 3.1: MPC algorithm variables definition

i	current decision step	w	predicting window length
τ	length of decision step	N	total number of steps
c_r	max charging rate	p_b	battery depreciation cost
d_r	max discharge rate	$\hat{d}$	environment disturbances
u	air flow volume	p_g	electricity price vector
T_c	node temperature	e_H	HVAC energy demand

e_g	building energy consumption
e_b	battery discharging energy
e_B	battery charging/discharging energy
Soc	battery state-of-charge
E_0	battery initial state-of-charge
γ	battery energy decay rate
ρ	battery round-trip efficiency
A, B, C, E	building thermal dynamics state space matrices
U^-, U^+	air flow volume lower/upper bounds
T^-, T^+	comfort zone temperature lower/upper bounds
E^-, E^+	battery charging/discharging range bounds
c_1, c_2, c_3, c_4	HVAC energy demand function coefficients

B. Demand Bid Curve Creation and Aggregation

The intelligent building energy scheduling algorithm provides the optimal energy schedule of buildings for each decision step within the predicting window, given the forecasting information of real-time prices and environment disturbances. The pair of electricity demand and price forecast reflects the amount of electricity that customers would be willing to buy at the corresponding price in current decision step. As we increase (or decrease) the electricity price forecast for current decision step while keeping price forecasts for the rest of the decision steps fixed [1], the corresponding optimal energy consumption for current decision step decreases (or increases). These pairs of electricity price and quantity forecast explicitly quantify the flexibility of buildings in current decision step. The locus of points traced out by following the price-quantity pairs when we gradually increase price forecast for current decision step, forms the building's flexible load demand bid curve [66]. An example of an individual customer flexible loads demand bid curve in a specific decision step is shown as Figure 3.2.

(1) Demand bid curve: we develop Algorithm 1 to derive the demand bid curve of an individual customer. All notations used in Algorithm 1 are declared in Table 3.2. In the following, bold notations represent vectors and plain notations represent scalars.

As shown in Algorithm 1, calculating demand bid curve at current decision step i requires a price forecast vector $\boldsymbol{p_r}$ (whose length is the same as the predicting window

[1]The real-time electricity price time series may exhibit autocorrelation, higher volatility and frequency of spikes, in which case a Markov regime switching model could be adopted to model the price series [93]. For simplicity, these stochastic factors are not modeled in this dissertation.

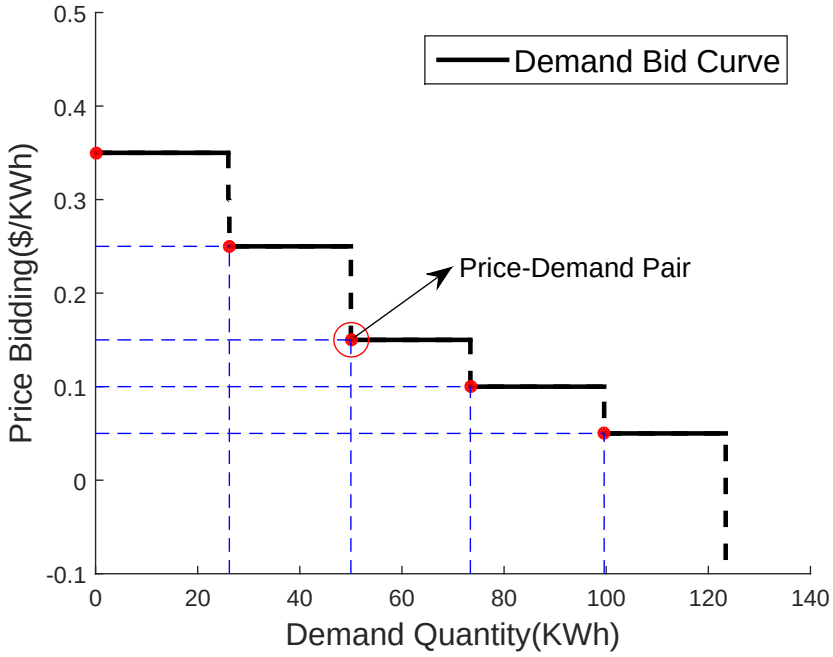

Figure 3.2: Demand bid curve

Algorithm 1 $\boldsymbol{P_j^d}$ = Demand_Curve$(i, \boldsymbol{p_r})$

Set P_{lower} and P_{upper}

$L \leftarrow (P_{upper} - P_{lower})/P_{incr} + 1$

for $l := 1$ to L **do**

    $\lambda_i \leftarrow P_{lower} + P_{incr} * (l - 1)$

    $\boldsymbol{p_r}[i] \leftarrow \lambda_i$

    $\boldsymbol{d} \leftarrow$ MPC$(i, \boldsymbol{p_r})$

    $\boldsymbol{w}[l] \leftarrow \lambda_i$

    $\boldsymbol{P_j^d}[l] \leftarrow \boldsymbol{d}[1]$

return $\boldsymbol{P_j^d}$

Table 3.2: Algorithm 1 and 2 variables definition

λ_i	possible price at decision step i	$\boldsymbol{p_r}$	electricity price vector
l	indices of bid points in demand bid curve		
L	total number of price points in demand bid curve		
P_{incr}	price increment		
$\boldsymbol{d}$	optimal energy scheduling within predicting window		
$\boldsymbol{w}$	customer willingness to pay for energy consumption $\boldsymbol{P_j^d}$		
P_{lower}	lower bound of price at decision step i		
P_{upper}	upper bound of price at decision step i		
n_j	number of buildings on bus j		
$\boldsymbol{P_j^d}$	energy consumption of individual demand bids set j		
$\boldsymbol{P_{j,k}^d}$	energy consumption of building k in demand bids set $\boldsymbol{P_j^d}$		
$\boldsymbol{P_j^D}$	energy consumption of aggregated demand bids set j		

size in MPC). P_{lower} and P_{upper} bound the possible price for current decision step i. Line 2 determines the number of distinct bid points. During each iteration, a possible price for decision step i is stored into λ_i in line 4 and $\boldsymbol{p_r}$ is updated in line 5. Then line 6 runs MPC algorithm to compute the optimal energy scheduling $\boldsymbol{d}$ within current predicting window based on the updated price forecast profile $\boldsymbol{p_r}$. Line 7 and 8 store the possible price value and the corresponding demand bid into $\boldsymbol{w}$ and $\boldsymbol{P_j^d}$, respectively. Finally those isolated price-demand pairs are connected sequentially to form the demand bid curve of current decision step i.

(2) Individual demand bid curve aggregation: the individual demand bid curves derived by Algorithm 1 need to be properly aggregated at substation level in order to solve the electricity market economic dispatch optimization problem. Without considering power losses in distribution lines, individual demand bid curves could be linearly added up to form the substation-level demand bid curve. This is shown in Algorithm 2 with notations defined in Table 3.2. Line 1 in Algorithm 2 initializes the aggregated demand bids set $\boldsymbol{P_j^D}$. In line

3, all individual demand bids set $\boldsymbol{P^d_{j,k}}$ in demand bids set j are linearly added up to derive the aggregated demand bid set on bus j.

Algorithm 2 $\boldsymbol{P^D_j}$ = Bid_Aggregate($j, \boldsymbol{P^d_j}$)

$\boldsymbol{P^D_j} \leftarrow [\mathbf{0}]_{1\times L}$

for $k := 1$ to n_j **do**

    $\boldsymbol{P^D_j} \leftarrow \boldsymbol{P^D_j} + \boldsymbol{P^d_{j,k}}$

return $\boldsymbol{P^D_j}$

C. Integrated Market Operations

(1) Network optimization formulation: the real-time market clears the supply offers with demand bids by maximizing the sum of the surplus of generation companies and retail customers. In each decision step, the wholesale market operator clears demand and supply in the network by solving a security constrained economic dispatch (SCED) problem [94][95], as shown below.

$$max\{\sum_{j\in J} u_j(\hat{P}_j^D) - \sum_{i\in I} C_i(\hat{P}_i^G)\} \tag{3.15}$$

$$\textbf{s.t:}\ \ P_k - P_{gk} + P_{dk} = 0, k = 1, ..., N_{bus} \tag{3.16}$$

$$|\sum_{k=1}^{N_{bus}} GSF_{bk} \times P_k| \leq F_{max}^b \tag{3.17}$$

$$\hat{P}_i^G \leq P_i^{max}, i \in I \tag{3.18}$$

$$\hat{P}_i^G \geq P_i^{min}, i \in I \tag{3.19}$$

$$u_j(\hat{P}_j^D) = \sum_{l=1}^{L} w_{lj}\hat{P}_{lj}^D \tag{3.20}$$

$$C_i(\hat{P}_i^G) = a_i\hat{P}_i^G + b_i(\hat{P}_i^G)^2 \tag{3.21}$$

The notations in SCED algorithm are presented in Table 3.3. The objective function (3.15) maximizes the sum of total surplus of all customers and power generation companies. Meanwhile it also minimizes the total generation cost. The first term of equation (3.15) denotes customers' utility function, while the second term denotes the sum of generation cost. Customer utility function u_j and generator cost function C_i are calculated in equation (3.20) and (3.21), respectively. Equation (3.16) is power supply/demand constraint for each bus. We use λ to denote the multiplier vector of constraints (3.16). It represents the shadow price of real power balance constraint on each bus. λ corresponds to the LMP in electricity market. Constraint (3.17) guarantees that the power flow will not exceed the thermal capacity on each transmission line. Constraints (3.18) and (3.19) bound the maximum and minimum power output of each generator.

Table 3.3: SCED algorithm variables definition

P_k	bus k power injection	J	aggregated demand bids set
P_{gk}	bus k total generation	I	set of generators
P_{dk}	bus k total demand	$\hat{P}_i^G$	generator i power generation
GSF_{bk}	generation shift factor from bus k to line b		
F_{max}^b	maximum power flow on line b		
N_{bus}	number of buses in the power network		
$\hat{P}_j^D$	dispatched energy consumption of aggregated demand bids set j		
$\hat{P}_{lj}^D$	segment l energy consumption of $\hat{P}_j^D$		
w_{lj}	customer willingness to pay for electricity demand $\hat{P}_{lj}^D$		
P_i^{min}	minimum power output of generator i		
P_i^{max}	maximum power output of generator i		

(2) Substation dispatching points disaggregation: after the wholesale market clears energy demand and supply bidding, the dispatch points need to be disaggregated into individual dispatching instructions for each building to manage its flexible loads. Algorithm 3 elaborates this procedure, with notations shown in Table 3.4.

Without considering power losses in distribution system, the disaggregation can be performed for two cases: (1) clearing price is not at the *jump point* of the aggregated demand bid curve, in which case the dispatch quantity for each customer is exactly the energy consumption at clearing price in its demand bid curve; and (2) clearing price falls on the *jump point*, in which case the disaggregated dispatch quantity consists of two parts. The first part is the same as the quantity in case (1) and those quantities will be subtracted from the total dispatch quantity $\boldsymbol{Q}[j]$. Then the remaining dispatch quantity is allocated to each customer proportionally based on their energy demand variation at current clearing price $\boldsymbol{\lambda}[j]$ in its demand bid curve (line 7).

Algorithm 3 $\boldsymbol{q}$ = Dispatch_Disaggregate$(j, \boldsymbol{\lambda}, \boldsymbol{Q})$

$\boldsymbol{q} \leftarrow [\mathbf{0}]_{1\times n_j}$

for $k := 1$ to n_j **do**

  if $\boldsymbol{\lambda}[j] \notin \boldsymbol{w_j}$ **then** ▷ *Clearing price is not at jump point*

    $\boldsymbol{q}[k] \leftarrow \mathcal{P}^d_{j,k}(\boldsymbol{\lambda}[j])$

  else ▷ *Clearing price is at jump point*

    $\boldsymbol{q}[k] \leftarrow \mathcal{P}^d_{j,k}(\boldsymbol{\lambda}[j])$

    $+\frac{\overline{P}^{d,\lambda}_{j,k} - \underline{P}^{d,\lambda}_{j,k}}{\sum_{k=1}^{n_j}(\overline{P}^{d,\lambda}_{j,k} - \underline{P}^{d,\lambda}_{j,k})} \cdot \left[\boldsymbol{Q}[j] - \sum_{k=1}^{n_j} \mathcal{P}^d_{j,k}(\boldsymbol{\lambda}[j])\right]$

return $\boldsymbol{q}$

Table 3.4: Algorithm 3 variables definition

$\boldsymbol{q}$	set of disaggregated dispatch quantities
n_j	number of buildings on bus j
$\boldsymbol{Q}$	set of total dispatch quantity on each bus
$\boldsymbol{\lambda}$	set of clearing price on each bus
$\boldsymbol{w_j}$	set of prices in jump points of demand bid curve on bus j
$\mathcal{P}^d_{j,k}$	mapping function between $\boldsymbol{P^d_{j,k}}$ and its bidding prices
$\mathcal{P}^D_j$	mapping function between $\boldsymbol{P^D_j}$ and its bidding prices
$\overline{P}^{d,\lambda}_{j,k}$	maximum energy consumption at price λ in individual demand bid curve k on bus j
$\underline{P}^{d,\lambda}_{j,k}$	minimum energy consumption at price λ in individual demand bid curve k on bus j

D. Overall Proactive Demand Participation Algorithm

Based on the methodologies and algorithms introduced in previous subsections 3.1.1 and 3.1.1, we summarize the algorithm flow for our proactive demand participation strategy, as show in Algorithm 4 with notations in Table 3.5.

Algorithm 4 $\boldsymbol{P_r} =$ Proactive_Response($\boldsymbol{P_r}$)

$\boldsymbol{P_r} = [\boldsymbol{p_{r_1}}, \boldsymbol{p_{r_2}}, ..., \boldsymbol{p_{r_{N_{bus}}}}]^T$

while $i \leq 24$ **do**

  for each $j \in J$ **do**

    for $k := 1$ to n_j **do**

      $\boldsymbol{P_j^d} \leftarrow$ Demand_Curve($i, \boldsymbol{p_{r_j}}$) ▷ *Algorithm 1*

    $\boldsymbol{P_j^D} \leftarrow$ Bid_Aggregate($j, \boldsymbol{P_j^d}$) ▷ *Algorithm 2*

  $(\boldsymbol{\lambda_i}, \boldsymbol{Q_i}) \leftarrow$ SCED($\boldsymbol{P_j^D}, \hat{\boldsymbol{D}}$)

  for each $j \in J$ **do**

    $\boldsymbol{p_{r_j}}[i] \leftarrow \boldsymbol{\lambda_i}[j]$

    $\boldsymbol{q_{i,j}} \leftarrow$ Dispatch_Disaggregate($j, \boldsymbol{\lambda_i}, \boldsymbol{Q_i}$) ▷ *Algorithm 3*

    for $k := 1$ to n_j **do**

      MPC($i, \boldsymbol{p_{r_j}}, \boldsymbol{q_{i,j}}[k]$)

  $i \leftarrow i + 1$

return $\boldsymbol{P_r}$

Table 3.5: Algorithm 4 variables definition

$\boldsymbol{P_r}$	price profile matrix	$\boldsymbol{p_{r_j}}$	price vector on bus j
$\hat{\boldsymbol{D}}$	fixed load demand	N_{bus}	number of buses
$\boldsymbol{\lambda_i}$	set of clearing price on each bus in decision step i		
$\boldsymbol{P_j^d}$	energy consumption of individual demand bids set j		
$\boldsymbol{P_j^D}$	energy consumption of aggregated demand bids set j		
$\boldsymbol{Q_i}$	set of total dispatch quantity on each bus in decision step i		
$\boldsymbol{q_{i,j}}$	dispatching quantities on bus j in decision step i		

As shown in line 5 of Algorithm 4, at current decision step i, Demand_Curve algorithm (Algorithm 1) constructs flexible demand bid curves of individual buildings by solving the MPC formulation in subsection 3.1.1. Then in line 6, individual demand bid curves are aggregated at substation level (Algorithm 2). The aggregated demand bid curve contains the information of how much electricity customers would be willing to buy at different price rates. Based on such information, in line 7, the SCED algorithm introduced in subsection 3.1.1 determines the economic dispatching points, which contain both electricity market clearing price $\boldsymbol{\lambda_i}$ and dispatch quantity $\boldsymbol{Q_i}$ in decision step i. The substation-level dispatching points are disaggregated into dispatch quantity for each individual building customer in line 10 (Algorithm 3). Finally, in line 12 each building operates its flexible load by strictly following the dispatch quantity $\boldsymbol{q_{i,j}}$.

3.1.2 Baseline Passive Demand Response

To evaluate our proactive demand response scheme, we compare it with a conventional passive demand response strategy as introduced below. In this baseline passive demand response process, the building energy management system uses the same MPC-based algorithm to schedule HVAC control and battery storage usage, based on the real-time

electricity price forecast. Then customers' current energy demand information is submitted to the electricity market operator. Next the electricity market operator is responsible for solving the SCED problem and determining the electricity price for current decision step, given customers' energy demand information.

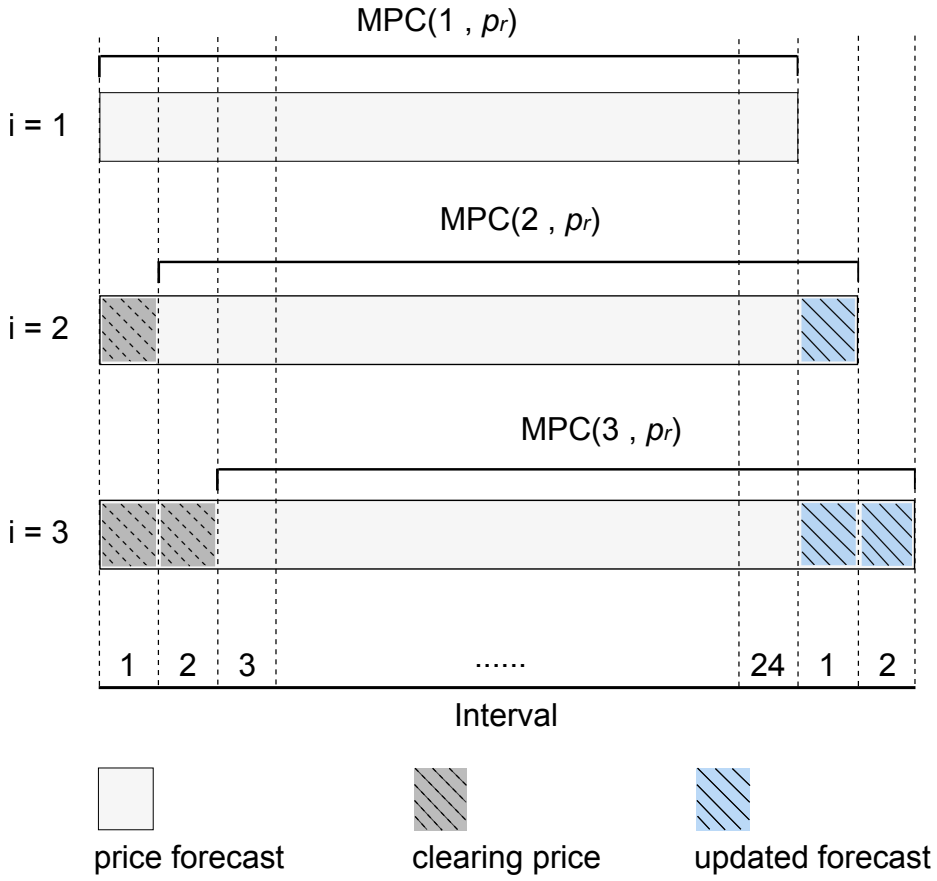

Figure 3.3: Passive demand response diagram

Figure 3.3 illustrates the process of passive demand response strategy for the first three decision steps. When scheduling energy demand for the first decision step, the MPC algorithm determines current decision step's optimal flexible load energy demand based on the initial electricity price forecasts. Then the electricity market operator sets the electricity

price and updates customers' price forecast profile for current decision step (shown by dash-line shadow). The price forecasts of the rest decision steps remain fixed. Next, the predicting window in the MPC algorithm is moved forward by one decision step and the algorithm solves the optimal energy scheduling within the new predicting window. The price forecast profile on the new predicting window is constructed by adding the updated price of last decision step at the end of the initial price forecast profile (as shown by solid-line shadow), by assuming the following day's price has a similar characteristic as the corresponding decision step at current day. We repeat the above process to obtain the passive demand response in each decision step. The passive demand response algorithm is shown in Algorithm 5.

Algorithm 5 $\boldsymbol{P_r} =$ Passive_Response($\boldsymbol{P_r}$)

$\boldsymbol{D} = [\boldsymbol{d_1}, \boldsymbol{d_2}, ..., \boldsymbol{d_{N_{bus}}}]^T$

$\boldsymbol{P_r} = [\boldsymbol{p_{r_1}}, \boldsymbol{p_{r_2}}, ..., \boldsymbol{p_{r_{N_{bus}}}}]^T$

while $i \leq 24$ **do**

  for each $j \in J$ **do**

    $\boldsymbol{d_j} \leftarrow$ MPC($i, \boldsymbol{p_{r_j}}$)

  $\boldsymbol{\lambda_i} \leftarrow$ SCED($\boldsymbol{D}, \hat{\boldsymbol{D}}$)

  for each $j \in J$ **do**

    $\boldsymbol{p_{r_j}}[i] \leftarrow \boldsymbol{\lambda_i}[j]$

  $i \leftarrow i + 1$

return $\boldsymbol{P_r}$

Table 3.6: Algorithm 5 variables definition

$\boldsymbol{P_r}$	price profile matrix	$\boldsymbol{p_{r_j}}$	price vector on bus j
$\boldsymbol{D}$	demand profile matrix	$\boldsymbol{d_j}$	demand vector on bus j
$\hat{\boldsymbol{D}}$	fixed load demand	$\boldsymbol{\lambda_i}$	clearing price in decision step i
N_{bus}	number of buses in the power network		

In Algorithm 5, $\boldsymbol{P_r}$ is the electricity price matrix that contains the initial price forecast profile on each bus. $\boldsymbol{D}$ denotes flexible load optimal energy demand matrix, and each of its row stores the optimal energy demand on corresponding bus. In line 5, the MPC algorithm determines the total energy demand d_j within predicting window for each bus based on its own price forecast profile $\boldsymbol{p_{r_j}}$ at decision step i. Line 6 solves the SCED problem to calculate the clearing price for each bus.

3.1.3 Experiments

A. Experiment Setup

The IEEE 30-bus network, as shown in Figure 3.4, is used to evaluate our proactive demand response scheme. There are six generation plants in this power network. Generator locations and their maximum generation capacities are listed in Table 3.7.

Table 3.7: Generator location and capacity

Generator	1	2	3	4	5	6
Bus Number	1	2	22	23	27	13
Max(MW)	730	570	1040	700	1600	600

The effectiveness of demand response strategies, including our proactive scheme, directly depends on the amount of flexible energy loads in the power network. To more

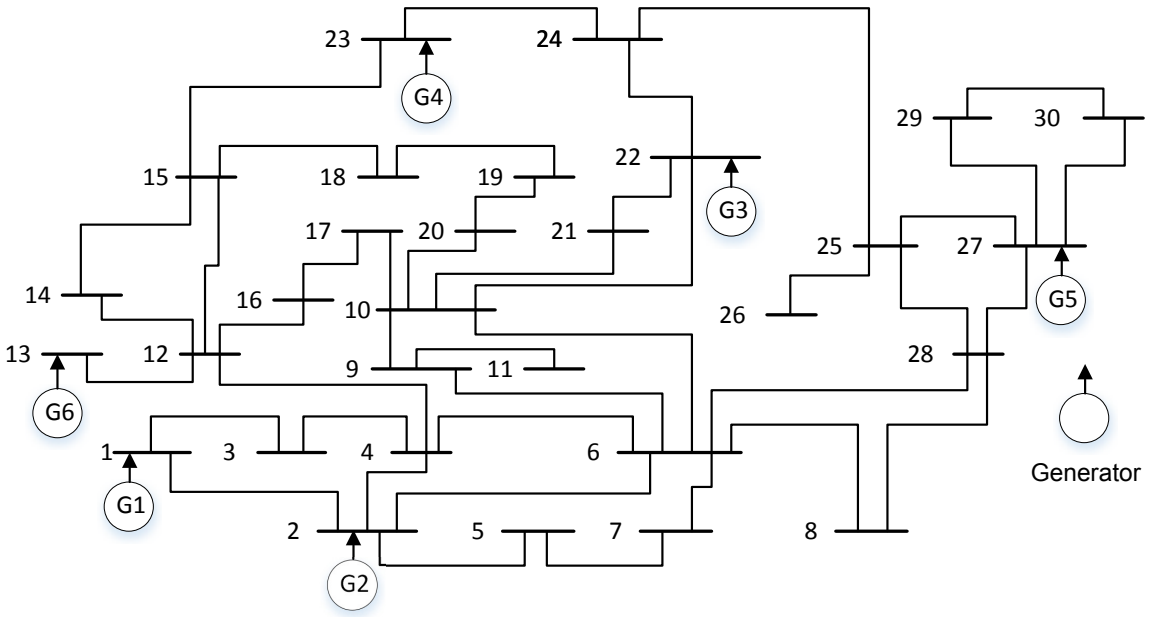

Figure 3.4: IEEE 30-bus power network diagram

comprehensively evaluate our scheme, we conduct experiments under different levels of available flexible energy loads (i.e., different amount of HVAC loads and battery storage in our case). Specifically, we define five types of buildings. Each building type has different flexible load ratio $(0\%, 25\%, 50\%, 75\% and 100\%)$ with respect to the total energy demand – the rest is fixed energy load whose demand profile is given and cannot be changed during scheduling. The flexible load ratio is defined in equation (3.23), where $D^{flexible}$ is the total energy demand from flexible load and D^{total} is the entire energy demand of a building.

$$R^{flexible} = \frac{D^{flexible}}{D^{total}} \tag{3.22}$$

In total, 1000 buildings are deployed on each bus. Each building operates an HVAC system and is equipped with a battery storage system. Moreover, each building also has certain amount of fixed load (e.g., lighting and office equipment). Each type of load

is characterized by a maximum power demand rating. The total peak demand of all types of load in each building is set to $150kW$. The building's comfort temperature zone range is set to $20\ ^{\circ}C \sim 23\ ^{\circ}C$. The battery's maximum charging/discharging rate in one hour is 25% of its maximum capacity, and the battery state-of-charge lower and upper bound is set to 20% and 80% respectively. We calibrate the number of buildings for each building type to obtain various desired flexible load ratios to a bus. In (3.23), m_i denotes the number of the i-th type of building, $R^{flexible}$ is our desired flexible load ratio for the bus.

$$\begin{aligned} &\sum_{i=1}^{5} m_i = 1000 \\ &\frac{\sum_{i=1}^{5} D_i^{flexible} \cdot m_i}{\sum_{i=1}^{5} D_i^{total} \cdot m_i} = R^{flexible} \end{aligned} \tag{3.23}$$

Furthermore, customers in electricity market are allowed to use different types of demand response strategies, which means some buildings are passive demand response users while some buildings may follow proactive demand response instructions. We define the proactive-demand-response ratio as shown in equation (3.24), where $N_{proactive}$ is the number of buildings which participate in proactive demand response scheme and N_{total} is the total number of buildings that contain flexible load in the power network (in our experiments all buildings have the same peak demand. If the buildings are heterogeneous in terms of energy demand as in reality, a more accurate capturing of proactive-demand-response ratio should be based on energy demand rather than number of buildings).

$$R_{proactive} = \frac{N_{proactive}}{N_{total}} \tag{3.24}$$

In the experiment, a reasonable initial electricity price forecast is constructed by running the passive DR algorithm once. Firstly, each individual building solves the

optimal energy demand scheduling for 24 hours based on a real-time price profile. Then the electricity market operator solves the optimal power flow in each decision step and derives the initial price forecast that fits with the simulation power network. In practice, time series and artificial intelligence models such as multiple linear regression and artificial neural network models could be used to generate electricity price forecasts.

B. Experiment Results

(1) Effectiveness of Proactive Demand Response

Effect of proactive-demand-response ratio: we first conduct experiments to study the effect of proactive demand response strategy on system cost at different customer participation levels, assuming the flexible load ratio is 100%. We gradually increase the ratio of proactive-demand-response customers from 0% to 100%, and assume the rest is passive demand response customers. In each case, proactive customers bid for their electricity demand and submit their demand bid curves to wholesale market operator. The system operator performs economic dispatch algorithm to clear the market based on both the flexible demand bids from proactive customers and the rigid demand bids from the passive customers. We calculate the system generation cost in each case, and compare it with the baseline approach where all building customers use passive demand response strategy (i.e., 0% proactive-demand-response ratio).

As shown in Figure 3.5, the system generation cost can be significantly reduced with more proactive demand response participation, and can achieve up to 10% in our experiment. This clearly demonstrates the advantages of our proactive demand response scheme over passive demand response. When the proactive-demand-response ratio gets very

high (exceeding 70% in our example), the reduction curve gets flat as the system has fully leveraged the scheduling potential from proactive customers.

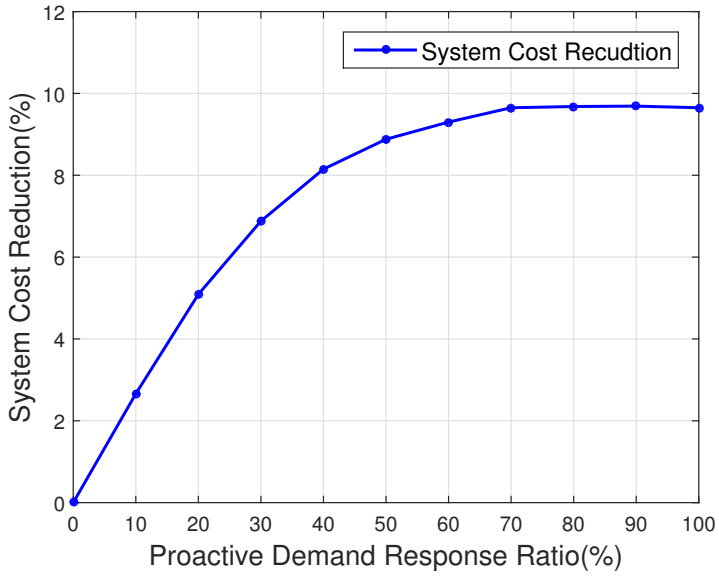

Figure 3.5: Power system generation cost reduction under various proactive demand response ratios

Effect of flexible-load ratio: we then study the effect of flexible load ratio on the power system generation cost, assuming 100% proactive-demand-response ratio. We vary the flexible load ratio from 0% to 100%. For each case, we compare the system generation cost against the baseline passive DR approach. As shown in Figure 3.6, our approach again provides significant cost reduction with respect to the baseline, and the reduction increases when the flexible load ratio increases.

Joint effect of proactive-demand-response ratio and flexible-load ratio: we also conduct experiments to evaluate our proactive demand response scheme under various flex-

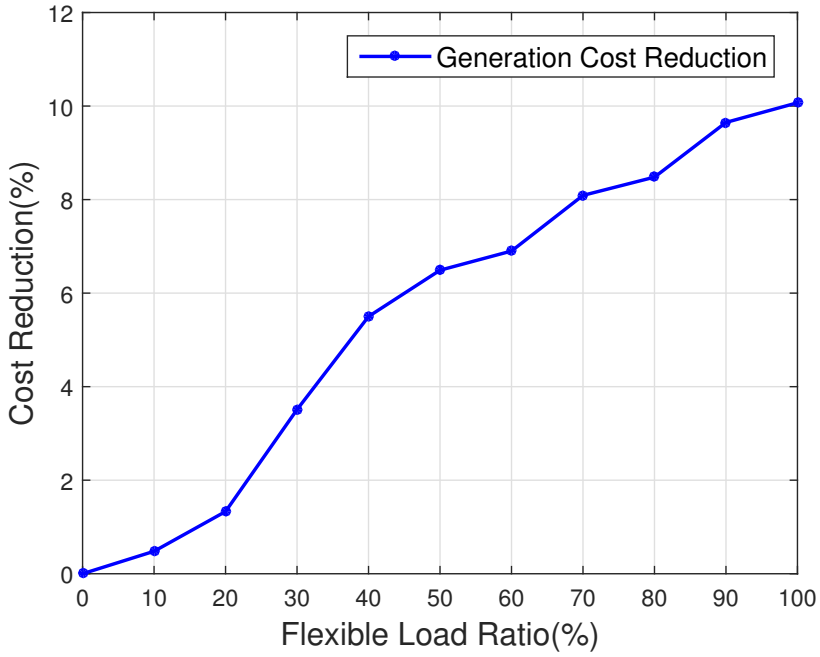

Figure 3.6: Power system generation cost reduction under various flexible load ratios

ible load installment percentage and various proactive customers participation level (essentially a more comprehensive study that includes the previous two aspects). We jointly change the proactive-demand-response ratio and flexible-load ratio, and compare power system generation cost reduction at each setting point versus the baseline case. The results are shown in Figure 3.7. The reduction of system generation cost increases when proactive-demand-response ratio increases and/or flexible-load ratio increases.

Electricity market pricing: in proactive demand response process, because of the joint optimization of electricity market dispatch and building energy management, the electricity wholesale market operator can fully leverage the advantage of building's flexibility. The market operator can determine the electricity quantity dispatched to each individual cus-

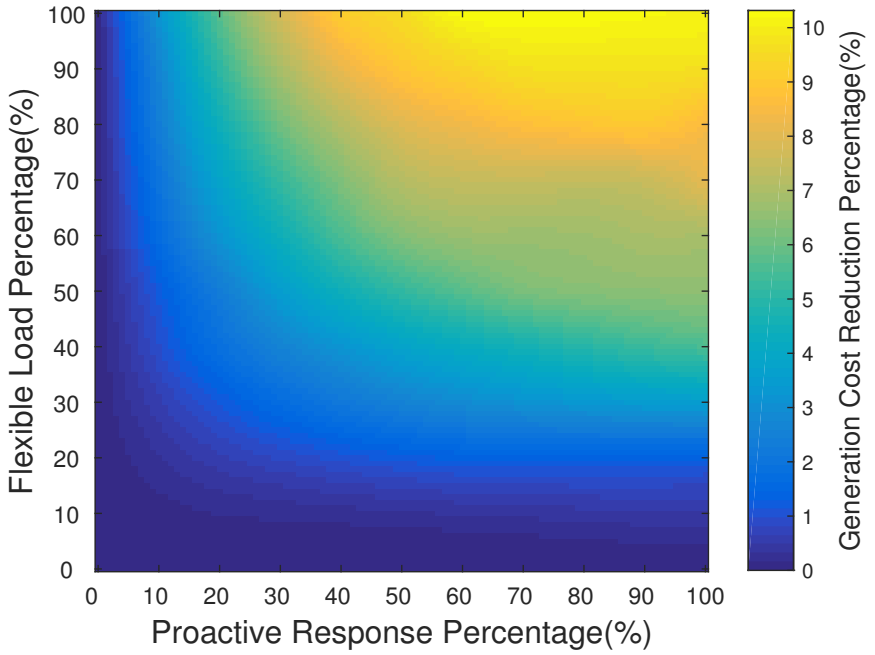

Figure 3.7: System generation cost reduction with various flexible load ratios and proactive demand response ratios

tomer, instead of just trying to meet customers' energy demand and simply using real-time prices to guide buildings' energy consumption. On the other hand, the decision of buildings' final electricity demand takes power system's generation capacity and operating conditions into consideration by providing market operator more flexibility in demand bid curve and letting market operator decide their electricity consumption. Thus the energy demand on different buses can be appropriately coordinated to avoid the synchronization of customers' peak energy demand. Consequently the proactive demand response scheme can effectively avoid utilizing high-cost generators to supply high power demand.

In Figure 3.8, under 50% of flexible load installment level, the electricity market price profiles in both passive DR process and proactive DR process are presented together.

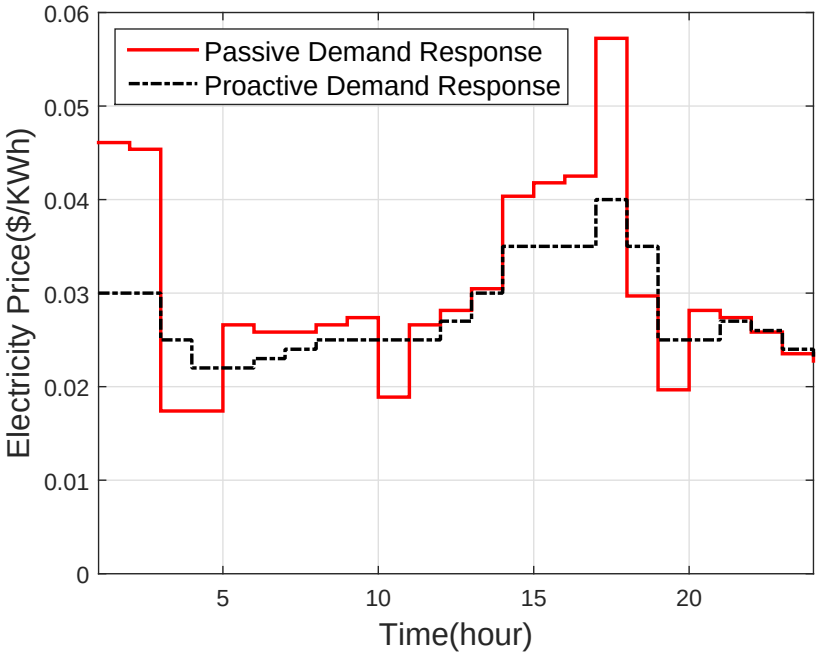

Figure 3.8: Clearing price

We can see that the price profile in proactive DR is much smoother than that in passive DR. This demonstrates that the proactive demand response scheme can help mitigate volatility in electricity market pricing.

(2) Comparison with Iterative RTP Scheme

In this work, we implemented an iterative passive RTP scheme and compared it with our proactive scheme. In the baseline passive demand response strategy introduced in section 3.1.2, we only update the price forecast at each decision step once. In this iterative RTP scheme, there are multiple iterations between the building-side energy scheduling and market clearing in transmission network, following the methodologies from [9]. Specifically, when determining the electricity price for customers at each decision step, building customers first decide their electricity demands based on the current price forecasts (by

solving the MPC-based formulation), and the market operator determines a clearing price in the electricity market after receiving the demands from all buildings. Then the building customers will repeat the energy scheduling based on the new price, and the market operator will determine a new price based on the new demands. This process will continue for multiple iterations. In this way, the building-side electricity demand scheduling and the market-side price settling might evolve toward an optimal solution. We conducted experiments to compare the system generation cost of our proactive scheme with the cost of the iterative RTP scheme, under two different levels of flexible load ratios. The results are shown in Figure 3.9. From the results we can see that with more iterations, the power system generation cost of iterative RTP scheme may decrease and get close to our proactive scheme, however still higher and oscillating. Such iterative method could be too slow for real-time operations due to high number of iterations.

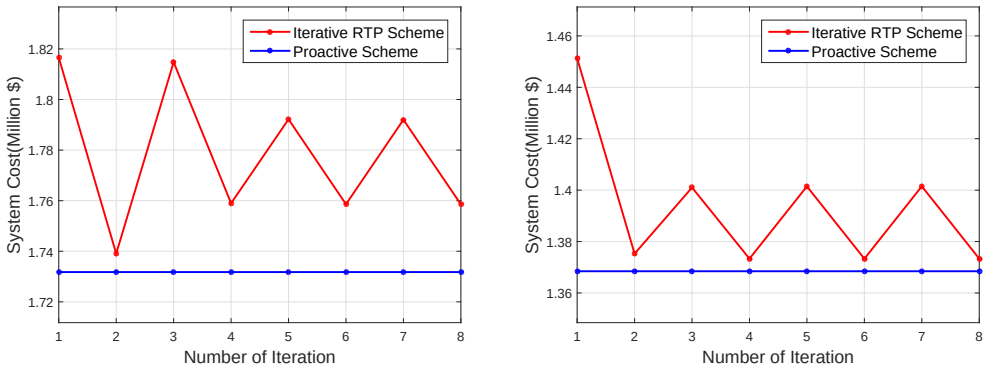

(a) 50% Flexible Load Ratio (b) 100% Flexible Load Ratio

Figure 3.9: System generation cost comparison between proactive demand response and iterative RTP scheme at different flexible load ratios: (a) 50% flexible load ratio, (b) 100% flexible load ratio

(3) Building Customer Incentives from Cost Savings

In this section, we study the effect of our proactive demand response scheme on building operating cost and evaluate how this might incentivize building customers to participate in the scheme. In passive demand response process, buildings simply schedule their energy demand base on the real-time price forecast at each decision step. Because energy management system in buildings simply manage the electricity consumption in the best interest of their own, a large number of buildings can lead to a very high electricity demand in power grid, which may lead to very high electricity charge rate for customers in return. While in our proactive demand response process, the electricity market operator is trying to maximize all customers' utility and simultaneously minimize the power system generation cost. It will typically make a compromising decision between the two and lead to a relatively low price rate.

Figure 3.10 shows the total building operating cost reduction by using proactive DR under different flexible-load ratio levels, compared with the baseline passive DR approach. It demonstrates that building customers may achieve significant operating cost reduction when they leverage their flexible loads and participate in the proactive DR process (in comparison with the passive approach). In many commercial and residential buildings, flexible loads such as HVAC systems account for 50% or more of buildings' total energy demand [1], and the flexibility could be even higher when leveraging battery storage. This shows significant incentives for building customers to participate in the proactive DR scheme.

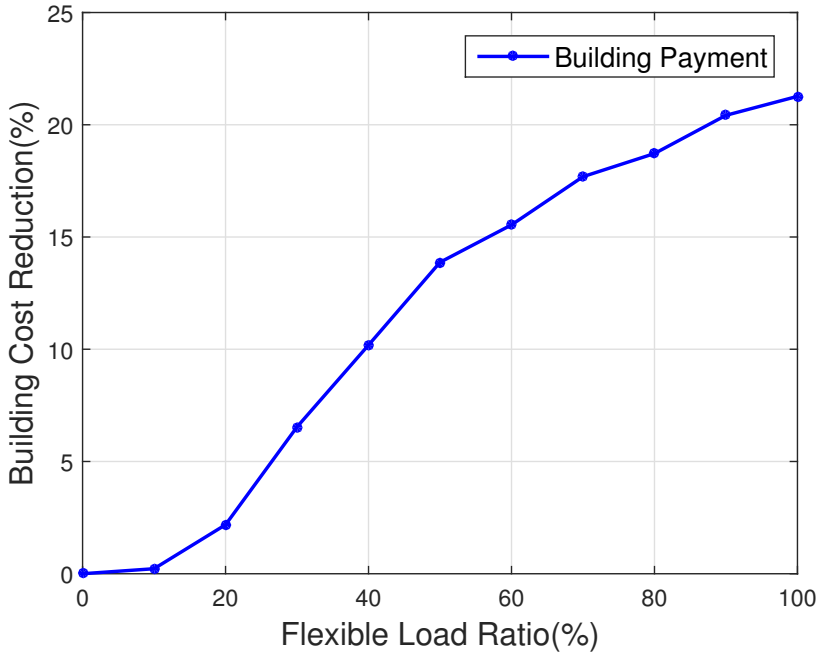

Figure 3.10: Building operating cost

(4) Trade-off between Building Comfort Level and Cost

Building operating costs and the overall power system generation cost may be significantly impacted by the required building comfort levels. In this work, we study the trade-off between these two aspects. We assume 50% of flexible-load installment level, and gradually relax building's comfort zone boundary by increasing comfort zone temperature range from $2°C$ to $13°C$ (centered around $21.5°C$). This means the building's HVAC system will have more flexibility when regulating the temperature. Then we calculate power system generation cost and total building operating cost for passive and proactive demand response under different comfort zone scenarios.

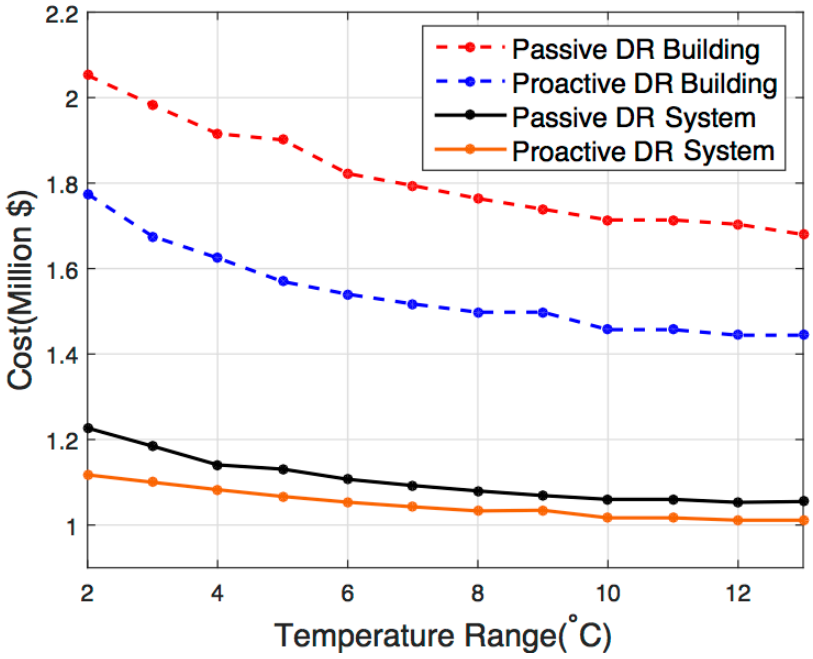

Figure 3.11: Trade-off between building comfort zone temperature range and cost (including both total building operating cost and system generation cost)

As shown in Figure 3.11, for both passive and proactive demand response strategies, building operating cost and power system generation cost decrease when comfort zone temperature range increases. The results demonstrate that relaxing building's comfort zone requirement can help reduce building customers' operating cost and power system generation cost. We can also see that both of the building operating cost and power generation cost in the passive DR strategy are higher than that from our proactive demand participation scheme, which further demonstrates the effectiveness of our proactive DR framework. Furthermore, this quantitative trend could help building operators to make trade off between comfort level and energy cost based on occupant activities, operating budget and other factors.

3.2 Security Analysis of Proactive Participation of Smart Buildings

In section 3.1, we propose an innovative proactive demand response (DR) scheme which enables the building customers to actively express their energy scheduling flexibility by defining the operations for three key decision-making components, i.e., Wholesale Market Operator, Distribution System Operator/Customer Aggregator and Intelligent Building Energy Scheduling Agent. In the proactive demand participation scheme, the bilateral information exchange among decision-making entities enable the power generation companies and building customers to benefit from the significant cost reduction. However the proactive DR scheme may also sustain the threats of malicious cyber attacks, such as guideline price manipulation, untruthful demand bids, etc. In this work, we will first present the possible attack strategies against both conventional passive DR strategy and our proactive demand participation scheme. Then, we conduct experiments to demonstrate the robustness our proactive DR scheme against various malicious cyber attacks.

3.2.1 Potential Cyber Attacks in Electricity Market

Various types of DR strategies could be vulnerable to three major cyber attacks as follows due to the bidirectional communication via wide-area network.

- Private information leakage: Customers' electricity usage preferences are transmitted via wide-area network. Private information (e.g., the pattern of residents' daily routine and customers' personal information) may be extracted from those data if attackers are able to access the metering devices [58, 59].

- Untruthful demand bidding: In proactive demand participation scheme, building customers need to submit electricity demand bids. It is possible for malicious customers to hack metering devices, create and submit fake demand bidding information to mislead the electricity market operator's decision for their own benefits [60].
- Guideline price manipulation: Proactive demand participation customers need to rely on the electricity price forecasts sent from distribution system operator to create their electricity demand bids and optimally schedule the energy consumption of different types of flexible loads inside building. Some malicious customers could hack the communication system and manipulate the electricity guideline price of other customers in the electricity market. In this way, they could possibly mislead other customers' electricity usage preferences and consequently achieve some economic benefits for themselves. In [55], similar electricity guideline price manipulation attacks against the conventional passive DR scheme has been addressed.

In DR process, building customers mainly rely on the electricity price forecasts to schedule the demand of their flexible energy loads. While the real-time clearing price on each bus of the power network is mainly affected by total electricity demand of all customers in the electricity market. Among the aforementioned security concerns, guideline price manipulation and untruthful demand bidding could have direct impact on customers' electricity usage behavior. Thus, some malicious customers could intentionally create a time period with low electricity price by misleading other customers to use less electricity by manipulating the guideline price forecast or submitting an untruthful demand bid curve. In this way, the attacker can obtain certain benefits in electricity consumption cost reduction

by scheduling its heavy electricity demand in those low-price periods. Figure 3.12 shows the overview of security analysis for our proactive DR scheme.

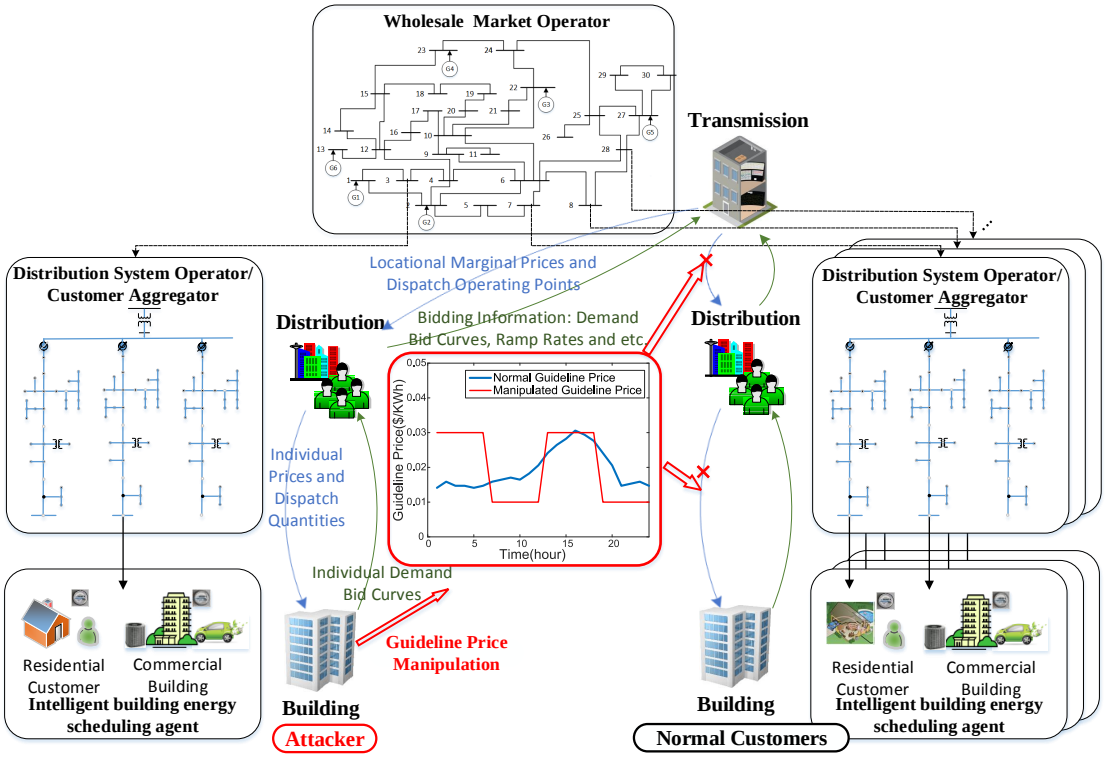

Figure 3.12: Security analysis in proactive demand participation

In this dissertation, we will present the possible guideline price manipulation attacks against both proactive demand participation and passive DR strategy, and then we evaluate the robustness of our proactive DR scheme against the guideline price manipulation and untruthful demand bidding attacks based on case studies.

A. Attacks Against Passive Demand Response Strategy

(1) Attack motivations: before introducing the attack strategies against the proactive demand participation scheme, we first talk about the possible attack strategies in passive DR. During passive DR process, utility companies will provide customers with a guideline price profile, which is used as a guidance for customers to schedule their daily electricity demand. The guideline price profile is meticulously designed by the utility company based on the predicted electricity demand of all customers. The guideline price is not used to charge customers' electricity consumption [55]. The guideline price profile predicts the future electricity price to guide customers' electricity demand. Consequently a more balanced power consumption pattern can be achieved throughout the day by encouraging customers to move some flexible electricity usage during peak hours to off-peak hours. Based on the electricity consumption of all customers in the past decision step, the electricity market will determine the real-time price to charge the electricity usage of each customer.

Based on this DR mechanism, some malicious customers can alter the guideline price in the electricity market to mislead other customers' scheduling behavior. In this way, they can force other customers to change their electricity demand and avoid overlapping the attackers' own heavy electricity demand with the total peak demand in the electricity market. In this work, we assume that building customers have certain energy storage ability apart from flexible energy loads (In this work, HVAC is the major flexible load). To reduce the electricity consumption cost, the attacker can manipulate the guideline price of other customers in the way as shown in Figure 3.13. In Figure 3.13, the blue dash line shows the attacker's daily energy consumption. Because the attacker has higher electricity demand

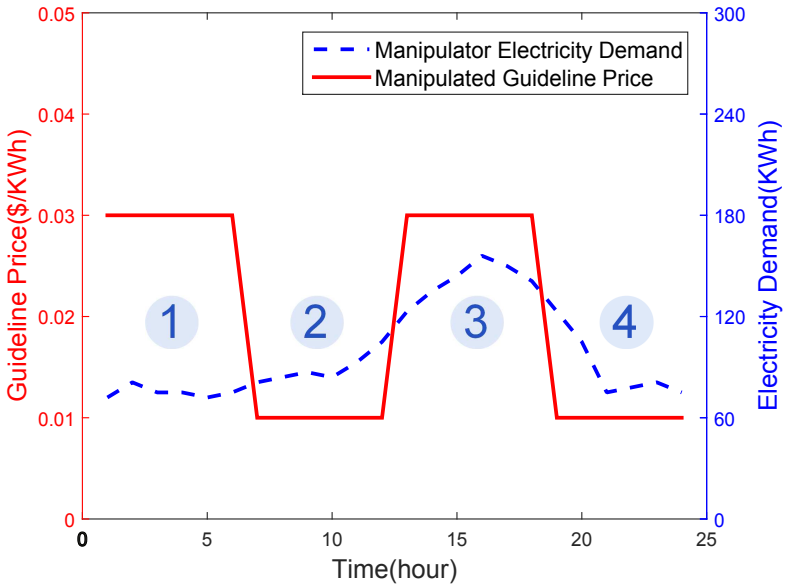

Figure 3.13: Attack strategy against passive demand response

during day time, he/she wishes to reduce the electricity price during that period of time. The attacker can create a fake guideline price curve shown by the red solid line and schedule its own electricity demand as follows:

- During period 1, the attacker charge its storage battery. While other customers would choose to use less electricity because the guideline price they receive is very high.
- During period 2, other customers will charge their storage battery which may lead to a high real-time price. So the attacker discharge battery to reduce its energy demand.
- During period 3, other customers detects the high electricity price and will try to reduce their electricity demand by discharging their battery. At this time, the attacker can schedule its heavy load to this period of time and benefits from the low price rate.
- During period 4, all customers have low electricity demand during this period of time.

(2) Attack algorithm: the price manipulation strategy against the passive DR is shown in Algorithm 6. $\boldsymbol{P_r^n}$ represents the normal electricity guideline price and the manipulated guideline price is denoted by $\boldsymbol{P_r^m}$. In line 1, the attacker will first determine its heavy energy demand starting/ending time which are represented by T_{start}^{peak} and T_{end}^{peak} respectively, and its storage battery charging ending time T_{end}^{charge}. Then line 2 to line 5 use the maximum and minimum price rate in the normal guideline price to set the price rate in different periods of the manipulated guideline price as discussed in section 3.2.1.

Algorithm 6 $\boldsymbol{P_r^m}$ = Passive_Attack($\boldsymbol{P_r^n}$)

1: Set T_{start}^{peak}, T_{end}^{peak} and T_{end}^{charge}

2: $\boldsymbol{P_r^m}[1 : T_{end}^{charge}] \leftarrow max(\boldsymbol{P_r^n})$

3: $\boldsymbol{P_r^m}[T_{end}^{charge} : T_{start}^{peak}] \leftarrow min(\boldsymbol{P_r^n})$

4: $\boldsymbol{P_r^m}[T_{start}^{peak} : T_{end}^{peak}] \leftarrow max(\boldsymbol{P_r^n})$

5: $\boldsymbol{P_r^m}[T_{end}^{peak} : T_{end}] \leftarrow min(\boldsymbol{P_r^n})$

6: **return** $\boldsymbol{P_r^m}$

B. Attacks Against Proactive Demand Participation Scheme

(1) Attack motivations: for proactive demand participation scheme, similar price-manipulation attacks can be conducted by attackers to reduce their own electricity consumption cost. Unlike the passive demand response scheme, the attacker cannot directly increase or decrease other customers' electricity usage during specific decision steps by decreasing or increasing the electricity price in the corresponding decision step. That's because as introduced in section 3.1, proactive demand participation customers don't directly submit their electricity

demand for each decision step. Actually they will receive an electricity price forecast for the next 24 hours starting from the current decision step, and create a demand bid curve based on the information of future electricity price in the market and their energy demand to operate various energy loads.

For current decision step, if the intelligent building energy scheduling agent detects very high electricity price rates in the following time intervals, the electricity usage preferences in the demand bid curve would be relatively higher for current time interval. That's because when the future electricity price is higher, the customers would be likely to accept more electricity consumption at high electricity price rate. Otherwise, if the electricity price rates in future intervals are very low, the intelligent building energy scheduling agent would choose to construct a demand bid curve with low electricity usage for current decision step. That's because when the future prices are lower, customers would choose to use more electricity later and reduce the their energy demand in current interval.

Based on these features in our proactive demand participation scheme, the attacker can manipulate other customers' electricity usage pattern in the following way as shown in Figure 3.14.

- As shown in Figure 3.14a, at current time, the attacker has low electricity demand (i.e., blue dash line). The attacker will send the fake guideline price (i.e., red solid line) to other customers in the electricity market. As discussed above, other customers would have high electricity usage preference in their demand bid curves (shown in left figure). In this way, the electricity market will dispatch a large quantity to normal customers and normal customers can charge their storage battery with enough dispatch quantity. Consequently,

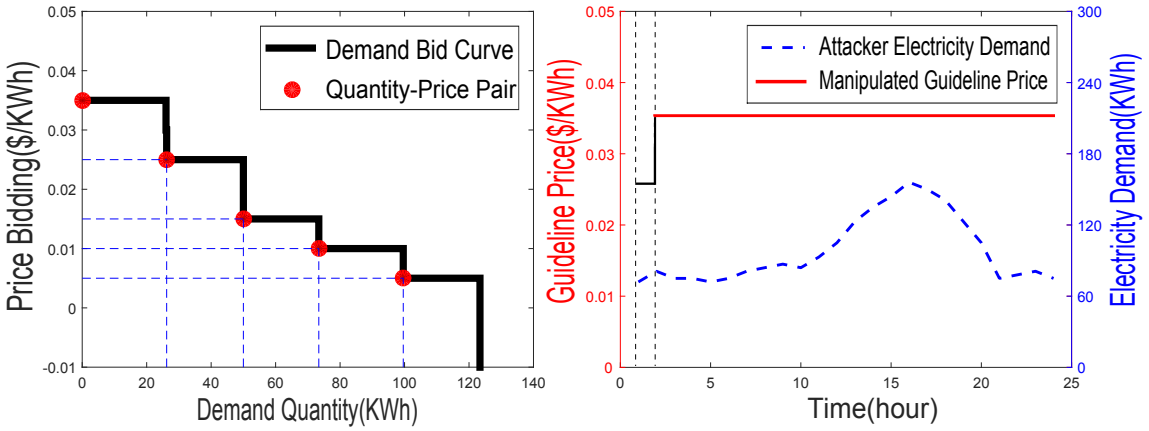

(a) Attack Strategy in High-demand Interval

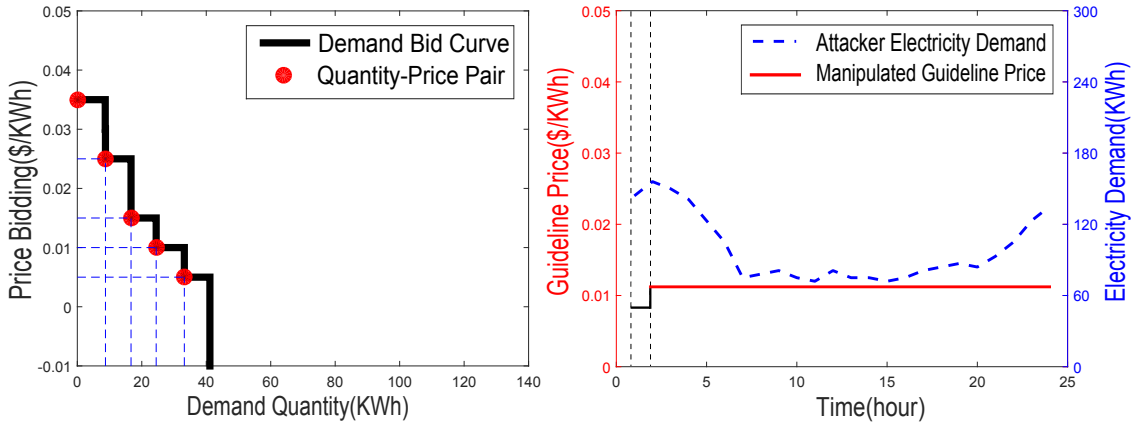

(b) Attack Strategy in Low-demand Interval

Figure 3.14: Attack strategy against proactive demand participation

this would result in higher clearing price. But the attacker has low electricity demand at current time, so it will not significantly increase the attacker's electricity bill.

- In Figure 3.14b, when the attack has high electricity demand in current time interval, the attacker will deceive other customers by sending them a low guideline price profile (as shown in red solid line). In this case, other customers would discharge their battery to reduce their electricity demand and create a demand bid curve with low electricity demand

preferences, which will lead to a very low clearing price in the electricity market. Thus in current time interval, the attacker could benefit from more electricity consumption.

(2) Attack algorithm: next we present the price manipulation strategy against the proactive demand participation in Algorithm 7.

Algorithm 7 $\boldsymbol{P_r^m}$ = Proactive_Attack($\boldsymbol{P_r^n}, T_{current}$)

1: Set T_{start}^{peak} and T_{end}^{peak}

2: **if** $T_{current} < T_{start}^{peak}$ **then**

3: $\quad \boldsymbol{P_r^m}[2 : T_{num}] \leftarrow max(\boldsymbol{P_r^n})$

4: **if** $T_{start}^{peak} < T_{current} < T_{end}^{peak}$ **then**

5: $\quad \boldsymbol{P_r^m}[2 : T_{num}] \leftarrow min(\boldsymbol{P_r^n})$

6: **if** $T_{end}^{peak} < T_{current}$ **then**

7: $\quad \boldsymbol{P_r^m}[2 : T_{num}] \leftarrow max(\boldsymbol{P_r^n})$

8: **return** $\boldsymbol{P_r^m}$

In Algorithm 7, the attacker first determine the starting time T_{start}^{peak} and ending time T_{end}^{peak} of its electricity demand preference as shown in line 1. From line 2 to line 7, T_{num} denotes the total number of decision step in one day. The attacker will send low guideline price profile to other customers when the attacker has high electricity demand as shown in line 4. While when the attacker has low electricity demand as shown in line 2 and line 6, the attacker will mislead other customers' decision by sending a high guideline price profile to them.

3.2.2 Experiments

A. Experiment Setup

Experiments are conducted on IEEE 30 bus system as shown in Figure 3.15. We assume there are 1000 buildings on each bus in the network. Each building operates a HVAC system to maintain the inside temperature within the preferred comfort level. Moreover, each building is also equipped with a battery storage system to store electricity energy and as an energy buffer to regulate building's total electricity demand throughout one day. The peak power demand of HVAC system in each building is set to 100 kW and battery storage system has a maximum charging/discharging rate of 50 kW. Besides, there is also certain amount of fixed load in the power network, for which the electricity demand is represented by a historical electricity consumption profile. In our experiment, buildings' flexible loads demand accounts for 50% of the total electricity demand in the whole power network (details about calibrating the flexible loads demand level can be found in [66]).

In the experiment, we assume the attacker is from bus 16 in Figure 3.15. The attacker will hack the advanced metering infrastructure to block the normal guideline price signal and send the manipulated guideline price to all customers on other buses (except for bus 16) in the network. The experiment is conducted for one typical day, the simulation duration is divided into 24 time intervals and each time interval is set to one hour.

B. Experiment Results

(1) Impact of price manipulation in proactive demand participation: in the 30-bus power network system, we firstly conduct experiments to evaluate the impact of guideline

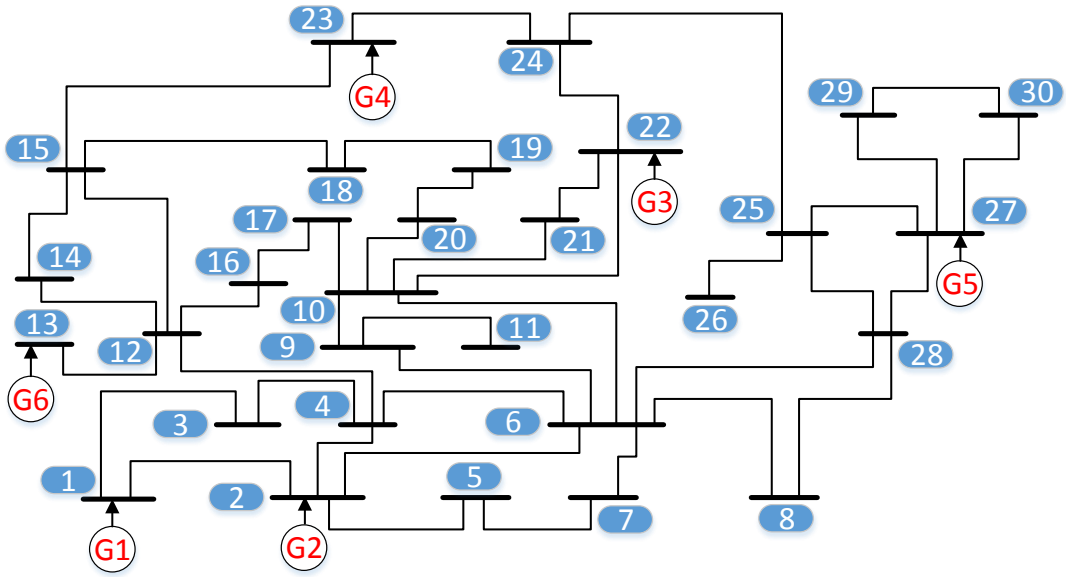

Figure 3.15: IEEE 30-bus network

price manipulation in proactive demand participation scheme. By following the guideline price manipulation strategy presented in section 3.2.1, the attacker on bus 16 misleads all customers on other buses by sending them a fake guideline price profile in each time interval. But the attacker itself will submit normal demand bid curve to the electricity market operator based on its real electricity demand. In this way, the attacker can keep other customers' high electricity demand from coinciding with its own heavy load demand.

Figure 3.16 shows the results of clearing price and customers' electricity demand when the guideline price manipulation attack is conducted by the attacker on bus 16. In Figure 3.16, the red dash line represents the normalized clearing price in the attack scenario based on the normal clearing price without attack. The blue curve represents the attacker's

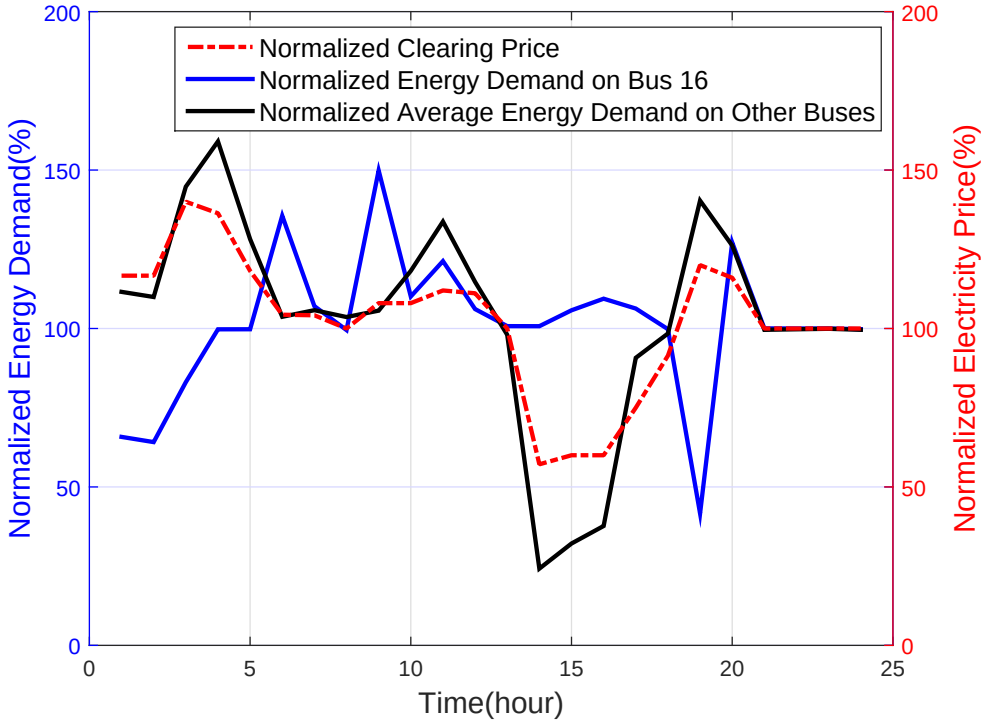

Figure 3.16: Normalized energy consumption and clearing price under price manipulation attack in proactive demand participation scheme

electricity demand and the black curve shows the average electricity demand of all normal customers on other buses (except for bus 16). They are also normalized based on the average electricity demand in normal proactive demand response scenario without attack.

In Figure 3.16, we can see that the trend of clearing price is mainly affected by majority of normal customers' electricity consumption. That's because compared with total electricity consumption of all normal customers in the electricity market, the electricity usage on bus 16 doesn't have as huge impact as those normal customers on the final clearing price. This characteristic is the key that the attacker can achieve economic benefits by manipulating the guideline price. We can see that the attacker creates a low price period

when it has high electricity demand and always avoid high electricity consumption in the same time intervals with other normal customers. Finally the experiment results show that by performing the guideline price manipulation, the attacker can achieve a 3.8% electricity cost reduction in one day as other normal customers' electricity cost is increased by 2.1%.

(2) Impact of price manipulation in passive demand response: we study the impact of guideline price manipulation on customers' electricity consumption cost in passive demand response scheme. In this case, the attacker on bus 16 manipulates the guideline price of normal customers by performing the attack strategy introduced in section 3.2.1. The attacker could speculate other customers' electricity demand in each time interval based on the fake guideline price sent to other normal customers. The attacker itself could schedule its heavy electricity demand accordingly in the intervals when the electricity price is low.

In Figure 3.17, similar as the result in section 3.2.2, the red dash line represents the normalized clearing price in the attack scenario. The blue curve and black curve represents the normalized electricity demand from the attacker and normal customers respectively. As shown in Figure 3.17, the trend of final clearing price is also dominated by the normal customers' electricity consumption. The attacker avoids consuming large amount of electricity together with the majority of customers in the electricity market. By manipulating the guideline price of other normal customers, the attacker forces the normal customers to shift their heavy electricity demand away from the attacker's peak electricity demand period. The experiment results show that in the passive demand response scheme the attacker can achieve an up to 17.2% daily electricity consumption cost reduction by performing guideline price manipulation. While other normal customers' electricity bill is increased by 6.4%.

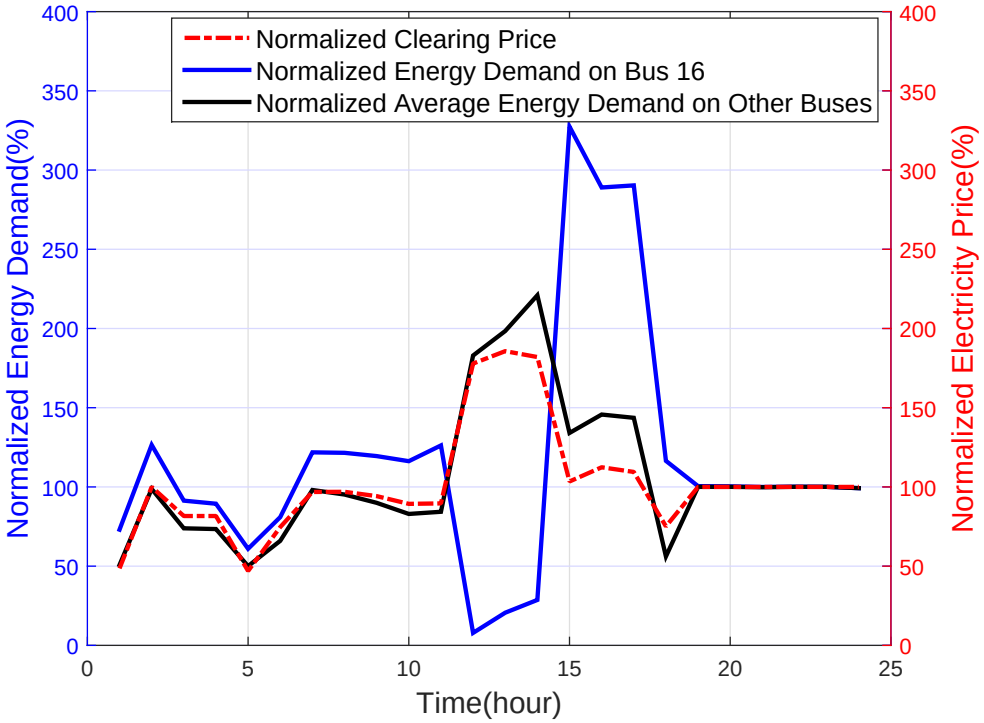

Figure 3.17: Normalized energy consumption and clearing price under price manipulation attack in passive demand response scheme

(3) Comparison of impacts of cyber attacks on two different demand response strategies: from the above experiment results, we can see that the cost reduction achieved by conducting attacks against the proactive demand participation scheme is more temperate (3.8% in proactive case and 17.2% in passive case) than that in attacks against the passive demand response scheme. That's because in passive demand response scheme, the guideline price is a direct stimulus that encourages customers to schedule flexible electricity demand in pursuit of reducing their electricity bill. So manipulating the guideline price could greatly change customers' electricity demand preference, which results in significant variations in clearing price and electricity consumption cost. While for customers in proactive demand

participation scheme, the guideline price is just used as a reference for customers to create their demand bid curve. After the electricity market operator receives demand bid information from all substations, a market clearing process, aiming at minimizing total generation cost, will be performed to determine the dispatch quantities to all customers. Even if customers in the electricity market submit demand bid curves containing very high electricity demands, the market clearing process can also effectively alleviate concurrent peak power demand by selecting a set of more temperate dispatch points to balance the electricity demand among geographically distributed customers. That explains why the proactive demand participation scheme is more robust against guideline price manipulation attacks compared with passive demand response scheme.

(4) Impact of untruthful demand bidding on proactive demand participation: malicious customers may also submit untruthful demand bid curves to gain benefits for themselves. In this work, we conduct experiments to evaluate the impact of such manipulation of demand bid curves.

We consider the cases where a malicious customer (or multiple colluding customers) has gained control of 50% of the buildings in the network. For simplicity, in this experiment we assume buildings all have the same characteristics (e.g., same flexible load ratio of 50%, same battery storage capacity, etc.), and therefore the malicious customer has control of 50% of the energy demand in the network. In practice it is highly unlikely that such high percentage of demand is under control of malicious customer(s). Nevertheless, we consider it here in our study to investigate how much impact the manipulation of demand bid curves may have in extreme cases.

Figure 3.18 shows two manipulated untruthful demand bid curves – in one the bidding price is lowered by 50% and in the other the bidding price is raised by 100% (i.e., 2X). There are many other ways to manipulate the true demand bid curve. We study these two as examples in this work.

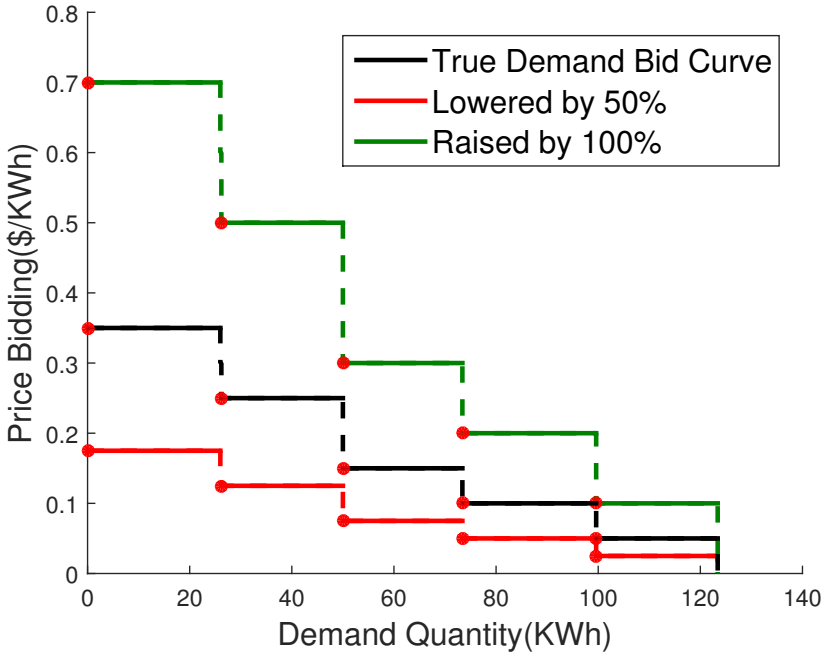

Figure 3.18: Manipulated untruthful demand bid curves

Then, first we consider several cases in which the malicious customer lowers the demand bid curves of *part of the buildings* it controls by 50% at the beginning of peak-load hours (1 : 00 pm) for an hour. Intuitively, the malicious customer tries to drive the clearing price lower to benefit *the rest of the buildings* it controls. Note that for the part of the buildings that submit untruthful lower demand bid curves at 1 : 00 pm, they will get lower amount of grid electricity dispatched to them at that hour. Therefore their demand for

grid electricity might be higher later on, and their total operating cost might not be lower. However, the malicious customer hopes to achieve an overall reduction of its cost from all of the buildings it controls. Figure 3.19 shows the clearing price in different cases, where the malicious customer manipulates 10%, 20%, 30%, 40% and 50% of all the buildings in the market. In the last case the malicious customer basically lowers the demand bid curves of all its controlled buildings at 1pm (note that we assume the malicious customer controls 50% of the buildings in the market).

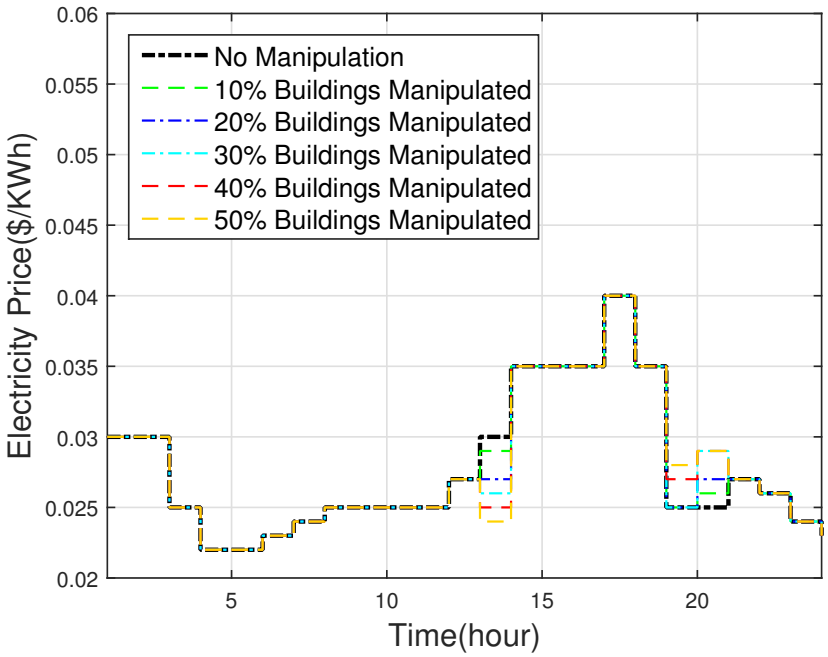

Figure 3.19: Clearing price under manipulated demand bids (lowered by 50%) in different cases

From Figure 3.19, we can see that the more buildings that submit manipulated (lower) demand bids, the lower the clearing price at 1 : 00 pm is. During the peak hours from

1 : 00 pm to 7 : 00 pm, the clearing price does not change significantly as battery is used to reduce the demand for grid electricity. After 7 : 00 pm, there is an increase in the clearing price. This confirms our analysis above – the manipulated buildings have to request more energy later to satisfy temperature comfort requirements and battery charging/discharging constraints.

Table 3.8 shows the total operating cost for the malicious customer and the total cost for the rest of the customers (i.e., the other 50% of the buildings in the network), under the five different cases as explained above. We can see that when the malicious customer manipulates a minority part of its buildings (i.e., 10% and 20% of the total buildings, out of 50% it controls), it gains a very small reduction in its cost; while other customers also see a small reduction. When the malicious customer manipulates more of its buildings, its overall cost starts increasing since the manipulated buildings actually have a higher cost over the whole process.

Table 3.8: Total costs for malicious customer and for other customers under manipulated demand bid curves

	Malicious Customer		Other Customers	
	Cost ($)	Change	Cost ($)	Change
No manipulation	841930	-	841950	-
10% buildings manipulated	841540	$\downarrow$ 0.05%	841630	$\downarrow$ 0.04%
20% buildings manipulated	840410	$\downarrow$ 0.18%	839900	$\downarrow$ 0.24%
30% buildings manipulated	842140	$\uparrow$ 0.03%	840950	$\downarrow$ 0.12%
40% buildings manipulated	844160	$\uparrow$ 0.27%	841400	$\downarrow$ 0.07%
50% buildings manipulated	845361	$\uparrow$ 0.41%	840721	$\downarrow$ 0.15%

We also conducted similar experiments where the malicious customer raises the demand bid curves by 100% at 1 : 00 pm for various percentage of the buildings it controls

(from 10% to 50% of all buildings in the market). The change of total operating cost is very small – within 0.05% for all cases. We also tried lowering and raising the true demand bid curves for more than one hour during the peak hours (e.g., for the entire peak hours of 1 : 00 pm to 7 : 00 pm), and the changes are all relatively minor – within 0.5%. Overall, the manipulations do not lead to a significant cost variation in our experiments. This demonstrates the robustness of our scheme with respect to the manipulation of demand bid curves.

Chapter 4

Deep Reinforcement Learning for Building Energy Management

In this chapter, we leverage the state-of-the-art deep reinforcement learning (DRL) to boost the energy efficiency in smart buildings. In section 4.1, we develop data-driven control algorithms for building HVAC control by modeling the key components of Markov Decision Process (MDP) in buildings [69, 70]. We demonstrate the effectiveness of our DRL-based HVAC control algorithm in reducing building energy cost while maintaining the room temperature within comfort range, and greatly reducing the design complexity of building energy management systems.

4.1 Deep Reinforcement Learning for Building HVAC Control

The recently proposed deep reinforcement learning (DRL) technique, which has been shown successful in playing Atari and Go games [61, 62], emerges as a powerful data-driven method for solving complex control problems. The DRL technique can handle large state space by building a deep neural network to relate the value estimates and associated state-action pairs, thereby overcoming the shortcoming of conventional RL. In this work, we develop an efficient DRL-based algorithm for HVAC control by 1) formulating the HVAC operation as a Markov Decision Process (MDP) [1], 2) developing a DRL-based control framework and an efficient heuristic variant, and 3) facilitating algorithm training and evaluation with a co-simulation framework.

Figure 4.1 illustrates the overview of our DRL-based framework for HVAC control and evaluation. During building operation, it learns an effective control policy based on sensing data input, without relying on any thermal dynamics model. For offline training and validation of the algorithm, we leverage detailed building dynamics model built in the widely-adopted EnergyPlus simulation tool [2] [63]. Simulation results demonstrate that our framework is able to significantly reduce the energy cost while meeting the room temperature requirements. Next, we will present our modeling of key components for our DRL-based control algorithm.

[1] Our MDP formulation is general and can be time-variant as well.

[2] It should be noted that while the detailed EnergyPlus models are highly accurate and suitable for offline training and validation, their high complexity makes them unsuitable for real-time control.

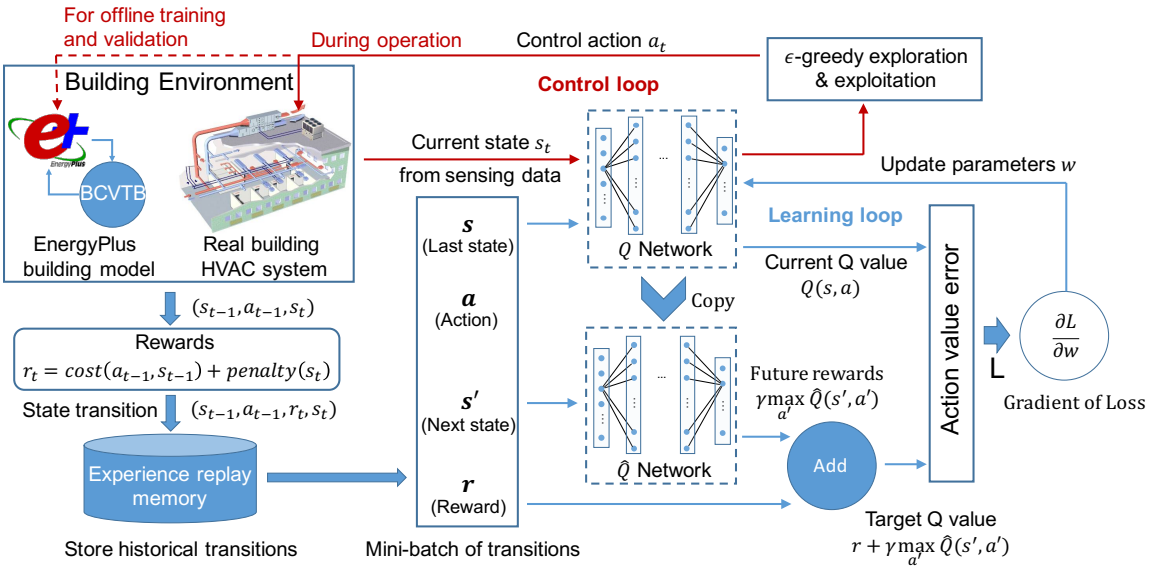

Figure 4.1: Our deep reinforcement learning (DRL) based framework for HVAC control and evaluation. The details of building state transition are defined in section 4.1.1. The details of DRL learning and control process are presented in section 4.1.2.

4.1.1 System Models

The building HVAC system is operated to maintain a desired temperature within each zone, based on current temperature and outside environment disturbances. The zone temperature at next time step is only determined by the current system state and environment disturbances, and the conditioned air input from the HVAC system. It is independent from the previous states of the building. Therefore, the HVAC control operation can be treated as a Markov Decision Process. Next, we formulate the key concepts in this process to facilitate our DRL-based HVAC control algorithm.

(1) Control actions: we consider a building that has z temperature zones and is equipped with a VAV (variable air flow volume) HVAC system. The VAV terminal box at each zone

provides conditioned air (typically at a constant temperature) with an air flow rate that can be chosen from multiple discrete levels, denoted as $F = \{f^1, f^2, ..., f^m\}$. Therefore, the entire action space $A = \{\mathcal{A}^1, \mathcal{A}^2, ..., \mathcal{A}^n\}$ of the building HVAC control includes all possible combinations of air flow rate for every zone, i.e., $n = m^z$. Clearly, the dimension of action space will increase rapidly with larger number of zones and air flow rate levels, which will then greatly increase the training time and degrade the control performance. In section 4.1.2, we introduce a multi-level control heuristic for multiple zones to combat this challenge.

(2) System states: the optimal control action is determined based on the observation of the current system state. In this work, we consider current (physical) time, zone temperature and environment disturbances (i.e. ambient temperature and solar irradiance intensity) to determine the optimal control action. In particular, incorporating current time information in the state enables the DRL algorithm to adapt to time related activities, such as time-varying temperature requirements, electricity price, occupant activities and equipment operation in the building. For environment disturbances, instead of just using current ambient temperature and solar irradiance, we also take into account of multi-step forecast of weather data. This is important because the weather pattern can vary significantly. Considering a short sequence of weather forecast data enables our DRL algorithm to capture the trend of the environment, perform proactive control and adapt to time-variant systems.

(3) Rewards function: the goal of the DRL algorithm is to minimize the total energy cost while maintaining the temperature of each zone within a desired range, by taking a sequence of actions $\{a_1, a_2, \ldots, a_t\}$, where $a_t \in A$. After taking an action a_{t-1} at state

s_{t-1}, the building will evolve into a new state s_t and the DRL algorithm will receive an immediate reward r_t, as calculated below in equation (4.1).

$$r_t = -cost(a_{t-1}, s_{t-1}) - \lambda \sum_{i=1}^{z} ([T_t^i - \overline{T}_t^i]_+ + [\underline{T}_t^i - T_t^i]_+) \tag{4.1}$$

which includes the energy cost of the last action a_{t-1} and the total penalty of temperature violation. We use negative rewards as our DRL algorithm will maximize the total reward. It should be noted that the goal of minimizing energy cost contradicts the goal of maintaining desired temperature, and the reward function tries to balance these two factors.

During the operation of HVAC systems, we want to maximize the accumulative reward $R = \sum_{i=1}^{\infty} \gamma^{i-1} r_{t+i}$, where $\gamma \in [0, 1]$ is a *decay factor* that controls the window length when maximizing the reward. We use $Q^*(s_t, a_t)$, i.e., the *optimal value*, to represent the maximum accumulative reward we can obtain by taking action a_t in state s_t. $Q^*(s_t, a_t)$ can be calculated by Bellman Equation (4.2) in a recursive fashion.

$$Q^*(s_t, a_t) := E[r_{t+1} + \gamma \max_{a_{t+1}} Q^*(s_{t+1}, a_{t+1}) | s_t, a_t] \tag{4.2}$$

The state transition in buildings is stochastic, because the zone temperature is affected by various disturbances, which cannot be accurately measured. In this work, we update the *value estimates* by following the Q-learning [96] method, as shown in equation (4.3).

$$\begin{aligned} Q_{t+1}(s_t,a_t) := {} & Q_t(s_t, a_t) \\ & + \eta(r_{t+1} + \gamma \max_{a_{t+1}} Q_t(s_{t+1}, a_{t+1}) - Q_t(s_t, a_t)) \end{aligned} \tag{4.3}$$

where $\eta \in (0, 1]$ represents the learning rate of value estimates during the training process. Equation (4.3) should converge to the optimal value $Q^*(s_t, a_t)$ over time under the MDP environment.

(4) Building control sequence: our DRL algorithm interacts with the building environment during operation, or with the EnergyPlus model via the *BCVTB* (a Ptolemy II platform that enables co-simulation across different models [97]) interface during offline training and validation.

As shown in Figure 4.2, we use a separate control step $\Delta t_c = k\Delta t_s$ to represent the control frequency of DRL algorithm. Every Δt_c time, as shown in equation (4.4), the DRL algorithm will observe the building state and update the control action. Between two control time steps, the control action used to operate the HVAC system remains the same as the last updated action. While in equation (4.5), the building receives the control signal and enters its next state every Δt_s time, which represents the building simulation or sensor sampling frequency.

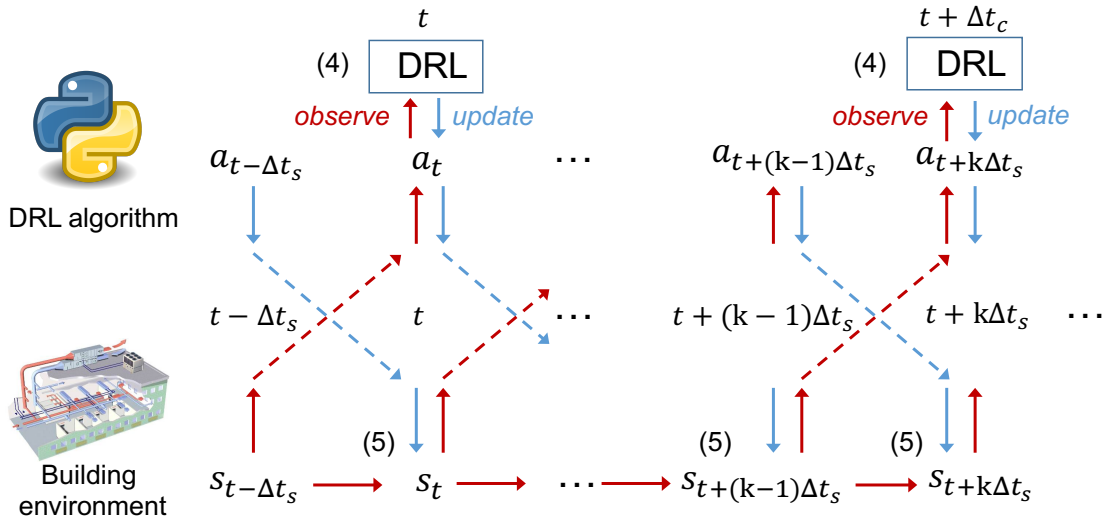

Figure 4.2: Building control sequence with DRL algorithm

$$a_t = f_{DRL}(s_{t-\Delta t_s}) \tag{4.4}$$

$$s_t = f_{ENV}(s_{t-\Delta t_s}, a_{t-\Delta t_s}) \tag{4.5}$$

4.1.2 DRL-based HVAC Control Algorithm

A. Value Function Approximation

The combination of possible values of each feature in the state vector forms a very large state space. In practice, it is more efficient to use generalization methods, such as randomized trees [98], kernel-based method [99] and neural networks [100] to approximate the Q-value. In this work, we use the artificial neural network to approximate the Q-value calculated by equation (4.3).

(1) Neural network architecture: as shown in Figure 4.3, we adopt a similar neural network structure as in [61]. With this structure, the Q-value estimates for all control actions (i.e., $[\mathcal{A}^1, \mathcal{A}^2, ..., \mathcal{A}^n]$) can be calculated by performing one forward pass (inference) in the neural network. This can greatly improve the efficiency when selecting actions with the ϵ-greedy policy. The input features of the network are the environment state that is defined in section 4.1.1. The rectified linear unit (ReLU) is used as the activation function for hidden layers, and the linear layer is used for inferring action value at the output.

We use the mean squared error between the target Q-value and the inferred output of neural network as loss function (4.6), where n denotes the number of possible control actions. Parameters (weights) in the neural network are updated by the mini-batch gradient descent method $w := w - \alpha\Delta w$ [101], where α is the learning rate and $\Delta w = \frac{\partial L}{\partial w}$.

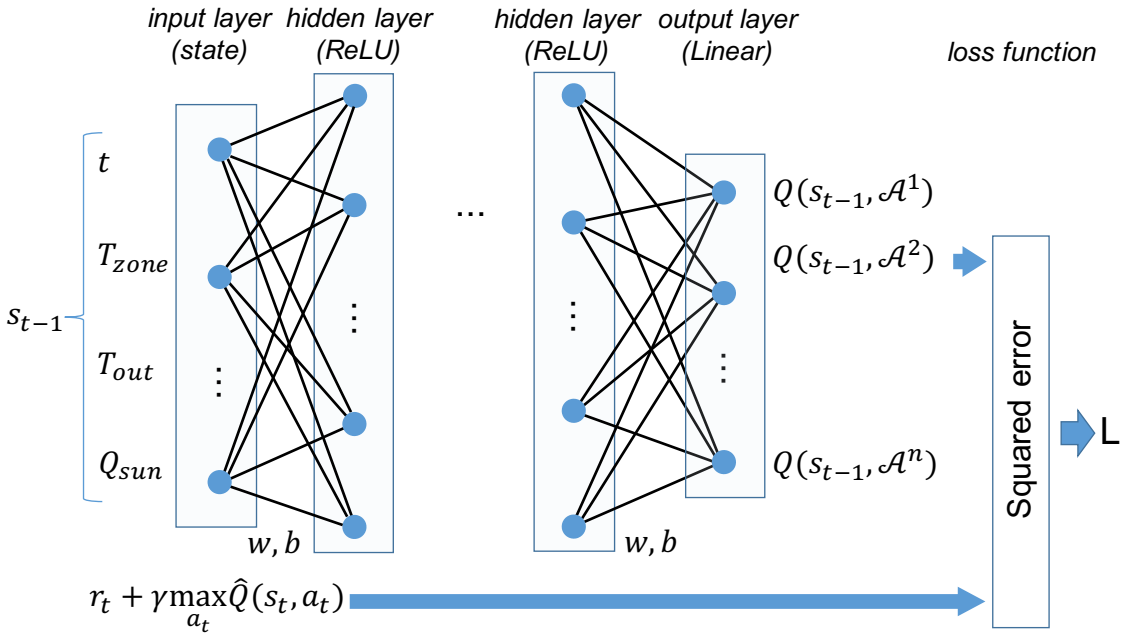

Figure 4.3: Structure of the neural network utilized in our DRL framework

$$L = \frac{1}{2n} \sum_{i=1}^{n} [Q^*(s_t, \mathcal{A}^i) - Q(s_t, \mathcal{A}^i)]^2 \tag{4.6}$$

Being consistent with the Q-learning update process (4.3), the target value $Q^*(s_t, \mathcal{A}^i)$ in the neural network can be estimated by equation (4.7) when using gradient descent, where Q values are approximated by the neural network.

$$Q^*(s_t, a_t) = r_{t+1} + \gamma \max_{a_{t+1}} Q(s_{t+1}, a_{t+1}) \tag{4.7}$$

(2) Training data pre-processing: the input state vector s_t consists of various types of features in the building. The range of value for each feature can vary significantly. To facilitate the learning process, we scale the feature values to a similar range before

feeding the input state to the neural network. In this work, we scale the input state vector to the range $[0, 1]$ as shown in equation (4.8), where x represents a feature in the input state. The minimum and maximum values for each feature can be estimated from historical observations.

$$x' = \frac{x - min(x)}{max(x) - min(x)} \tag{4.8}$$

For output units, the linear layer is used to infer Q-value estimates from hidden units. However, if we directly use reward function (4.1) to calculate the target Q-value as shown in equation (4.7), it may result in a large variance in the target value. During backward propagation, the corresponding bias factor in the last linear layer may dominate the derivative of the loss function, which will prevent weights in earlier layers from learning the optimal value. In order to overcome this limitation, we calculate the target value by first shrinking the original immediate reward with a factor ρ and then clipping it if the target is smaller than -1, as shown in equation (4.9).

$$target\_val(s_{t-1}, a_{t-1}) = \max[\frac{r_t}{\rho} + \gamma \max_{a_t} Q(s_t, a_t), -1] \tag{4.9}$$

In this way, we squash the original target value with a large variance to the range $[-1, 0]$. *The underlying principle is that while it does not help to know which control actions are worse, we focus on which control actions are better.*

(3) Training of the neural network: as shown in Figure 4.1, the one-step state transition process is represented by a tuple $(s_{t-1}, a_{t-1}, r_t, s_t)$, which includes previous state, previous action, immediate reward and current state. The *target vector* of the neural network can be calculated by equation (4.10), where the target value associated with a_{t-1}, i.e.,

$target\_val(s_{t-1}, a_{t-1})$, is calculated by equation (4.9). For other control actions, the target value is set to the current value estimate associated with that action, does not contribute to the loss function.

$$target(s_{t-1}) = \begin{cases} target\_val(s_{t-1}, \mathcal{A}^i) & \text{if } \mathcal{A}^i == a_{t-1} \\ Q(s_{t-1}, \mathcal{A}^i) & \text{otherwise} \end{cases} \quad \forall i \in [1, n] \tag{4.10}$$

Next, the target vector $target(s_{t-1})$ is compared with current inference output of the neural network to calculate the approximation error. Then, we use the RMSprop [102] method to update parameters in the neural network.

B. DRL Algorithm Design

Our DRL-based HVAC control algorithm is presented in Algorithm 8. The outer loop controls the number of training episodes, while the inner loop performs HVAC control at each simulation time step within one training episode.

(1) Initial setup: during learning process, the recent transitions $(s_{t-1}, a_{t-1}, r_t, s_t)$ are stored in memory M, from which a mini-batch of samples will be generated for neural network training. At the beginning, we first initialize memory M as an empty set. Then, we initialize weights w in the neural network similar as in [103]. As shown in equation (4.7), updating neural network weights requires the target value, which also depends on weights in the neural network. To break this dependency loop between target value and weights w, in line 3, a separate neural network $\hat{Q}$ is created for calculating the target value similar as in [61]. This network $\hat{Q}$ will be periodically updated by copying parameters from the network Q. In line 4, the variable a stores the control action in the last step, and s_{pre} and s_{cur} represent the building state in the previous and current control time steps, respectively.

Algorithm 8 DRL-based HVAC Control Algorithm

Initialize memory M = [empty set]

Initialize neural network Q with parameters w

Copy neural network Q and store as $\hat{Q}(\cdot|\hat{w})$

Initialize control action a, state s_{pre} and s_{cur}

for $m := 1$ to N **do**

    Reset building environment to initial state

    for $t_s := 0$ to L **do**

        if $t_s \ mod \ k \ == \ 0$ **then**

            $s_{cur} \leftarrow current \ observation$

            $r = reward(s_{pre}, a, s_{cur})$

            $M \leftarrow (s_{pre}, a, r, s_{cur})$

            Draw mini-batch $(s, a, r, s') \leftarrow M$

            Target vectors $v \leftarrow target(s)$

            Train $Q(\cdot|w)$ with s, v

            Every $d\Delta t_c$ steps, $\hat{Q}(\cdot|\hat{w}) \leftarrow Q(\cdot|w)$

            $\epsilon = \max(\epsilon - \Delta\epsilon, \epsilon_{min})$

            $$a = \begin{cases} \mathcal{A}^i \in A \mid i = random(n) & \text{probability } \epsilon \\ \underset{\tilde{a}}{argmax} Q(s_{cur}, \tilde{a}) & \text{otherwise} \end{cases}$$

            $s_{pre} \leftarrow s_{cur}$

        end if

        Execute action a in building environment

    end for

end for

(2) Learning process: within each training episode, line 8 determines whether the current time step t_s is a control time step. As discussed in section 4.1.1, the control step Δt_c is k times of the simulation step Δt_s. If t_s is a control time step, the algorithm will perform training and determine the new control action (line 9 to 18). Otherwise, the building will maintain the current control action.

During the learning process, in line 9 we first observe the state at current control time step. Then, the immediate reward is calculated by equation (4.1). Next, in line 11 the state transition tuple is stored in memory. Then, a mini-batch of transition tuples are drawn randomly from the memory. Lines 13 to 14 follow equation (4.10) to calculate the target vector and update weights in neural network Q by using the *RMSprop* Back-propagation method [102]. In line 15, the network $\hat{Q}$ will be updated with current weights in network Q in every d control time steps. Then, this $\hat{Q}$ network is used for inferring the target value for the next d control steps.

Next, from line 16 to 18 the network Q is utilized to determine the next control action. The ϵ-greedy policy is used to select the optimal control action based on the output of Q. The algorithm has a probability ϵ to explore the action space by randomly selecting an available action; otherwise, it will choose the action with the maximum value estimate. After each training process, in line 16 the exploration rate ϵ will gradually decrease until reaching at a lower bound ϵ_{min}. In this way, the DRL algorithm is more likely to try different control actions at the beginning. As the training process proceeds, the DRL algorithm will have a higher chance to follow the learned policy. Finally, in line 18 the current state is assigned to s_{pre} to prepare for the next training process.

C. Heuristic Adaption for Multiple Zones

We present a heuristic mechanism that adapts our DRL algorithm for multi-zone HVAC control. As discussed in section 4.1.1, the action space has a cardinality of m^z, which increases exponentially with the number of zones in the building. Training a neural network with such a large number of outputs is inefficient or even infeasible in practice.

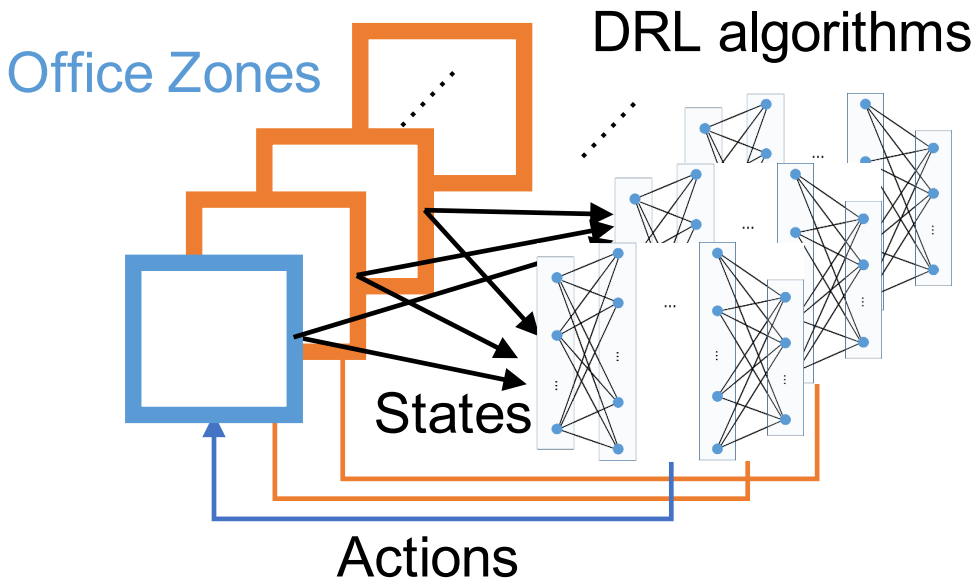

Figure 4.4: Overview of the heuristic adaption for efficient multi-zone HVAC control

In our heuristic as shown in Figure 4.4, instead of using a single neural network to approximate the Q-values of all control actions in the building, we separately train a neural network for each zone using Algorithm 8. Each neural network is responsible for approximating the Q-value in one zone. At each time step, all networks will receive the entire state of the building, and then determine the control action for each zone separately. After executing the control action, the temperature violation penalty for each zone is calculated

similarly as equation (4.1). The electricity cost in each zone is calculated by equation (4.11), which is proportional to the air flow demand in each zone based on the total cost.

$$cost_i = cost \cdot \frac{u_i}{\sum_{i=1}^{n} u_i} \tag{4.11}$$

where *cost* denotes the total electricity cost in the building and u_i represents the air flow rate in each zone. Although the total electricity cost is not exactly a linear function of the air flow rate, we can still heuristically estimate the amount of cost contributed by each zone by following equation (4.11).

4.1.3 Experiments

A. Experiment Setup

We demonstrate the effectiveness of our DRL-based algorithms through simulations in EnergyPlus. We train the DRL algorithms on weather profiles of summer days in two areas, obtained from the National Solar Radiation Data Base [91]. The weather data from Area 1 (Riverside) has intensive solar radiation and large variance in temperature, while Area 2 (Los Angeles) has a milder weather profile. We use the practical time-of-use price from the Southern California Edison [79] to calculate buildings' electricity cost. The desired temperature range is between $19°C$ and $24°C$ based on the ASHRAE standard [104]. There are 4 hidden layers in the neural network. The network layout and other parameters in our DRL algorithms are listed in Table 4.1. We train our DRL algorithm using 100 episodes (months) of data. In practice, the training process can be facilitated by building accurate EnergyPlus models.

Table 4.1: Parameter settings in DRL algorithms

Δt_s	1 min	Δt_c	15 min
k	15	d	$48 * 5$
mini-batch	48	memory size	$48 * 31$
η	0.99	α	0.003
ρ	1000	λ	100
ϵ_{min}	0.1	N	100
$\underline{T}$	$19°C$	$\overline{T}$	$24°C$
number of neurons		50, 100, 200, 400	

We evaluate the performance of our DRL algorithms by comparing them with a rule-based HVAC control strategy (similarly as the one in [105]) and the conventional RL method. In the rule-based approach, the HVAC system is operated by an on-off control strategy such that if the zone temperature exceeds the cooling setpoint (i.e. $24°C$ in our experiment), the room will be cooled at the maximum air flow rate. If the temperature drops below certain threshold [3], the air flow in the zone will be turned off. In our experiment, for both baseline approaches and DRL algorithms, the conditioned air temperature from the HVAC system is set to $10°C$.

B. Experiment Results

(1) Effectiveness of DRL control algorithms in meeting temperature requirements: we evaluate the performance of our DRL algorithms with three buildings modeled in EnergyPlus, which have 1 zone, 4 zones and 5 zones, respectively. The HVAC system can provide multi-level air flow rate for each zone. In this work, we test our DRL algorithms with two-level (i.e. on-off control) and five-level air flow control, where each level is evenly distributed between the minimum and maximum air flow rate of the HVAC system.

[3] We find out that setting it to $20°C$ helps the rule-based approach minimize temperature violation rate.

Figure 4.5 shows the zone temperature in the 1-zone and 4-zone building in August, where our regular DRL algorithm in Algorithm 8 performs on-off control to operate the HVAC system. We can see that after training the DRL algorithm is quite effective in maintaining the zone temperature within the desired range.

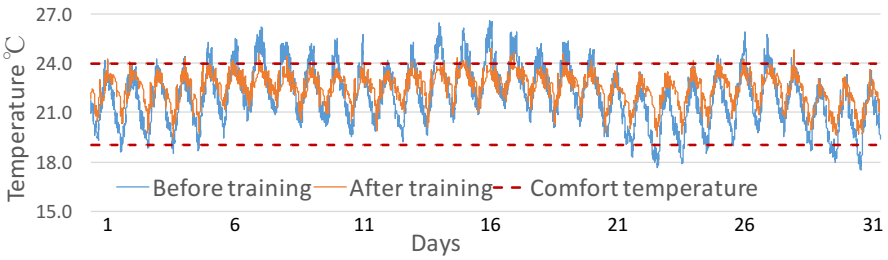

(a) 1 zone

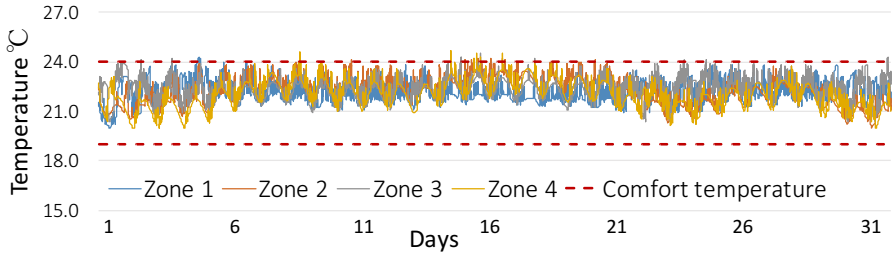

(b) 4 zones

Figure 4.5: Effectiveness of our regular DRL algorithm in maintaining comfort temperature

Figure 4.6 shows the average Q value of our regular DRL algorithm throughout the learning process. At the beginning, the Q value is very small due to the large penalty caused by frequent temperature violations. The Q value will gradually increase as the DRL algorithm learns the effective strategy to maintain the zone temperature within the desired range. Eventually, the Q value will stabilize when the DRL algorithm learns the policy to avoid temperature violation and minimize the electricity cost.

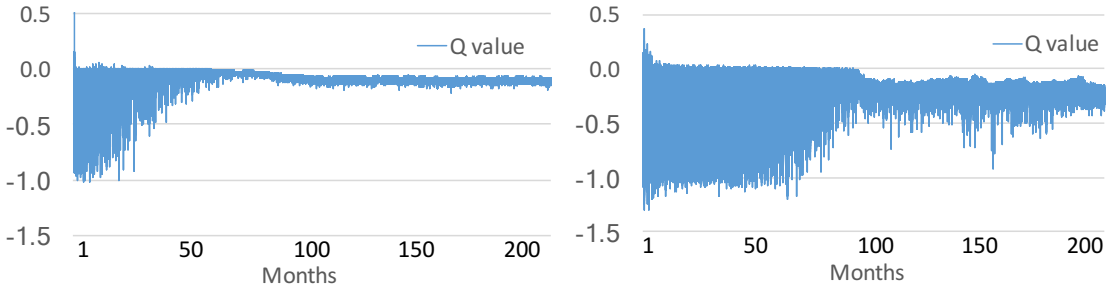

(a) 1 zone

(b) 4 zones

Figure 4.6: Q value in 1-zone and 4-zone buildings

As discussed in section 4.1.2, the action space will exponentially increase with the number of zones. For the 5-zone building, the total number of actions is more than 3000 with 5-level air flow rate control, which would be intractable for our regular DRL algorithm. Therefore, we leverage the efficient heuristic method in section 4.1.2 to perform multi-level control in multi-zone buildings. Figure 4.7 compares the average frequency of temperature violations of the baseline strategy, conventional Q learning, our regular DRL algorithm with on-off control, and the heuristic DRL algorithm with 5-level control. *We can see that the DRL algorithms are able to keep the percentage of temperature violations at a low level.*

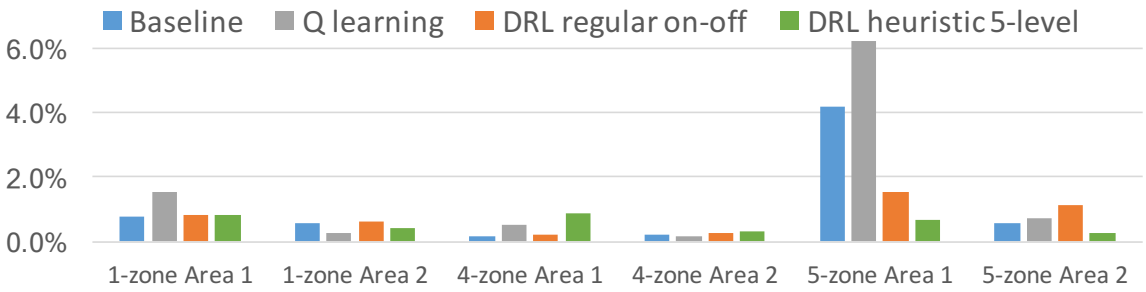

Figure 4.7: Comparison of temperature violation rate between our DRL algorithm, baseline approach and Q learning

(2) Effectiveness of DRL algorithms in energy cost reduction: Figure 4.8 shows the comparison of average daily electricity cost of our DRL control algorithms, conventional Q learning and the baseline approach. The percentage of cost reduction achieved by DRL algorithms compared with the baseline approach is marked in the figure.

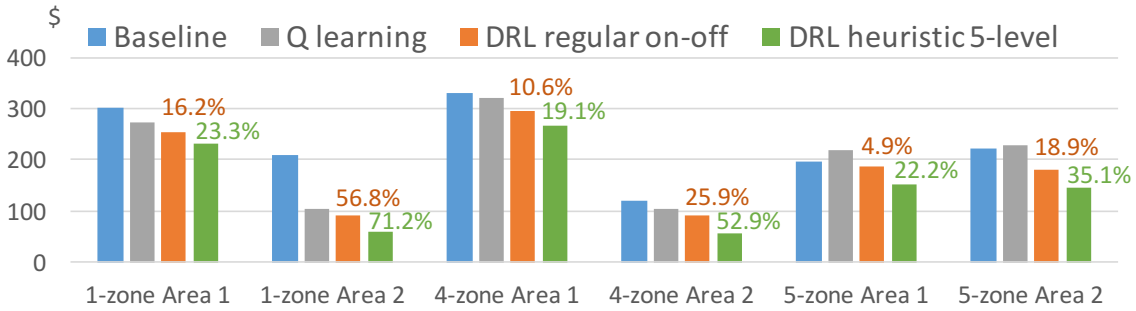

Figure 4.8: Comparison of energy cost between our DRL algorithms, baseline approach and Q learning

We can see that our regular DRL algorithm can achieve significant energy cost reduction compared with the baseline approach and conventional Q learning. The efficient heuristic DRL can leverage multi-level control in multi-zone buildings to achieve further

reduction. Furthermore, the DRL algorithms are more effective in reducing energy cost for Area 2, since the learning process is more effective with a milder weather profile. Compared with the 5-zone building, the DRL algorithms achieve more reduction for 1-zone and 4-zone buildings. That is likely because the 5-zone building is more sensitive to outside disturbances and hence more challenging for the learning process.

Chapter 5

Conclusions and Future Directions

5.1 Conclusions

In this dissertation, we presented our approaches for improving energy efficiency of cyber-physical systems. We developed algorithms and models to optimally schedule various types of flexible energy loads in smart buildings to reduce total energy cost and peak power demand. We further present a proactive demand participation demand response scheme for improving the overall power efficiency in the entire power network. We also develop data-driven algorithms for building energy management based on the state-of-the-art deep reinforcement learning. In conclusion, the major work of this dissertation includes:

- We present a model predictive control (MPC) based algorithm for co-scheduling HVAC control, EV charging and battery usage to reduce total building energy cost, while maintaining the room temperature within the desirable comfort zone and meeting the deadlines for EV charging tasks. Then, we further extend our co-scheduling algorithm for energy management in building clusters. Next, we also address the problem of energy

management for mixed-use buildings (MUBs) with colocated datacenter server rooms. We develop models for key components in MUB and present a co-scheduling formulation to collaboratively schedule the energy demand from operations of both datacenter rooms and office rooms. Our experimental results demonstrate that our co-scheduling approach can significantly reduce energy cost and carbon footprint, while satisfying various building requirements.

- We present an innovative demand response (DR) scheme called proactive demand participation. The proactive DR scheme fully utilizes the flexibility of buildings' energy consumptions and enables individual customers to actively participate in the wholesale electricity market. At the smart building level, an MPC-based HVAC control algorithm is developed for intelligently scheduling HVAC control and battery storage usage. A physical demand bid curve creation algorithm is developed to specify customers' energy consumption preferences under various pricing points. At the wholesale market level, the security constrained economic dispatch problem is formulated to coordinate the operations of power plants and flexible loads. Our experiment results demonstrate that the proactive DR scheme is superior to the conventional passive DR strategies by achieving significant cost reduction for both power generation and building operation and being more robust against various types of malicious cyber attacks, i.e., guideline price manipulation and untruthful demand bidding.
- We develop a deep reinforcement learning (DRL) based data-driven approach for building HVAC control by formulating the HVAC operation as Markov Decision Process (MDP). A co-simulation framework based on EnergyPlus is developed for validation and facilitate

training of our DRL-based approach. Our experiment result based on EnergyPlus models and real weather and pricing data demonstrate that the DRL-based control algorithms are able to significantly reduce energy cost while maintaining the desired room temperature for building tenants.

5.2 Future Directions

There are a few directions to improve our current work in the future:

- Our MPC-based control algorithms for co-scheduling of HVAC, EV charging, datacenter loads and renewable energy sources is mainly evaluated with simulation. In the future work, we can implement and evaluate our algorithms on industrial-size building testbeds.
- In our current proactive demand participation demand response scheme, we assume that there is no power loss in the power distribution process. In the future work, we can take into consideration the power loss in the power distribution line.
- Our current deep reinforcement learning based approach uses discrete level control actions. In the future work, we can extend the current work to enable continuous control to further improve the performance.
- We can further extend our current deep reinforcement learning based approach to enable control for more types of energy loads in the smart building.

Bibliography

[1] Building energy data book of DOE. website:http://buildingsdatabook.eren.doe.gov.

[2] Equinix. www.equinix.com.

[3] NRDC. Scaling up energy efficiency across the data center industry: Evaluating key drivers and barriers. *Issue Paper*, August 2014.

[4] The Green Grid. Pue: A comprehensive examination of the metric. 2012.

[5] S. K. Aggarwal, L. M. Saini, and A. Kumar. Electricity price forecasting in deregulated markets: A review and evaluation. *International Journal of Electrical Power and Energy Systems*, 31(1):13–22, 2009.

[6] N. Rasmussen. Calculating space and power density requirements for data centers. *APC White Paper*. http://www.apcmedia.com/salestools/NRAN-8FL6LW/NRAN-8FL6LW_R0_EN.pdf?sdirect=true.

[7] FERC. A national assessment of demand response potential. 2009.

[8] DOE. Benefits of demand response in electricity markets and recommendations for achieving them. 2006.

[9] N. Li, L. Chen, and S. H. Low. Optimal demand response based on utility maximization in power networks. *IEEE Power and Energy Society General Meeting*, 2011.

[10] F. Oldewurtel, A. Parisio, C. N. Jones, M. Morari, D. Gyalistras, M. Gwerder, V. Stauch, B. Lehmann, and K. Wirth. Energy efficient building climate control using stochastic model predictive control and weather predictions. *American Control Conference (ACC)*, pages 5100–5105, 2010.

[11] M. Maasoumy, A. Pinto, and A. S. Vincentelli. Model-based hierarchical optimal control design for HVAC systems. *ASME Dynamic System Control Conference (DSCC)*, 2011.

[12] Y. Ma, F. Borrelli, B. Hencey, B. Coffey, S. Bengea, and P. Haves. Model predictive control for the operation of building cooling systems. *IEEE Transactions on Control Systems Technology*, 20(3):796–803, 2012.

[13] T. Wei, T. Kim, S. Park, Q. Zhu, S. X. D. Tan, N. Chang, S. Ula, and M. Maasoumy. Battery management and application for energy-efficient buildings. *Design Automation Conference on Design Automation Conference (DAC)*, 2014.

[14] T. Wei, Q. Zhu, and M. Maasoumy. Co-scheduling of HVAC control, EV charging and battery usage for building energy efficiency. *International Conference on Computer-Aided Design (ICCAD)*, 2014.

[15] L. Yang, Z. Nagy, P. Goffin, and A. Schlueter. Reinforcement learning for optimal control of low exergy buildings. *Applied Energy*, 156:577–586, 2015.

[16] P. Xu, P. Haves, M. A. Piette, and J. Braun. Peak demand reduction from pre-cooling with zone temperature reset in an office building. *Lawrence Berkeley National Laboratory*, 2004.

[17] M. Maasoumy and A. S. Vincentelli. Total and peak energy consumption minimization of building hvac systems using model predictive control. *IEEE Design Test of Computers*, 29(4):26–35, Aug 2012.

[18] M. Maasoumy, Q. Zhu, C. Li, F. Meggers, and A. S. Vincentelli. Co-design of control algorithm and embedded platform for building HVAC systems. pages 61–70, April 2013.

[19] Y. Yang, Q. Zhu, M. Maasoumy, and A. S. Vincentelli. Development of building automation and control systems. *IEEE transactions on Design Test of Computers*, 2012.

[20] S. Zhao, X. Lin, and M. Chen. Peak-minimizing online EV charging. technical report, Purdue University, 2013. `http://web.ics.purdue.edu`.

[21] Y. M. Wi, J. U. Lee, and S. K. Joo. Electric vehicle charging method for smart homes/buildings with a photovoltaic system. *IEEE Transactions on Consumer Electronics*, 59(2), 2013.

[22] D. Molina, C. Hubbard, C. Lu, R. Turner, and R. Harley. Optimal EV charge-discharge schedule in smart residential buildings. *Power Engineering Society Conference and Exposition in Africa*, 2012.

[23] C. J. Baldwin, K. M. Dale, and R. F. Dittrich. A study of the economic shutdown of generating units in daily dispatch. *IEEE Transactions on Power Apparatus and Systems*, 78(4):1272–1282, 1959.

[24] J. A. Muckstadt and R. C. Wilson. An application of mixed-integer programming duality to scheduling thermal generating systems. *IEEE Transactions on Power Apparatus and Systems*, 1968.

[25] N. P. Padhy. Unit commitment - a bibliographical survey. *IEEE Transactions on Power Systems*, 19(2):1196–1205, 2004.

[26] T. Shiina and J. R. Birge. Stochastic unit commitment problem. *International Transactions on Operational Research*, 11(1):19–32, 2004.

[27] J. Tu, L. Lu, M. Chen, and R. K. Sitaraman. Dynamic provisioning in next-generation data centers with on-site power production. *International Conference on Future Energy Systems*, 2013.

[28] X. Zhao, T. Peng, X. Qin, Q. Hu, L. Ding, and Z. Fang. Feedback control scheduling in energy-efficient and thermal-aware data centers. *IEEE Transactions on Systems, Man, and Cybernetics: Systems*, 46(1):48–60, Jan 2016.

[29] L. A. Barroso, J. Clidaras, and U. Hoelzle. *The Datacenter as a Computer: An Introduction to the Design of Warehouse-Scale Machines*. Morgan and Claypool, 2013.

[30] M. H. Albadi and E. F. El-Saadany. Demand response in electricity markets: An overview. *IEEE Power Engineering Society General Meeting*, 2007.

[31] N. Zorba J. S. Vardakas and C. V. Verikoukis. A survey on demand response programs in smart grids: Pricing methods and optimization algorithms. *Communications Surveys and Tutorials, IEEE*, 17(1):152–178, 2015.

[32] A. Faruqui and J. R. Malko. The residential demand for electricity by time-of-use: a survey of twelve experiments with peak load pricing. *Energy*, 8(10):781–795, 1983.

[33] J. Aghaei and M. I. Alizadeh. Demand response in smart electricity grids equipped with renewable energy sources: A review. *Renewable and Sustainable Energy Reviews*, 18:64–72, 2013.

[34] R. Hledik A. Faruqui and J. Tsoukalis. The power of dynamic pricing. *The Electricity Journal*, 22(3):42–56, 2009.

[35] K. Herter, P. McAuliffe, and A. Rosenfeld. An exploratory analysis of california residential customer response to critical peak pricing of electriicty. *Energy*, 32(1):25–34, 2007.

[36] G. R. Newsham and B. G. Bowker. The effect of utility time-varying pricing and load control strategies on residential summer peak electricity use: a review. *Energy Policy*, 38(7):3289–3296, 2010.

[37] X. Cao Y. Liang, L. He and Z. J. Shen. Stochastic control for smart grid users with flexible demand. *IEEE Transactions on Smart Grid*, 4(4):2296–2308, 2013.

[38] R. Schober P. Samadi, H. M. Rad and V. W. S. Wong. Advanced demand side management for the future smart grid using mechanism design. *IEEE Transactions on Smart Grid*, 3(3):1170–1180, 2012.

[39] M. A. Biviji J. Wang and W. M. Wang. Lessons learned from smart grid enabled pricing programs. *Power and Energy Conference at Illinois (PECI)*, 2011.

[40] A. J. Conejo, J. M. Morales, and L. Baringo. Real-time demand response model. *IEEE Transactions on Smart Grid*, pages 236–242, 2010.

[41] P. Faria and Z. Vale. Demand response in electrical energy supply: An optimal real time pricing approach. *Energy*, 36(8):5374–5384, 2011.

[42] P. Yi, X. Dong, A. Lwayemi, C. Zhou, and S. Li. Real-time opportunistic scheduling for residential demand response. *IEEE Transactions on Smart Grid*, 4(1):227–234, 2013.

[43] G. Webber, J. Warrington, S. Mariethoz, and M. Morari. Communication limitations in iterative real time pricing for power systems. *IEEE International Conference on Smart Grid Communications*, 2011.

[44] L. Murphy, R. J. Kaye, and F. F. Wu. Distributed spot pricing in radial distribution systems. *IEEE Transactions on Power Systems*, 9(1):311–317, 1994.

[45] J. M. Vignolo and P. M. Sotkiewicz. Distribution network loss allocation with distributed generation using nodal prices. *International Conference on Power Energy Systems*, 2004,.

[46] K. Shaloudegi, N. Madinehi, S. H. Hosseinian, and H. A. Abyaneh. A novel policy for locational marginal price calculation for distribution systems based on loss reduction allocation using game theory. *IEEE Transactions on Power Systems*, 27(2):811–820, 2012.

[47] L. Xu and R. Baldick. Transmission-constrained residual demand derivative in electricity markets. *IEEE Transactions on Power Systems*, 22(4):1563–1573, 2007.

[48] N. G. Singhal and K. W. Hedman. An integrated transmission and distribution systems model with distribution-based lmp pricing. *North American Power Symposium*, 2013.

[49] E. Barrett and S. Linder. *Autonomous HVAC Control, A Reinforcement Learning Approach*. Springer, 2015.

[50] B. Li and L. Xia. A multi-grid reinforcement learning method for energy conservation and comfort of hvac in buildings. *IEEE International Conference on Automation Science and Engineering (CASE)*, pages 444–449, 2015.

[51] D. Nikovski, J. Xu, and M. Nonaka. A method for computing optimal set-point schedules for HVAC systems. 2013.

[52] P. Fazenda, K. Veeramachaneni, P. Lima, and U. M. O'Reilly. Using reinforcement learning to optimize occupant comfort and energy usage in HVAC systems. *Journal of Ambient Intelligence and Smart Environments*, pages 675–690, 2014.

[53] G. T. Costanzo, S. Iacovella, F. Ruelens, T. Leurs, and B. Claessens. Experimental analysis of data-driven control for a building heating system. *CoRR*, abs/1507.03638, 2015.

[54] S. J. Olivieria, G. P. Henzea, C. D. Corbina, and M. J. Brandemuehla. Evaluation of commercial building demand response potential using optimal short-term curtailment of heating, ventilation, and air-conditioning loads. *Journal of Building Performance Simulation*, 7(2):100–118, 2014.

[55] Y. Liu, S. Hu, and T. Y. Ho. Leveraging strategic detection techniques for smart home pricing cyberattacks. *IEEE Transactions on Dependable and Secure Computing*, June 2015.

[56] Z. G. Liu and W. Huang. The design of smart home system based on wi-fi. *Computational Problem-Solving (ICCP)*, pages 454–456, October 2012.

[57] Z. Fan, P. Kulkarni, S. Gormus, C. Efthymiou, G. Kalogridis, M. Sooriyabandara, Z. Zhu, S. Lambotharan, and W. H. Chin. Smart grid communications: overview of research challenges, solutions, and standardization activities. *Communications Surveys and Tutorials*, pages 21–38, January 2013.

[58] S. McLaughlin, P. McDaniel, and W. Aiello. Protecting consumer privacy from electric load monitoring. *Proceedings of the 18th ACM conference on Computer and communications security*, 2011.

[59] J. Liu, Y. Xiao, S. Li, W. Liang, and C. L. P. Chen. Cyber security and privacy issues in smart grids. *IEEE Communications Surveys and Tutorials*, pages 981–997, January 2012.

[60] L. Xie, Y. Mo, and B. Sinopoli. False data injection attacks in electricity markets. *IEEE International Conference on Smart Grid Communications (SmartGridComm)*, pages 226–231, October 2010.

[61] V. Mnih and et al. Human-level control through deep reinforcement learning. *Nature*, 518:529–533, Feb 2015.

[62] D. Silver and et al. Mastering the game of go with deep neural networks and tree search. *Nature*, 529:484–503, 2016.

[63] EnergyPlus. `https://energyplus.net/`.

[64] T. Wei and Q. Zhu. Co-scheduling of flexible energy loads in building clusters. pages 958–961, May 2016.

[65] T. Wei, M. A. Islam, S. Ren, and Q. Zhu. Co-scheduling of datacenter and hvac loads in mixed-use buildings. pages 1–8, Nov 2016.

[66] N. Yu, Q. Zhu, and T. Wei. From passive demand response to proactive demand participation. *International Conference on Automation Science and Engineering (CASE)*, 2015.

[67] T. Wei, Q. Zhu, and N. Yu. Proactive demand participation of smart buildings in smart grid. *IEEE Transactions on Computers*, 65(5):1392–1406, May 2016.

[68] T. Wei, B. Zheng, Q. Zhu, and S. Hu. Security analysis of proactive participation of smart buildings in smart grid. pages 465–472, Nov 2015.

[69] T. Wei, Y. Wang, and Q. Zhu. Deep reinforcement learning for building hvac control. pages 1–6, June 2017.

[70] H. Li, T. Wei, A. Ren, Q. Zhu, and Y. Wang. Deep reinforcement learning: Framework, applications, and embedded implementations: Invited paper. pages 847–854, Nov 2017.

[71] M. Maasoumy and A. S. Vincentelli. Modeling and optimal control algorithm design for HVAC systems in energy efficient buildings, 2011. `http://www.eecs.berkeley.edu/Pubs/TechRpts/2011/EECS-2011-12.html`.

[72] C. Lemaréchal J. F. Bonnans, J. C. Gilbert and C. A. Sagastizábal. Numerical optimization: theoretical and practical aspects. 2006.

[73] M. Chen and G.A. Rincon-Mora. Accurate electrical battery model capable of predicting runtime and i-v performance. *IEEE Transactions on Energy Conversion*, 21(2):504–511, June 2006.

[74] M. Maasoumy, C. Rosenberg, A. S. Vincentelli, and D. S. Callaway. Model predictive control approach to online computation of demand-side flexibility of commercial buildings hvac systems for supply following. pages 1082–1089, June 2014.

[75] W. Tang, S. Bi, and Y. J. Zhang. Online coordinated charging decision algorithm for electric vehicles without future information. *IEEE Transactions on Smart Grid*, 5(6):2810–2824, Nov 2014.

[76] S. Argade, V. Aravinthan, and W. Jewell. Probabilistic modeling of ev charging and its impact on distribution transformer loss of life. *IEEE International Electric Vehicle Conference*, pages 1–8, March 2012.

[77] K. Qian, C. Zhou, M. Allan, and Y. Yuan. Modeling of load demand due to EV battery charging in distribution systems. *IEEE Transactions on Power Systems*, 26(2):802–810, 2011.

[78] K. Qian, C. Zhou, M. Allan, and Y. Yuan. Load model for prediction of electric vehicle charging demand. *International Conference on Power System Technology*, pages 1–6, Oct 2010.

[79] Southern California Edison Company. Schedule tou-gs-3: Time-of-use, general service-demand metered. `https://www.sce.com/NR/sc3/tm2/pdf/CE281.pdf`.

[80] S. Goyal and P. Barooah. Energy-efficient control of an air handling unit for a single-zone VAV system. pages 4796–4801, Dec 2013.

[81] ASHRAE. Ventilation for acceptable indoor air quality. *American Society of Heating, Refrigerating and Air-Conditioning Engineers*, 2004.

[82] H. Phillip. Model predictive control of HVAC systems: Implementation and testing at the university of california, merced. *Lawrence Berkeley National Laboratory*, 2010.

[83] Z. Liu, Y. Chen, C. Bash, A. Wierman, D. Gmach, Z. Wang, M. Marwah, and C. Hyser. Renewable and cooling aware workload management for sustainable data centers. pages 175–186, 2012.

[84] L. Rao, X. Liu, L. Xie, and W. Liu. Minimizing electricity cost: Optimization of distributed internet data centers in a multi-electricity-market environment. pages 1–9, March 2010.

[85] N. Rasmussen. Calculating total cooling requirements for data centers. `http://apcmedia.com/salestools/nran-5te6he/nran-5te6he\_r3\_en.pdf?sdirect=true`.

[86] P. X. Gao, A. R. Curtis, B. Wong, and S. Keshav. It's not easy being green. *Conference on Applications, Technologies, Architectures, and Protocols for Computer Communication*, 42(4):211–222, August 2012.

[87] E. Thereska, A. Donnelly, and D. Narayanan. Sierra: a power-proportional, distributed storage system. *Tech. Rep. MSR-TR-2009-153*, 2009.

[88] Google transparency report. `http://www.google.com/transparencyreport/traffic/explorer`.

[89] L. Wang, P. Mathew, and X. Pang. Uncertainties in energy consumption introduced by building operations and weather for a medium-size office building. *Energy and Buildings*, 53:152–158, 2012.

[90] Tesla. `http://www.teslamotors.com/powerwall`.

[91] NSRDB. `http://rredc.nrel.gov`.

[92] T. Wei and Q. Zhu. Proactive demand participation of heterogeneous flexible loads in smart grid. pages 1–2, Dec 2015.

[93] N. Yu, H. Sheng, and R. Johnson. Economic valuation of wind curtailment rights. *Power and Energy Society General Meeting*, July 2013.

[94] N. Yu, C. C. Liu, and J. Price. Evaluation of market rules using a multi-agent system method. *IEEE Transactions on Power Systems*, 25(1):470–479, 2010.

[95] N. Yu, C. C. Liu, and L. Tesfatsion. Modeling of suppliers learning behaviors in a market environment. *International Journal of Engineering Intelligent Systems*, 15(2):115–121, 2007.

[96] C. J. Watkins and P. Dayan. Q-learning. *Machine learning*, 8(3-4):279–292, 1992.

[97] M. Wetter. Co-simulation of building energy and control systems with the building controls virtual test bed. *Journal of Building Performance Simulation*, 4(3):185–203, 2011.

[98] D. Ernst, P. Geurts, and L. Wehenkel. Tree-based batch mode reinforcement learning. *J. Mach. Learn. Res.*, 6:503–556, December 2005.

[99] D. Ormoneit and Ś. Sen. Kernel-based reinforcement learning. *Machine Learning*, 49(2):161–178, 2002.

[100] M. Riedmiller. *Neural Fitted Q Iteration – First Experiences with a Data Efficient Neural Reinforcement Learning Method*. Springer, 2005.

[101] L. Bottou. Large-scale machine learning with stochastic gradient descent. 2010.

[102] G. Hinton, N. Srivastava, and K. Swersky. Lecture 6a overview of mini–batch gradient descent. `http://www.cs.toronto.edu/~tijmen/csc321/slides/lecture_slides_lec6.pdf`.

[103] K. He, X. Zhang, S. Ren, and J. Sun. Delving deep into rectifiers: Surpassing human-level performance on imagenet classification. pages 1026–1034, 2015.

[104] ASHRAE. Standard 55-2004-thermal environmental conditions for human occupancy. *ASHRAE Inc.*, 2004.

[105] D. Urieli and P. Stone. A learning agent for heat-pump thermostat control. *International Conference on Autonomous Agents and Multi-agent Systems (AAMAS)*, 2013.

[106] S. Zhao, X. Lin, and M. Chen. Peak-minimizing online EV charging: Price-of-uncertainty and algorithm robustification. *IEEE Conference on Computer Communications (INFOCOM)*, pages 2335–2343, April 2015.

[107] Z. Liu, Y. Chen, C. Bash, and A. Wierman. Renewable and cooling aware workload management for sustainable data centers. *SIGMETRICS Performance Evaluation Review*, 40(1), 2012.

[108] Y. Li, Y. Wen, K. Guan, and D. Tao. Transforming cooling optimization for green data center via deep reinforcement learning. *CoRR*, abs/1709.05077, 2017.

[109] E. Alpaydin. Introduction to machine learning (adaptive computation and machine learning). *MIT Press*, 2004.